Summer 8-15-2018

Instrumentation for Cryogenic Dynamic Nuclear Polarization and Electron Decoupling in Rotating Solids

Faith Joellen Scott
Washington University in St. Louis

WASHINGTON UNIVERSITY IN ST. LOUIS

Division of Chemistry

Dissertation Examination Committee:
Alexander Barnes, Chair
Joseph Ackerman
Sophia Hayes
Richard Loomis
Jacob Schaefer

Instrumentation for Cryogenic Dynamic Nuclear Polarization and Electron Decoupling in Rotating Solids

by

Faith Scott

A dissertation presented to
The Graduate School
of Washington University in
partial fulfillment of the
requirements for the degree
of Doctor of Philosophy

August 2018
St. Louis, Missouri

Table of Contents

List of Figures

List of Tables

Acknowledgments

Many thanks to my advisor and mentor Professor Alexander Barnes whose enthusiasm for science gave me energy for the project, and whose brainstorms and input have been instrumental to my PhD. I would also like to thank members of the Barnes Lab past and present- you gave me a joyful working and learning environment that I will remember the rest of my life. Thank you to my thesis committee and Dr. Mark Conradi who have helped to guide my academic journey at every step. Special thanks to Dr. Hao Yang for many fruitful conversations and for organizing the NMR discussion group where I learned so much about the field in my early years. I also thank Gregory Potter and Zayd Ma for helpful discussions regarding my research. I would also like to thank Jim Linders, James Graflage and Larry Guerdan from the Chemistry Machine shop, whose expertise has saved my projects countless times.

Funding was provided through an NSF STTR National Science Foundation Small Business Technology Transfer grant (STTR 1521314), NSF CAREER award NSF-IDBR (CAREER DBI-1553577), and the NIH Director's New Innovator Award from the National Institutes of Health (DP2GM119131). The resonator project described in Chapter 4 of this dissertation was pursued in collaboration with Alexander Laut and Dr. Jagadishwar Sirigiri and was funded under STTR 1521314. DNP enhancement profiles and the EPR profile of $N@C_{60}$ endofullerene in Chapter 2 were completed in collaboration with Dr. Anil Jagtap and Dr. Snorri Sigurddson at the University of Iceland, Dr. Johannes Wittmann and Dr. Björn Corzilius at Goethe University Frankfurt (BMRZ), and Dr. Michael Eckardt and Dr. Wolfgang Harneit at Johannes Gutenberg-Universität Mainz, and Universität Osnabrück.

I would like to thank my family and friends for their support through this journey, especially my husband Dustin, who has made my work possible on a day-to-day basis, and my parents who

have supported me throughout my life. I would also like to thank my grandfather Phil Passon, who tutored me in AP chemistry with a zeal for learning and was a role model for my academic career.

Faith Scott

Washington University in St. Louis

August 2018

ABSTRACT OF THE DISSERTATION

Instrumentation for Cryogenic Dynamic Nuclear Polarization and

Electron Decoupling in Rotating Solids

by

Faith Joellen Scott

Doctor of Philosophy in Chemistry

Washington University in St. Louis, 2018

Professor Alexander Barnes, Chair

Dynamic nuclear polarization (DNP) increases the sensitivity of nuclear magnetic resonance (NMR) using the higher polarization of electron radical spins compared to nuclear spins. The addition of electron radicals for DNP to the sample can cause hyperfine broadening, which decreases the resolution of the NMR resonances due to hyperfine interactions between electron and nuclear spins. Electron decoupling has been shown to attenuate the effects of hyperfine coupling in rotating solids. Magic angle spinning (MAS) DNP with electron decoupling requires a high electron Rabi frequency provided by a high-power microwave source such as a frequency-agile gyrotron. This dissertation describes the development of instrumentation to improve electron decoupling through a higher electron Rabi frequency, including two designs for frequency agile gyrotrons and a MAS rotor resonator to increase the effect of microwaves at the sample. Electron spin relaxation times are increased at cryogenic temperatures, enabling manipulation of electron spins with lower electron Rabi frequency. Therefore, a cryostat with interchangeable MAS-DNP NMR probes for DNP experiments ranging from 4-80 K has been constructed and tested.

Chapter 1: Introduction

1.1 Nuclear magnetic resonance

Nuclear magnetic resonance (NMR) is a nondestructive spectroscopic method used to study chemical structure and molecular dynamics [1,2]. It is widely used in biology as well as materials science [3–6]. NMR can determine average structures down to 0.1 Å and investigate dynamics on a timescale as short as 1 μs [2,7,8]. NMR operates by manipulating the spin Hamiltonian of the NMR active (spin ½ or higher) isotope nucleus within the sample and collecting the electrical signal emitted by the precession of nuclear spins in the presence of a magnetic field. The spin Hamiltonian includes several interactions, some of which are anisotropic and are averaged to their isotropic values by the tumbling of molecules in solution state NMR. In solid state NMR, these isotropic and anisotropic interactions contribute to faster relaxation and, consequently, broader resonances. In NMR experiments, signals from repeated scans can be added together so that the signal to noise ratio (SNR) builds up as the square root of the number of scans. A major goal of NMR spectroscopists is to derive meaningful data from the NMR sample while keeping experimental time short. Spin polarization is a factor in dictating the sensitivity of an NMR measurement:

$$P = \tanh\left(\frac{\gamma \hbar B_0}{2k_B T}\right)$$

This indicates that polarization, P, and therefore NMR sensitivity, can be improved by increasing the strength of the main magnetic field (B_0), decreasing the temperature (T), or using the polarization of a nucleus with a higher gyromagnetic ratio (γ). Plank's constant divided by 2π (ħ) and Boltzmann's constant (k_B) cannot be changed, but the three variables are often exploited to gain NMR sensitivity. Lowering sample temperature and creating higher magnetic fields both

add operational costs, but are often utilized to reduce experimental time [9–11]. In solid state NMR, the higher polarization of high γ ^{1}H nuclei can be transferred to ^{13}C, ^{15}N, or other low γ nuclei by cross polarization [12–14].

1.1.1 Magic angle spinning

In solution state NMR, molecules tumble at a fast enough rate to average out anisotropic interactions from the Hamiltonian. However, in solid samples, anisotropic interactions are not averaged out and contribute to shorter relaxation times. However, many anisotropic terms contain the angle-dependent component $(1\text{-}3\cos^2\theta)$. This term is zero when θ, the angle of the two spins to the main magnetic field (B_0), is approximately 54.7°. Molecules do not need to be tumbled isotropically to average out these terms- if the sample is rotated at a high enough frequency about this axis at a 54.7° angle to the main magnetic field, anisotropic interactions containing this term can be mostly averaged out. Spinning the sample at 54.7° to the main magnetic field is known as magic angle spinning (MAS) because of its profound effects on many anisotropic interactions such as chemical shift and dipolar interactions [14]. In some cases such as hyperfine interactions, the interactions are too strong (1-10 MHz) to be averaged out by spinning with current technology, but research is always underway to push to higher spinning frequencies for better resolution [15,16].

1.2 Dynamic nuclear polarization

In NMR and especially solid-state NMR, a very large amount of radiofrequency (RF) power (up to 1 kW) is used to disturb the equilibrium of the sample, and only a very small signal is received back. Complex experiments such as multidimensional NMR or REDOR on biologically relevant sample concentrations can take a long time because of low signal- even with isotopic enrichment of the nuclei of interest. Dynamic nuclear polarization (DNP) uses microwaves at specific

matching conditions to transfer the higher polarization of radical electrons to nuclei with lower γ values to enhance the sensitivity of NMR. This enhancement is usually measured as the signal with microwave matching condition “DNP on” divided by the signal without microwaves “DNP off”. Several DNP mechanisms occur but at a magnetic field of 7 T, solid effect and cross effect are observed most often. Narrow line radicals such as trityl are used for solid effect, and broad line radicals such as bcTol-M are used for cross effect [17–19]. Electron radicals for DNP are classified as narrow line or broad line based primarily on whether the full width at half maximum of the EPR spectrum for the radical has a greater frequency than the Larmor frequency of the nuclear spin that is being enhanced.

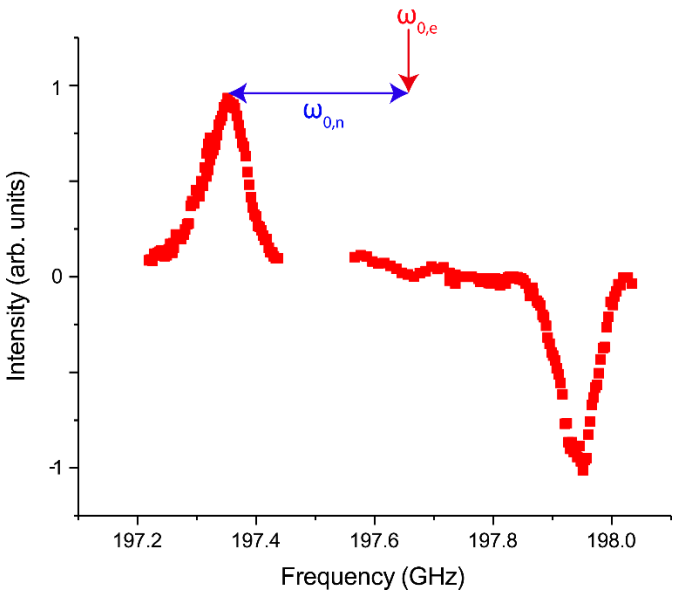

Figure 1.1 Solid effect ^{1}H enhancement profile 4 M [^{13}C, ^{15}N] urea in 60% d8-glycerol, 30% D_2O and 10% H_2O with 40 mM trityl radical. The frequency difference of the nuclear Larmor frequency ($\omega_{0,n}$, blue) from the highest positive enhancement indicates the electron Larmor frequency ($\omega_{0,e}$, red arrow). The nuclear Larmor frequency plus the electron Larmor frequency is the microwave frequency where highest negative enhancement is observed. Data from [20] with permission.

1.2.1 Solid effect

Solid effect DNP occurs between an electron radical spin and nuclear spin. Microwaves are applied to the sample at a frequency equal to the electron Larmor frequency ($\omega_{0,e}$) plus or minus the nuclear Larmor frequency ($\omega_{0,n}$) (**Figure 1.1**) [21,22]. Maximum positive enhancement

occurs at the matching condition $\omega_{0,e} - \omega_{0,n}$ and maximum negative enhancement occurs at the alternate matching condition, $\omega_{0,e} + \omega_{0,n}$. Solid effect enhancements are inversely related to B_0^2 [21] because of the increase in bandwidth of the electron radical lineshape as magnetic field increases.

1.2.2 Cross effect

Cross effect is considered to be more effective at high magnetic fields because maximum enhancement scales as the inverse of B_0 instead of the inverse of B_0^2 [23]. However, both cross effect and solid effect mechanisms can be accessed at 7 T. Two electron spins separated in frequency by the Larmor frequency of the polarized nucleus are required for cross effect (**Figure 1.2**), and thus broad line radicals usually display cross effect DNP mechanism. Biradicals are advantageous for cross effect because the electron spins need to be physically close enough to each other and the nucleus to complete DNP transfer. Without a biradical, a broad line monoradical must be at a much higher concentration to reach the same enhancement levels as a similar biradical, and the higher concentration causes higher levels of hyperfine broadening in the sample [24]. In magic angle spinning systems, broad line biradicals used for the cross effect can de-polarize the sample even without microwaves, which can cause overall enhancement, a comparison of signal with DNP polarization to a signal without microwaves, to be artificially inflated [25]. This effect can be taken into consideration by measuring a sample with no DNP radical and comparing this value to the "DNP on" value for the sample containing DNP radical. The integrated NMR spectrum of a stationary sample with radical can also be compared to the integrated "DNP on" spectrum, but this does not take radical bleaching into consideration [25].

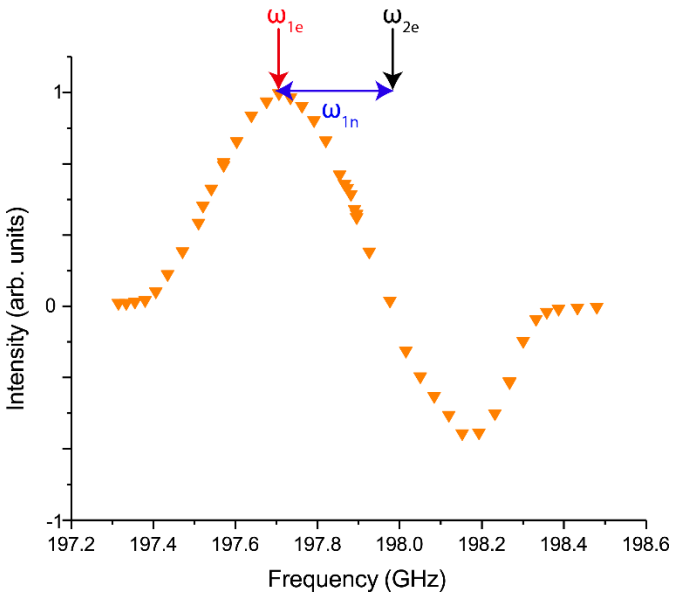

Figure 1.2 Cross effect ^{1}H enhancement profile of 4 M [^{13}C, ^{15}N] urea in 60% d_8-glycerol, 30% D_2O and 10% H_2O with 20 mM bcTol-M. The frequency difference between the two electron spins ($\omega_{0,1e}$ and $\omega_{0,2e}$, red and black respectively) is equal to the nuclear Larmor frequency ($\omega_{0,n}$, blue). Microwave frequency is applied at $\omega_{0,1e}$ for each DNP enhancement value shown. Data from [20] with permission.

1.3 Hyperfine interaction

Hyperfine interactions decrease the resolution of the NMR spectrum in the presence of EPR radicals. Hyperfine interactions are a type of spin-spin interaction between radical electrons and nuclei. Like internuclear dipolar interaction, the relationship between the two spins is dependent on their angle relative to the main magnetic field, and more importantly, the distance between the spins. The dipolar hyperfine interaction strength is dependent on $\frac{1}{r^3}$ where r is the distance between the electron spin and the nuclear spin so that the electron is very strongly coupled to nuclei nearby, but outside of 20 Å the coupling is negligible. This means a sample with a higher concentration of electron radicals will show stronger average hyperfine interactions. Hyperfine interactions within DNP samples are usually strong enough that they cause shifts in some nuclear frequencies and so the spectrum is broadened, decreasing NMR resolution. This hyperfine broadening is too strong to average out with current magic angle spinning frequencies [26,27].

1.4 Electron decoupling

Electron radical concentrations that provide optimal DNP enhancement decrease the resolution of the NMR spectrum. The Barnes lab has implemented electron decoupling in a magic angle spinning system to decrease the negative effects of hyperfine broadening [28]. Electron decoupling parallels the strategy of proton decoupling (**Figure 1.3**). Once polarization has been transferred from electrons to carbon nuclei using the solid effect matching condition frequency, the microwave frequency is changed to the trityl radical resonant frequency and swept back and forth. The frequency sweeps across the trityl EPR lineshape are necessary because the microwave power used in this experiment does not generate a high enough electron Rabi frequency to nutate all the electron spins with continuous wave radiation.

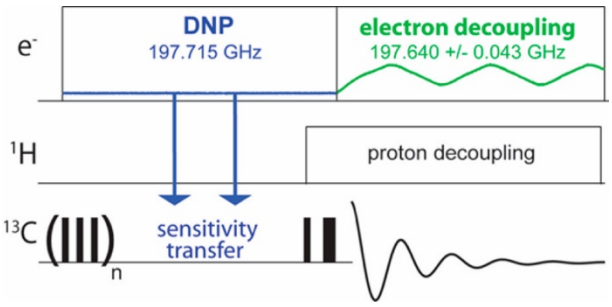

Figure 1.3 Pulse sequence for electron decoupling. Voltage profile (not to scale) for the anode shown in blue and green on the electron channel. Solid effect DNP transfer (blue) at 197.715 GHz polarizes the ^{13}C nuclei, then the microwave frequency is changed to sweeps centered around 197.640 GHz (the electron Larmor frequency of the radical) for electron decoupling. For experiments without electron decoupling, the sweeps were sent in the opposite direction, off resonance. Proton decoupling was applied during electron decoupling and acquisition. Figure from [28] with permission.

Electron decoupling is observed as NMR linewidth narrowing as hyperfine interactions are averaged. The linewidth of 4 M urea with 40 mM trityl (Finland radical) in a 60% d_8-glycerol, 30% D_2O, 10% H_2O mixture was reduced at full width half maximum (FWHM) to 48 Hz by electron decoupling at 0.5 s (**Figure 1.4**).

A frequency-agile microwave source is required to shift from the DNP matching condition to the electron decoupling frequency before the polarization benefit lent by DNP decays by nuclear longitudinal relaxation. This required the design and construction of a frequency agile gyrotron capable of generating an electron Rabi frequency of 0.46 MHz without the use of a resonator [29].

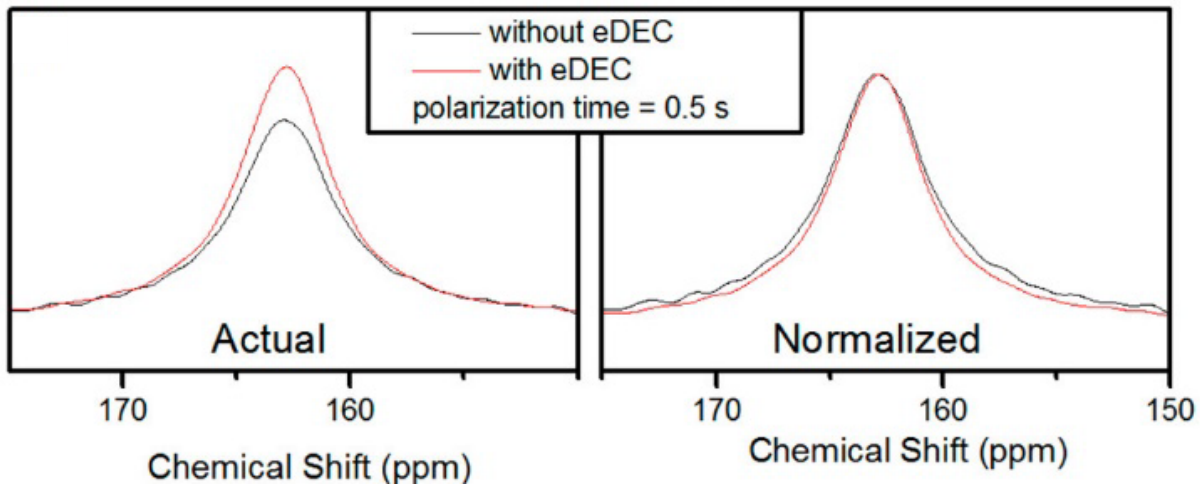

Figure 1.4 Spectra of 4 M [^{13}C, ^{15}N] urea comparing electron decoupling (red) to no electron decoupling (black) at a polarization time of 0.5 s with 40 mM trityl in 60% d_8-glycerol: 30% D_2O:10% H_2O mixture. Magnetic field=7 T, ^{13}C Zeeman frequency=75.495 MHz. Linewidth narrowing was 48 Hz. Figure adapted from [28] with permission.

1.5 Instrumentation for MAS-DNP NMR

MAS-DNP NMR can collect data on biologically relevant samples up to 430,000 times faster than traditional MAS NMR, but gyrotrons, waveguides and cryogenic systems are required in addition to the spectrometer used for MAS NMR. The gyrotron provides microwave power, which propagates through the waveguide and into the sample which is cooled below 100 K (**Figure 1.5**).

1.5.1 MAS NMR Probe

The NMR probe sends radiofrequency (RF) pulses into the sample and receives back an RF signal up to 10,000 times weaker from the relaxation of spins within the sample. Circuits are

carefully isolated and diodes are strategically placed so that the signal from the amplifiers (up to 1 kW) does not damage the sensitive receiver. Several different kinds of probes are custom built or available for purchase for MAS-NMR experiments [13,30].

The experiments within this dissertation employ transmission line style probes. These probes are built in the Schaefer McKay style [31] and can irradiate up to four NMR channels simultaneously. At 7.05 T, ^{1}H resonates at 300.184 MHz, ^{31}P at 121.516 MHz, ^{13}C at 75.495 MHz, and ^{15}N at 30.427 MHz. Since each of these frequencies has a different wavelength in the copper conductor used, the channel branch for ^{13}C, ^{15}N, and ^{31}P can be connected at a ¾ wavelength current node for ^{1}H. ^{13}C and ^{31}P can be connected at a ¼ wavelength ^{15}N current node, and so on, so that the current from the first channel does not go down the two lower frequency channels, etc. In the other direction, lower frequencies are prevented from attenuation via in-line capacitors.

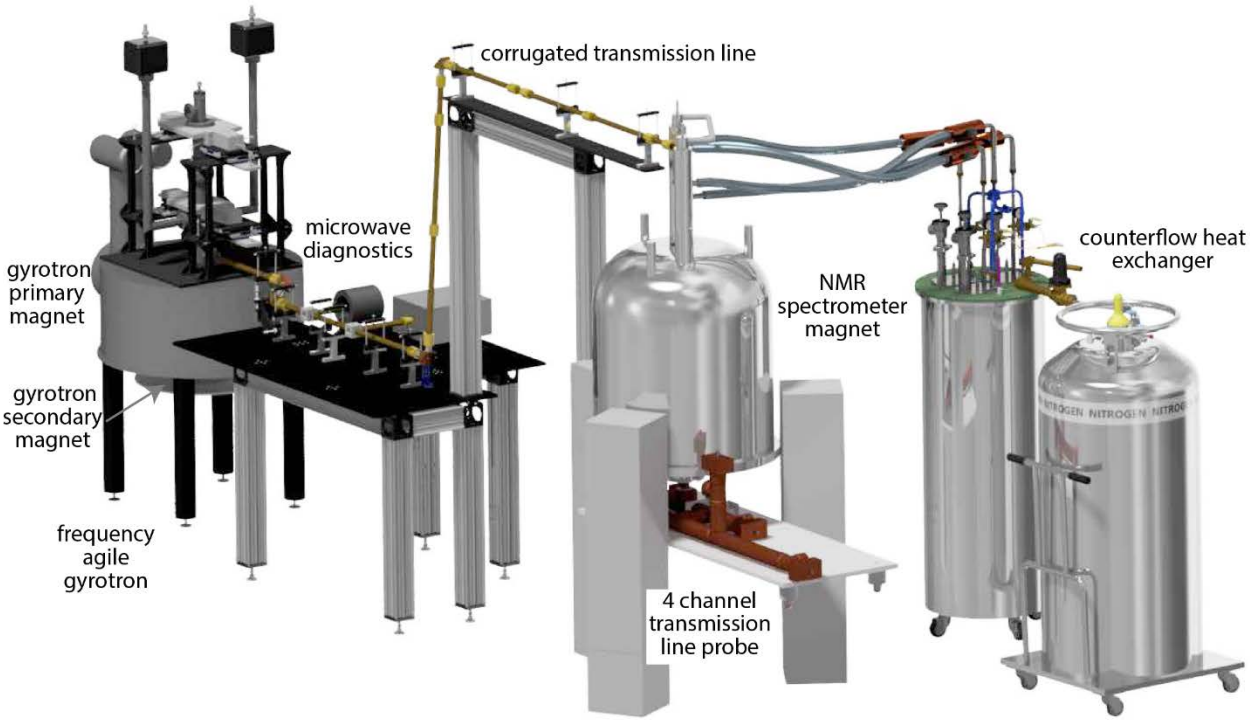

Figure 1.5 Schematic of the DNP spectrometer showing the NMR magnet, probe, microwave transmission line, gyrotron, and heat exchanger. Figure from [20] with permission.

Magic angle spinning probeheads contain a stator which holds the rotor and spins the sample at an angle of 54.7° to the main magnetic field. The gas lines shown in **Figure 1.6** supply drive or spinning gas to the turbine fins on the rotor and bearing gas to float the rotor on a cushion of air and reduce friction. For DNP, pure nitrogen or helium gas is used for cryogenic spinning. A 3.2 mm outer diameter rotor can spin up to 20 kHz. A variable temperature (VT) fluid line cools the center of the rotor. The separate VT line allows for flexibility in cooling the sample. While the drive and bearing gases are cooled, the flow of either line does not need to be increased to provide additional cooling power, which can introduce spinning instability.

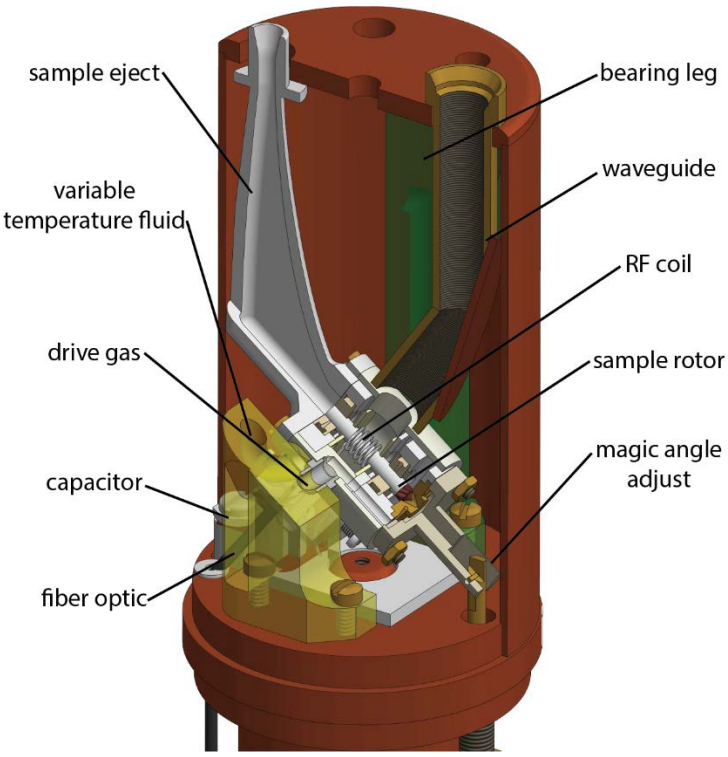

Figure 1.6 A probehead built to support MAS of 3.2 mm OD rotors.

1.5.2 Cryogenic equipment

DNP transfer mechanisms are more efficient at temperatures below 80 K due in part to the increased electron spin relaxation time. The probes described in this thesis can reach

temperatures as low as 4.6 K by using 80 K helium gas for drive and bearing gas and spraying liquid helium mist at 4.2 K on the center of the rotor. 80 K experiments are more often carried out with nitrogen gas as drive, bearing, and VT gas. These extremely low temperatures are possible because of insulation of transfer line and probehead, as well as the efficient liquid nitrogen heat exchanger used.

Nitrogen gas for spinning and thermostating is pre-cooled by a circuit in the machine room adjacent to the lab. Atmospheric air is pumped through a series of passive and mechanical driers and an oxygen absorbing “nitrogen generator” to leave pure nitrogen gas. From there it is split into drive, bearing, and VT gas lines which are controlled through an MAS controller (Tecmag, Houston, TX). The three gas streams are passed through Polycold gas chillers as a pre-cooling step before being routed into the NMR laboratory room (Brooks, MA). The air channels now at a temperature of ~210 K are sent through the heat exchanger before entering the NMR probe.

The heat exchanger [32] cools the gas in the drive, bearing, and VT channels further with returning exhaust gas then with compressed liquid nitrogen. This heat exchanger can cool gas to 80 K and uses about 90 L of liquid nitrogen a day, a marked improvement over a previous design which used 300 L of liquid nitrogen per day [33]. Exhaust gas from the probe is brought back to the heat exchanger and is split into three channels for each of the three canisters. The exhaust cools the incoming gas by passing through a counterflow coil which surrounds the incoming gas stream.

The transfer lines used to transfer cryogens into the probe are broken into two parts. The flexible section connects the heat exchanger to the top of the NMR magnet, and the rigid portion carries the gas into the bore of the magnet and to its function in the probehead. Transfer lines are required for drive and bearing gas, explained above as part of magic angle spinning apparatus.

Additionally, vacuum jacketed transfer lines for the returning exhaust gas and sample exchange are inserted into the top of the probe, as well as the last section of the waveguide.

The exhaust gas exits the probe through two vacuum jacketed lines. One has a large inner diameter to reduce back-pressure in the probehead, which can cause spinning instability. The other line is connected back to the heat exchanger to the outside of the counterflow coil. The exhaust gas coming out of the probe is still at a temperature of 110 K so it is a valuable resource for cooling. The cold exhaust air is injected into the bottom of the counterflow coil jacket and spirals upwards as the incoming gas spirals downwards. According to fluid dynamic simulations, the incoming gas drops from 210 K to 152 K as a result of this heat transfer. Thus, less heat must be transferred to the liquid nitrogen in the second chamber and liquid nitrogen is conserved.

The sample eject uses a jet of air to exchange samples while the probehead remains in place at cryogenic temperatures. The sample is caught at the end of a flexible tube in a nearby box and new samples are inserted at the top of the vacuum jacketed sample eject tube.

While not a vacuum-jacketed cryogenic transfer line, the waveguide enters from the top of the magnet to deliver microwaves from the gyrotron to the NMR sample. The waveguide is fitted with a Teflon insert so that cryogenic gases do not escape through the waveguide and cool this non-vacuum-jacketed transfer tube.

The cryostat insulates the probehead, protects the NMR magnet, and keeps the transfer lines in place. The gasket seals of the magnet become brittle and break vacuum at low temperatures, causing the magnet to quench. To prevent magnet quenching, the vacuum layer of the cryostat insulates the probehead cryogenic temperature from room temperature processes. All transfer

lines and the waveguide are inserted into the probehead from the top of the magnet through the cryostat, and a brass plate with O-ring seals around the transfer lines.

1.5.3 Gyrotron and waveguide

The microwave power necessary for excitation of electron radicals in MAS-DNP can be provided by free electron lasers, slow wave traveling wave tubes, or gyro devices like gyroampifiers and gyrotrons [34–40]. The gyrotron built in the Barnes lab is unique because it is frequency agile over a bandwidth of at least 670 MHz at a single magnetic field, though several gyrotrons have demonstrated frequency agility [35,41,42]. The gyrotron operates with an electron beam accelerated through a magnetic field in a vacuum (**Figure 1.7**). As the electron beam moves through the magnetic field, the electrons move in circles in a plane orthogonal to the main magnetic field. The beam is compressed until it comes to the interaction cavity, where some of the electron beam power is deposited into a TE_{52} microwave mode which also travels up the gyrotron. Microwaves are converted by the internal mode converter and reflected out of the sapphire window to be used in DNP experiments. The remaining electron beam power is deposited at the water-cooled beam collector as heat. Ceramic breaks allow for different electric potentials to be applied to different parts of the gyrotron.

The waveguide allows the microwave power to be transmitted from the gyrotron to the NMR probe with a loss of 4.4 dB (**Figure 1.5**). Microwaves travel in the HE_{11} mode with the least attenuation within corrugated waveguide out of all modes [43]. The microwave mirrors are flat pieces of polished copper to reflect the microwaves up and over to the top of the NMR magnet and down into the bore. A final mirror at an angle of 73° reflects the microwaves onto the NMR sample rotor.

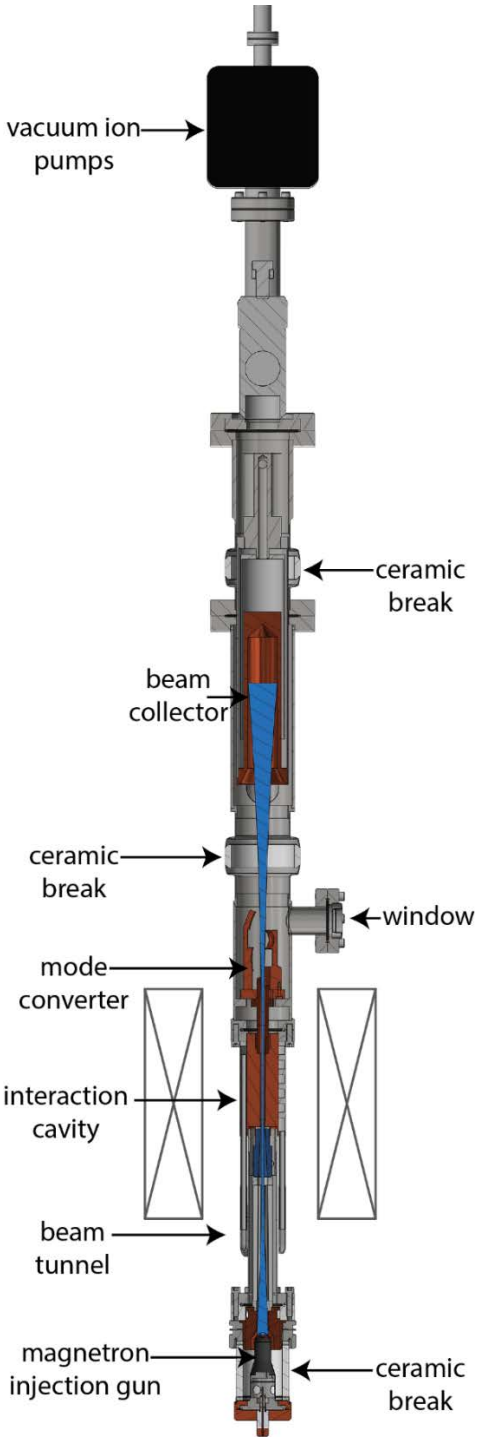

Figure 1.7 Schematic cross-section of a gyrotron. The location of the magnet is indicated by grey crossed boxes around the interaction cavity. Adapted from [20] with permission.

1.6 Specific aim: achieving higher electron Rabi frequency

The enhancement value for DNP and the adiabaticity factor used in electron decoupling sweeps are both dependent on the electron Rabi frequency at the DNP sample. Electron Rabi frequency

can be improved by increasing the incoming microwave power or better utilizing microwaves at the source by creating a resonant structure inside the sample or focusing the microwaves with a lens. I will discuss the first two methods at length, though development of the third method, lens focusing, has been used to good success in the Barnes lab.

With a lower sample temperature, the same electron Rabi frequency can be used to greater effect. This is because the electron relaxation time is longer at lower temperatures, and so there is less loss of polarization due to relaxation before the experiment can be completed. For this reason, cryogenic equipment is used.

References

[1] A. McDermott, Structure and Dynamics of Membrane Proteins by Magic Angle Spinning Solid-State NMR, Annu. Rev. Biophys. 38 (2009) 385–403. doi:10.1146/annurev.biophys.050708.133719.

[2] H. Yang, D. Staveness, S.M. Ryckbosch, A.D. Axtman, B.A. Loy, A.B. Barnes, V.S. Pande, J. Schaefer, P.A. Wender, L. Cegelski, REDOR NMR reveals multiple conformers for a protein kinase c ligand in a membrane environment, ACS Cent. Sci. 4 (2018) 89–96. doi:10.1021/acscentsci.7b00475.

[3] G. Tong, Y. Pan, H. Dong, R. Pryor, G.E. Wilson, J. Schaefer, Structure and dynamics of pentaglycyl bridges in the cell walls of Staphylococcus aureus by 13C-15N REDOR NMR, Biochemistry. 36 (1997) 9859–9866. doi:10.1021/bi970495d.

[4] M. Afeworki, R.A. McKay, J. Schaefer, Dynamic nuclear polarization enhanced nuclear magnetic resonance of polymer-blend interfaces, Mater. Sci. Eng. A. 162 (1993) 221–228. doi:10.1016/0921-5093(90)90046-6.

[5] F.A. Bovey, E.W. Anderson, D.C. Douglass, J.A. Manson, Polymer NMR spectroscopy. X. The use of H1-H1spin decoupling in the elucidation of polymer structure, J. Chem. Phys. 39 (1963) 1199–1202. doi:10.1063/1.1734413.

[6] A.J. Rossini, C.M. Widdifield, A. Zagdoun, M. Lelli, M. Schwarzwälder, C. Copéret, A. Lesage, L. Emsley, Dynamic nuclear polarization enhanced NMR spectroscopy for pharmaceutical formulations, J. Am. Chem. Soc. 136 (2014) 2324–2334. doi:10.1021/ja4092038.

[7] A.B. Barnes, M.L. Mak-Jurkauskas, Y. Matsuki, V.S. Bajaj, P.C. a van der Wel, R. DeRocher, J.A. Bryant, J.R. Sirigiri, R.J. Temkin, J. Lugtenburg, J. Herzfeld, R.G. Griffin, Cryogenic sample exchange NMR probe for magic angle spinning dynamic nuclear polarization, J. Magn. Reson. 198 (2009) 261–270. doi:10.1016/j.jmr.2009.03.003.

[8] M. Akke, NMR methods for characterizing microsecond to millisecond dynamics in recognition and catalysis, Curr. Opin. Struct. Biol. 12 (2002) 642–647. doi:10.1016/S0959-440X(02)00369-X.

[9] K.R. Thurber, R. Tycko, Low-temperature dynamic nuclear polarization with helium-cooled samples and nitrogen-driven magic-angle spinning, J. Magn. Reson. 264 (2016) 99–106. doi:10.1016/j.jmr.2016.01.011.

[10] T. Maly, G.T. Debelouchina, V.S. Bajaj, K. Hu, C.-G. Joo, M.L. Mak-Jurkauskas, J.R. Sirigiri, P.C. a van der Wel, J. Herzfeld, R.J. Temkin, R.G. Griffin, Dynamic nuclear polarization at high magnetic fields, J. Chem. Phys. 128 (2008) 052211. doi:10.1063/1.2833582.

[11] A.B. Barnes, G. De Paëpe, P.C. a van der Wel, K. Hu, C.-G. Joo, V.S. Bajaj, M.L. Mak-

Jurkauskas, J.R. Sirigiri, J. Herzfeld, R.J. Temkin, R.G. Griffin, High-Field Dynamic Nuclear Polarization for Solid and Solution Biological NMR, Appl. Magn. Reson. 34 (2008) 237–263. doi:10.1007/s00723-008-0129-1.

[12] T. Gullion, J. Schaefer, Rotational-echo double-resonance NMR, J. Magn. Reson. 81 (1989) 196–200. doi:10.1016/0022-2364(89)90280-1.

[13] K.A. Collier, S. Sengupta, C.A. Espinosa, J.E. Kelly, J.I. Kelz, R.W. Martin, Design and construction of a quadruple-resonance MAS NMR probe for investigation of extensively deuterated biomolecules, J. Magn. Reson. 285 (2017) 8–17. doi:10.1016/j.jmr.2017.10.002.

[14] E.O. Stejskal, J. Schaefer, J.S. Waugh, Magic-Angle Spinning and Polarization Transfer in Proton-Enhanced NMR, J. Magn. Reson. 28 (1977) 105–12. doi:https://doi.org/10.1016/0022-2364(77)90260-8.

[15] M. Ernst, A. Verhoeven, B.H. Meier, High-Speed Magic-Angle Spinning 13 C MAS NMR Spectra of Adamantane: Self-Decoupling of the Heteronuclear Scalar Interaction and Proton Spin Diffusion, J. Magn. Reson. 130 (1998) 176–185.

[16] E. Barbet-Massin, A.J. Pell, J.S. Retel, L.B. Andreas, K. Jaudzems, W.T. Franks, A.J. Nieuwkoop, M. Hiller, V. Higman, P. Guerry, A. Bertarello, M.J. Knight, M. Felletti, T. Le Marchand, S. Kotelovica, I. Akopjana, K. Tars, M. Stoppini, V. Bellotti, M. Bolognesi, S. Ricagno, J.J. Chou, R.G. Griffin, H. Oschkinat, A. Lesage, L. Emsley, T. Herrmann, G. Pintacuda, Rapid proton-detected NMR assignment for proteins with fast magic angle spinning, J. Am. Chem. Soc. 136 (2014) 12489–12497. doi:10.1021/ja507382j.

[17] K. Hu, Polarizing agents and mechanisms for high-field dynamic nuclear polarization of

frozen dielectric solids, Solid State Nucl. Magn. Reson. 40 (2011) 31–41. doi:10.1016/j.ssnmr.2011.08.001.

[18] M.-A. Geiger, A.P. Jagtap, M. Kaushik, B. Corzilius, H. Oschkinat, S.T. Sigurdsson, Efficiency of water-soluble nitroxide biradicals for dynamic nuclear polarization in rotating solids at 9.4 T: bcTol-M and cyolyl-TOTAPOL as new polarizing agents, Manuscr. Prep. (2017).

[19] A.P. Jagtap, M.-A. Geiger, D. Stöppler, M. Orwick-Rydmark, H. Oschkinat, S.T. Sigurdsson, bcTol: a highly water-soluble biradical for efficient dynamic nuclear polarization of biomolecules, Chem. Commun. 52 (2016) 7020–7023. doi:10.1039/C6CC01813K.

[20] F.J. Scott, E.P. Saliba, B.J. Albert, N. Alaniva, E.L. Sesti, C. Gao, N.C. Golota, E.J. Choi, A.P. Jagtap, J.J. Wittmann, M. Eckardt, W. Harneit, B. Corzilius, S. Th. Sigurdsson, A.B. Barnes, Frequency-agile gyrotron for electron decoupling and pulsed dynamic nuclear polarization, J. Magn. Reson. 289 (2018) 45–54. doi:10.1016/j.jmr.2018.02.010.

[21] B. Corzilius, A.A. Smith, R.G. Griffin, Solid effect in magic angle spinning dynamic nuclear polarization., J. Chem. Phys. 137 (2012) 054201. doi:10.1063/1.4738761.

[22] A.A. Smith, B. Corzilius, A.B. Barnes, T. Maly, R.G. Griffin, Solid effect dynamic nuclear polarization and polarization pathways, J. Chem. Phys. 136 (2012). doi:10.1063/1.3670019.

[23] V.K. Michaelis, T.-C. Ong, M.K. Kiesewetter, D.K. Frantz, J.J. Walish, E. Ravera, C. Luchinat, T.M. Swager, R.G. Griffin, Topical developments in high-field dynamic nuclear polarization, Isr. J. Chem. 54 (2014) 207–221. doi:10.1002/ijch.201300126.

[24] C. Song, K.-N. Hu, C.-G. Joo, T.M. Swager, R.G. Griffin, TOTAPOL: A Biradical Polarizing Agent for Dynamic Nuclear Polarization Experiments in Aqueous Media, J. Am. Chem. Soc. (2006) 11385–11390. doi:10.1021/JA061284B.

[25] F. Mentink-Vigier, S. Paul, D. Lee, A. Feintuch, S. Hediger, S. Vega, G. De Paëpe, Nuclear depolarization and absolute sensitivity in magic-angle spinning cross effect dynamic nuclear polarization, Phys. Chem. Chem. Phys. 17 (2015) 21824–21836. doi:10.1039/c5cp03457d.

[26] K.R. Thurber, R. Tycko, Perturbation of nuclear spin polarizations in solid state NMR of nitroxide-doped samples by magic-angle spinning without microwaves, J. Chem. Phys. 140 (2014) 184201.

[27] B. Corzilius, L.B. Andreas, A.A. Smith, Q.Z. Ni, R.G. Griffin, Paramagnet induced signal quenching in MAS – DNP experiments in frozen homogeneous solutions, J. Magn. Reson. 240 (2014) 113–123. doi:10.1016/j.jmr.2013.11.013.

[28] E.P. Saliba, E.L. Sesti, F.J. Scott, B.J. Albert, E.J. Choi, N. Alaniva, A.B. Barnes, Electron Decoupling with Dynamic Nuclear Polarization in Rotating Solids, J. Am. Chem. Soc. 139 (2017) 6310–6313. doi:10.1021/jacs.7b02714.

[29] D.E.M. Hoff, B.J. Albert, E.P. Saliba, F.J. Scott, E.J. Choi, M. Mardini, A.B. Barnes, Frequency swept microwaves for hyperfine decoupling and time domain dynamic nuclear polarization, Solid State Nucl. Magn. Reson. 72 (2015) 79–89. doi:10.1016/j.ssnmr.2015.10.001.

[30] P.L. Gor'kov, W.W. Brey, J.R. Long, Probe Development for Biosolids NMR Spectroscopy, Encycl. Magn. Reson. Solid-stat (2010) 141–158.

doi:10.1002/9780470034590.

[31] J. Schaefer, R.A. McKay, Multi-Tuned Single Coil Transmission Line Probe for Nuclear Magnetic Resonance Spectrometer, 1999.

[32] B.J. Albert, S.H. Pahng, N. Alaniva, E.L. Sesti, P.W. Rand, E.P. Saliba, F.J. Scott, E.J. Choi, A.B. Barnes, Instrumentation for cryogenic magic angle spinning dynamic nuclear polarization using 90 L of liquid nitrogen per day, J. Magn. Reson. 283 (2017) 71–78. doi:10.1016/j.jmr.2017.08.014.

[33] A.B. Barnes, E. Markhasin, E. Daviso, V.K. Michaelis, E.A. Nanni, S.K. Jawla, E.L. Mena, R. DeRocher, A. Thakkar, P.P. Woskov, J. Herzfeld, R.J. Temkin, R.G. Griffin, Dynamic nuclear polarization at 700MHz/460GHz, J. Magn. Reson. 224 (2012) 1–7. doi:10.1016/j.jmr.2012.08.002.

[34] J.H. Booske, R.J. Dobbs, C.D. Joye, C.L. Kory, G.R. Neil, G.S. Park, J. Park, R.J. Temkin, Vacuum electronic high power terahertz sources, IEEE Trans. Terahertz Sci. Technol. 1 (2011) 54–75. doi:10.1109/TTHZ.2011.2151610.

[35] S. Alberti, F. Braunmueller, T.M. Tran, J. Genoud, J.P. Hogge, M.Q. Tran, J.P. Ansermet, Nanosecond Pulses in a THz Gyrotron Oscillator Operating in a Mode-Locked Self-Consistent Q-Switch Regime, Phys. Rev. Lett. 111 (2013) 205101.

[36] D.T. Edwards, Y. Zhang, S.J. Glaser, S.-I. Han, M.S. Sherwin, Phase cycling with a 240 GHz, free electron laser-powered electron paramagnetic resonance spectrometer, Phys. Chem. Chem. Phys. 15 (2013) 5707. doi:10.1039/c3cp44492a.

[37] G.S. Nusinovich, Gyrotron Oscillators for Controlled Fusion Experiments, in: Introd. to

Phys. Gyrotrons, The John Hopkins University Press, 2004: pp. 215–238.

[38] Y.M. Shin, L.R. Barnett, N.C. Luhmann, Phase-shifted traveling-wave-tube circuit for ultrawideband high-power submillimeter-wave generation, IEEE Trans. Electron Devices. 56 (2009) 706–712. doi:10.1109/TED.2009.2015404.

[39] C.S. Kou, Q.S. Wang, D.B. McDermott, N.C. Luhmann, K.R. Chu, A.T. Lin, High-Power Harmonic Gyro-TWT's—Part I: Linear Theory and Oscillation Study, IEEE Trans. Plasma Sci. 20 (1992) 155–162. doi:10.1109/27.142815.

[40] C.D. Joye, M.A. Shapiro, J.R. Sirigiri, R.J. Temkin, Demonstration of a 140-GHz 1-kW confocal gyro-traveling-wave amplifier, IEEE Trans. Electron Devices. 56 (2009) 818–827. doi:10.1109/TED.2009.2015802.

[41] T. Idehara, E.M. Khutoryan, Y. Tatematsu, Y. Yamaguchi, A.N. Kuleshov, O. Dumbrajs, Y. Matsuki, T. Fujiwara, High-Speed Frequency Modulation of a 460-GHz Gyrotron for Enhancement of 700-MHz DNP-NMR Spectroscopy, J. Infrared, Millimeter, Terahertz Waves. 36 (2015) 819–829. doi:10.1007/s10762-015-0176-2.

[42] D. Yoon, M. Soundararajan, P. Cuanillon, F. Braunmueller, S. Alberti, J.P. Ansermet, Dynamic nuclear polarization by frequency modulation of a tunable gyrotron of 260 GHz, J. Magn. Reson. 262 (2016) 62–67. doi:10.1016/j.jmr.2015.11.008.

[43] J.L. Doane, Propagation and Mode Coupling in Corrugated and Smooth-Wall Circular Waveguides, Infrared Millim. Waves, Vol. 13. (1985) 123–170.

Chapter 2: Frequency-agile gyrotron for electron decoupling and pulsed dynamic nuclear polarization

Adapted from "Frequency-agile gyrotron for electron decoupling and pulsed dynamic nuclear polarization" published in the Journal of Magnetic Resonance, April 2018, pp 45-54, https://doi.org/10.1016/j.jmr.2018.02.010 by Faith J. Scott, Edward P. Saliba, Brice J. Albert, Nicholas Alaniva, Erika L. Sesti, Chukun Gao, Natalie C. Golota, Eric J. Choi, Anil P. Jagtap, Johannes J. Wittmann, Michael Eckardt, Wolfgang Harneit, Björn Corzilius, Snorri Th. Sigurdsson, and Alexander B. Barnes in collaboration with the University of Iceland, Goethe University Frankfurt, Johannes Gutenberg-Universität Mainz, and Universität Osnabrück. The first frequency-agile gyrotron built at Washington University, described here, provided the necessary electron Rabi frequency for electron decoupling in MAS-DNP NMR.

Abstract

I describe a frequency-agile gyrotron which can generate frequency-chirped microwave pulses. An arbitrary waveform generator (AWG) within the NMR spectrometer controls the microwave frequency, enabling synchronized pulsed control of both electron and nuclear spins. I demonstrate that the acceleration of emitted electrons, and thus the microwave frequency, can be quickly changed by varying the anode voltage of the electron gun. This strategy results in much faster frequency response than can be achieved by changing the potential of the electron emitter, and does not require a custom triode electron gun. The gyrotron frequency can be swept with a rate of 20 MHz/μs over a 670 MHz bandwidth in a static magnetic field. Our group has already implemented time-domain electron decoupling with dynamic nuclear polarization (DNP) and magic angle spinning (MAS) with this device [1]. In this chapter, I show frequency-swept DNP

enhancement profiles recorded without changing the NMR magnet or probe. The profile of endofullerenes exhibits a DNP profile with a <10 MHz linewidth, indicating that the device also has sufficient frequency stability, and therefore phase stability, to implement pulsed DNP mechanisms such as the frequency-swept solid effect. I describe schematics of the mechanical and vacuum construction of the device which includes a novel flanged sapphire window assembly. Finally, I discuss how commercially available continuous-wave gyrotrons can potentially be converted into similar frequency-agile high-power microwave sources.

2.1 Introduction

Dynamic nuclear polarization (DNP) is a powerful tool to increase nuclear magnetic resonance (NMR) sensitivity in which the high polarization of electron spins is transferred to nuclear spins via microwave irradiation that fulfills matching conditions [2–4]. High microwave power levels (>5 W) are required to generate significant DNP enhancements for magic angle spinning (MAS) samples at temperatures >80 Kelvin at high magnetic fields (>5 T) [5–7]. Gyrotrons, now widely commercially available, provide the requisite microwave power levels, yet can rarely be tuned quickly or pulsed [8]. Such continuous-wave (CW) gyrotrons permit only CW DNP mechanisms. Similar to the development of NMR and EPR spectroscopy from continuous wave to pulsed regimes, pulsed DNP will provide many advantages over CW approaches [1,9–12]. Although CW DNP mechanisms yield large signal enhancements for model systems at lower magnetic fields, their performance is suboptimal with higher magnetic fields, higher temperatures, and more complex samples [13,14]. Pulsed DNP transfers have considerable promise to improve DNP performance where CW mechanisms underperform [15–18]. Chirped microwave pulses have also recently enabled the first electron decoupling experiments, which attenuate hyperfine interactions and alleviate detrimental paramagnetic relaxation effects [1].

Possible microwave sources that can produce high power levels required for pulsed DNP and electron decoupling with MAS include free electron lasers, slow-wave traveling wave tubes (TWTs), gyromonotrons, gyro-TWTs, and gyro-backward wave oscillators (gyro-BWOs) [19–24]. Free electron lasers are unrivaled in their tuning range and can also be frequency and phase stable, yet occupy considerable space making their broad applicability in NMR laboratories across the world limited [25]. Slow-wave TWTs are very promising sources for EPR and DNP below 300 GHz, yet their maximum power levels are lower than gyrotrons, and the inverse scaling of the interaction cavity dimensions with higher frequencies presents considerable microfabrication challenges [26,27]. Fast-wave gyro-TWTs have successfully been developed at 140 and 250 GHz, yet their broad dissemination into the ranks of NMR spectroscopists has been hindered by the cost associated with the requisite superconducting magnets and electron beam power supplies [20,28–30]. I have chosen to instead focus on the development of frequency agile gyrotrons, which fall under the category of gyro-BWOs. Gyrotrons have numerous advantages including higher power levels (up to 1 megawatt, 100% duty cycle) and possible widespread dissemination of technology through upgrades of existing and available MAS DNP spectrometers.

Gyrotrons are especially appealing due to the experimental feasibility of implementing chirped pulses for time-domain DNP and electron decoupling, rather than hard pulses which are more commonly employed in NMR spectroscopy of spin ½ nuclei. For instance, 13 megawatts of microwave power are required to generate sufficient electron Rabi frequency (ω_{1e}) for a hard pulse to excite the 800 MHz nitroxide lineshape at 7 Tesla, given current widely available MAS DNP probes [31]. Furthermore, the wavelength of high-frequency microwaves is smaller than the sample geometries currently employed in MAS DNP experiments leading to severe

inhomogeneity of the electron Rabi frequency, and would lead to a concomitant poor performance of hard pulses. Notably, frequency chirped pulses such as adiabatic rapid passages remain effective with a high degree of ω_{1e} inhomogeneity [9,10]. Microwave resonance structures and focusing strategies (i.e. TE_{01} resonators and Teflon lenses) are being developed by our group and others, and could provide both uniform and intense ω_{1e} fields required for pulsed DNP. However, I note that their applicability will most likely be restricted to sample-limited applications, as larger samples currently provide higher sensitivity in MAS DNP experiments. Gyrotrons which exhibit fast frequency tuning, or pulsing, include those described by Idehara et al., Alberti et al., and the device I present herein [32–34]. In this chapter I describe the mechanical, vacuum, and electrical design of a frequency-agile gyrotron which has previously been employed in pulsed electron decoupling experiments [1]. I also measure frequency swept DNP enhancement profiles of various polarizing agents using the gyrotron. Importantly, the DNP enhancement profiles of an endofullerene, $N@C_{60}$, indicate that the gyrotron has the frequency and phase stability required to perform time domain DNP transfers such as the integrated solid effect. Finally, I conclude with a discussion of how currently available spectrometers could possibly be upgraded to provide similar frequency agility and a concomitant acceleration of the field of MAS DNP into the pulsed regime.

2.2 Design

2.2.1 Overview

The gyrotron is shown within the context of the DNP-MAS NMR spectrometer (**Figure 1.5**), of which many components were custom-built such as the NMR probe, cryostat, heat-exchanger, and corrugated waveguide transmission line. Corrugated transmission line transmits microwave power from the gyrotron to the NMR probe. A cryostat insulates the NMR superconducting magnet and facilitates cryogenic MAS <6 K [35,36]. The DNP NMR probe includes a four-

channel transmission line circuit resonating at 300.184 MHz (^{1}H), 75.495 MHz (^{13}C), 30.427 MHz (^{15}N), and 121.516 MHz (^{31}P) [37,38]. A Tecmag Redstone spectrometer (Tecmag Inc., Houston TX), drives each channel and includes an arbitrary waveform generator (AWG) to generate shaped microwave pulses.

The potential waveform from the AWG is amplified 1000:1 by a low capacitance, high voltage Trek 5/80-L linear amplifier (Trek, Lockport, NY). The amplifier output is connected to the gyrotron anode, as shown in **Figures 2.1c** and **2.2a**. An electron beam is emitted from a magnetron injection gun (MIG), and compressed by the magnetic field gradient into the interaction cavity. A portion of the electron beam power is deposited into the TE_{52q} cylindrical resonator. Microwaves are directed out of the gyrotron by the internal mode converter while the electron beam continues up through the gyrotron body. Finally, the remaining electron beam energy is absorbed at the grounded collector.

2.2.2 Electrical isolation and frequency agility

The amplifier driven by the AWG is connected to the anode by a low-capacitance wire (pseudo-colored in yellow for clarity, **Figure 2.2a**). This high-voltage wire is isolated to reduce stray circuit capacitance. The cathode, which emits the electron beam, is connected to a separate high-voltage, high-power (4 kW) supply (**Figures 2.1c** and 2.**2b**) (Spellman, Hauppage, NY). Note that the capacitance of the cathode power supply is very large to maintain a stable potential, yet prevents the generation of quickly-swept microwave waveforms via control of only the cathode potential.

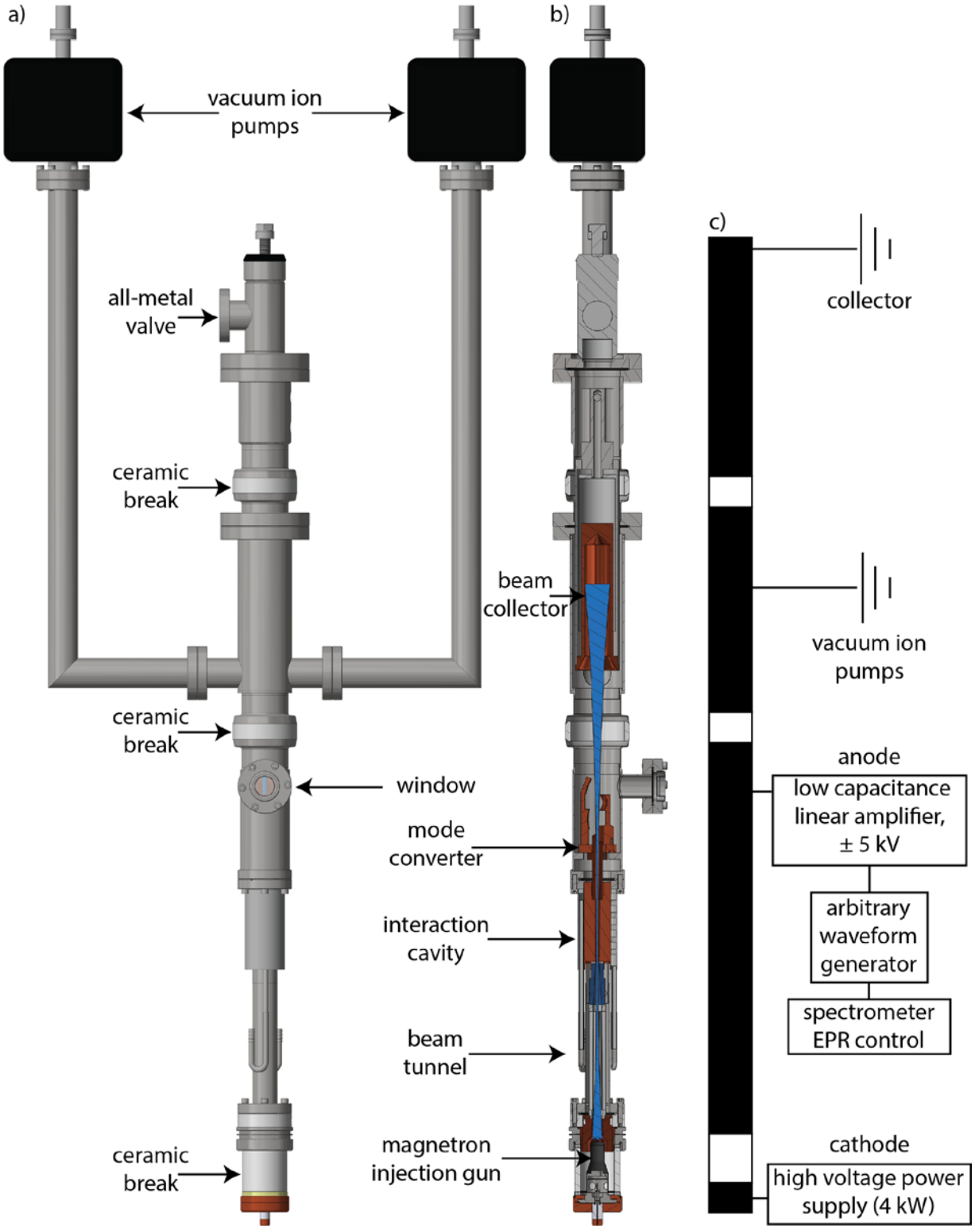

Figure 2.1 Schematics of the frequency-agile gyrotron a) full view and b) cross section. c) Electronic schematic showing the anode and cathode connections for frequency agility. Ceramic electrical breaks are shown in white.

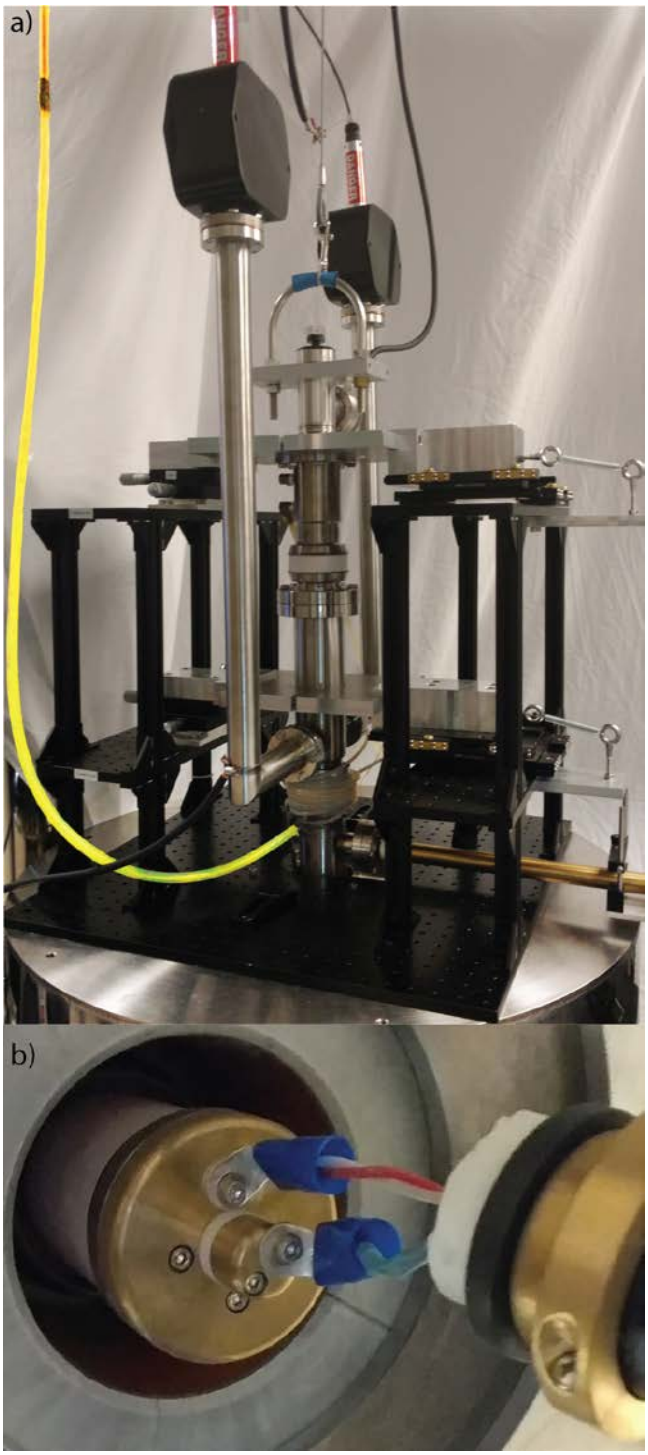

Figure 2.2 a) Photograph of the gyrotron in the magnet. The anode is connected to the low capacitance amplifier by cord highlighted in yellow. Black alignment stages are mounted to the top of the magnet. b) Cathode connection to high-voltage power supply.

The anode amplifier has a low power and voltage requirement which permits a fast slew rate of 1000 V/μs due to a low internal capacitance. Therefore the potential of the anode can be changed

quickly and results in microwave output frequency agility of up to 20 MHz/μs. This allows for frequency jumps from the DNP matching condition to the electron spin resonance for electron decoupling [1,31], and should permit coherent electron spin manipulation with adiabatic chirped pulses.

Ceramic breaks allow for electrical isolation between different sections of the gyrotron (**Figure 2.1c**). Vacuum ion pumps must be grounded to function properly and are electrically isolated from the collector and anode. The collector is also grounded so that the electron beam colliding with its surface does not accrue a negative charge. Note that the collector must be kept electrically separated from the anode to permit fast microwave frequency tuning.

The microwave output frequency is partially determined by the acceleration potential of electron emission. The electron beam is generated by a barium impregnated tungsten ring within the MIG and carries 190 mA of current. The potential between the anode and cathode is maintained between 9 and 17 kV. This high potential accelerates electrons to relativistic speeds. The associated increase in electron mass results in a lower microwave frequency according to the cyclotron frequency equation:

$$\Omega = \frac{eB_0}{m} \qquad \text{[eq. 1]}$$

where Ω is the cyclotron resonance frequency, e is the charge of the electron, B_0 is the magnetic field at the interaction cavity, and m is the relativistic electron mass [24]. Within the interaction cavity the electron beam deposits power into a cylindrical microwave mode. This TE_{52q} mode supports a continuous tuning bandwidth over a frequency range of 197.2 to 198.4 GHz, which can be controlled with 1 MHz precision by adjusting the potential across the MIG. Here, the q

subscript refers to axial modes present along the long axis of the cylindrical resonator (**Figure 2.3a**) [8,22].

2.2.3 Interaction cavity

The cavity radius is 2.542 mm, optimized for interaction with the electron beam. The magnetic field gradient focuses the electron beam at a compression factor of 28 for optimal overlap with the TE_{52q} mode [8]. The compression factor is defined as R_{MIG}/R_C where R_{MIG} is the beam radius at the MIG and R_C is the beam radius at the interaction cavity. Ohmic losses in the copper cavity walls generate heat. If the cavity is sufficiently heated, the cavity radius and frequency change concomitantly [39]. For this reason, the cavity is cooled by a water channel within the stainless steel outer jacket (**Figure 2.3c**). The 30 mm long interaction cavity supports a large continuous frequency bandwidth, here explored from 197.2 GHz to 198.4 GHz to allow for electron paramagnetic resonance (EPR) or DNP excitation of several radicals. The cavity can support up to 0.67 GHz bandwidth for a fixed magnetic field, and the gyrotron can access additional frequency ranges by adjusting the primary gyrotron magnetic field. In this way, the gyrotron can excite EPR/DNP transitions for a variety of different radicals without changing the NMR spectrometer magnetic field.

Achieving continuous tuning of greater than 1 GHz with gyrotrons requires access to hybridized axial modes within in the interaction cavity (**Figure 2.3a**) [8,22]. Therefore, I implemented a cavity with a length of 30 mm (20 λ for 198 GHz electromagnetic radiation in a vacuum), which supports hybridized axial modes. After the straight section of the interaction cavity, the walls taper away from the center for 37 mm until the Vlasov launcher of the internal mode converter. The taper prevents parasitic oscillations as the beam expands in the weaker magnetic field above the interaction cavity.

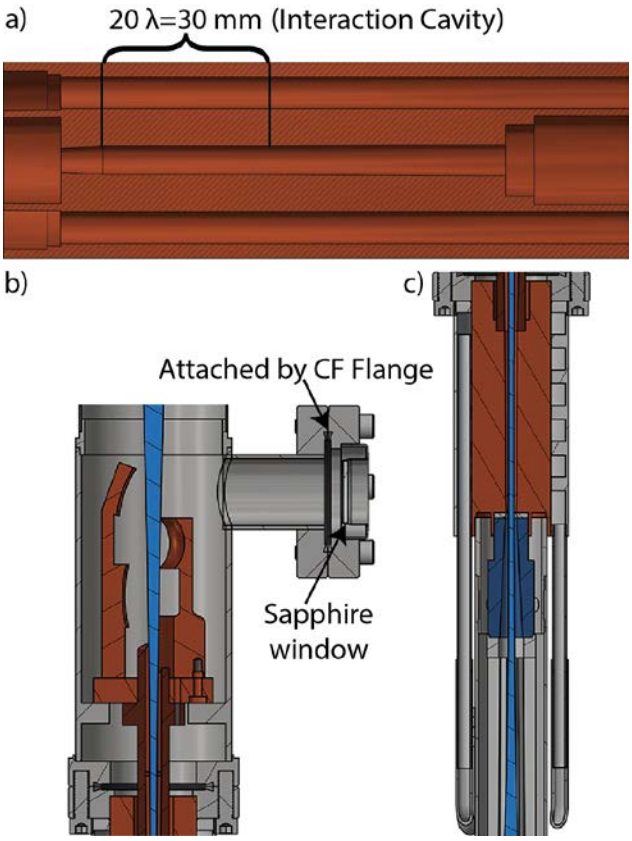

Figure 2.3 Schematic of gyrotron a) cavity b) internal mode converter, and c) interaction cavity in context with beam tunnel.

2.2.4 Internal mode converter

The microwaves generated in the interaction cavity (**Figure 2.3b**) propagate inside the gyrotron in the TE_{52q} mode, which is not supported by an overmoded corrugated transmission line [40]. For this reason, it is desirable to convert the microwave output into a beam of high Gaussian content which couples with high efficiency to the HE_{11} mode supported within the waveguide [8]. The TE_{52q} mode is broadcasted by a Vlasov launcher and further shaped by an off-axis parabolic mirror and three concave mirrors [24,41]. The Vlaslov launcher and mirrors are defined as the internal mode converter. All portions of the internal mode converter are machined in copper so that the microwaves can reflect off the surface in a quasi-optical manner. The

internal mode converter is specifically designed for the TE_{52q} mode; other modes will not be converted efficiently into a Gaussian-like beam.

2.2.5 Interaction cavity and internal mode converter deficiencies

The ceramic break above the window reaches up to 82°C during nominal operation despite plastic water cooling lines, as shown in **Figure 2.2a**. This indicates that a portion of the microwave power is trapped inside the gyrotron body and absorbed into the ceramic break as heat. There are several possible reasons why microwaves may be misdirected inside the tube. First, mode excitation in the cavity may not be the expected TE_{52q} mode and is, therefore, not properly reflected by the mode converter. However the TE_{52q} mode was specifically chosen for operation because there are no competing modes nearby in frequency [8]. Second, a cylindrical section between the interaction cavity and the Vlasov launcher could act as a secondary cavity and generate microwaves in a competing mode. Third, gaps in the tapered waveguide between the cavity and the Vlasov launcher or misalignments in the interaction cavity could cause a significant portion of microwaves to be scattered away from the window. These potential sources of error will be addressed in the next generation of the frequency-agile gyrotron, currently under fabrication.

2.2.6 Output window

The microwave output port is a sapphire window cut perpendicular to the crystallographic C-axis, with a width of 0.0685 mm to optimally transmit 198 GHz microwaves. An incorrect window thickness would reflect the majority of the microwaves back into the gyrotron body. However, the window has been tested independently of the gyrotron and found to be transparent at 198 GHz. The sapphire is brazed to a Kovar sleeve, which is in turn welded to a 316 stainless

steel CF flange to allow for window removal or replacement as needed. The exchangeable window is advantageous compared to welding the window directly to the gyrotron body.

2.2.7 Alignment apparatus

The purpose of the alignment stage is to adjust the gyrotron position inside the super-conducting magnet to optimize interaction of the electron beam with the interaction cavity. For maximum microwave power output, the electron beam should run parallel to the axis of the interaction cavity, and aligned concentrically within the cavity. Misalignment on the scale of fractions of a millimeter lead to drastic reduction in microwave conversion efficiency. The electron beam should overlap with the first radial maximum of the TE_{52q} mode, which is experimentally achieved by changing both the alignment stages and the magnetic field at the electron gun [8]. The gyrotron's alignment apparatus has been optimized since its first installation. The gyrotron was originally held in place by an arm attached to the top of the magnet and mounted on a table underneath the primary magnet. The top arm was supported by two crossed x-stages such that the cavity's location in the x-y plane could be adjusted in addition to the angle with respect to the electron beam. The bottom stage also held two orthogonal translation stages for alignment, on which a Delrin high-voltage plug was mounted. The high-voltage plug consisted of two brass cylinders fitted with finger-stock separated by a concentric Teflon cylinder. This first design had a number of problems: (i) finger stock was employed for connection of the high-voltage MIG, but often lost electrical connection during the alignment process, (ii) the numbers on the translation stages underneath the magnet could not be read by eye, making precise alignment difficult, and (iii) the high voltage from the power supply occasionally arced to the grounded aluminum table underneath the magnet. For these reasons, a new alignment stage was designed.

The new alignment apparatus features two sets of translation stages mounted to the top of the superconducting magnet, as shown in **Figure 2.2a**. The lower stage support is just above the vacuum extension arms, and the upper stage support is clamped around the top flange of the collector. Alignment is achieved by axial sliding stages shown on the right of the magnet in **Figure 2.2a**. Furthermore, heavy-duty springs accommodate motion when the internal springs of the translation stages are too weak to move the gyrotron.

Although there have been no arcs external to the gyrotron since the plug and alignment stages were replaced, a round Plexiglas shield prevents access to the bottom of the magnet for safety. A second Plexiglas shield sits around the top of the magnet to protect the user from the anode. The upper shield is not shown in **Figure 2.2** because the glare concealed gyrotron details.

2.2.8 Fabrication and implementation

The MIG was purchased from Bridge12 Technologies, Inc. (Framingham, MA). Unless otherwise stated, parts were machined at Washington University in St. Louis from 316 stainless steel or oxygen-free high conductivity (OFHC) copper. Vacuum-tight CF flanges, ceramic breaks, and the all-metal valve were purchased from MDC (Hayward, CA). The internal mode converter was machined at Ramco Machining (Rowley, MA), and the interaction cavity was machined at Midwest Precision Tool and Die (Sioux Falls, SD). The upper beam tunnel was machined in SiC by International Ceramics Engineering (Worchester, MA).

At every welding and brazing step, joints were vacuum tested to ensure proper seals. When all components were complete, each was cleaned meticulously with acetone followed by ethanol to remove machining oils [42]. Prior to operation in the magnet, the gyrotron was baked out under vacuum by wrapping in fiberglass heating tape and covering in aluminum foil. The gyrotron body was heated to 200°C and the collector was heated to 350°C for six days. The MIG was then

attached for a second vacuum processing session at 100°C. Subsequently the emitter was activated under a DC potential of 0.3-2.2 V and an AC heater current up to 2.3 A.

2.3. Results

2.3.1 Power output and voltage frequency sweeps

The gyrotron microwave power and frequency over a range of 670 MHz (or 4.5 kV) are shown in **Figure 2.4**. To measure power output, a section of corrugated transmission line was removed and a water load of 500 mL was placed in the path of the transmission line at 1 m from the gyrotron window. The water load was stirred continuously and the temperature rise was measured with a thermocouple to determine the microwave power. Microwave frequency was measured with a commercial frequency measurement system (Bridge 12 Technologies, Inc, Framingham, MA). The microwave power output peaked at 27 W, but a frequency span of consistent power at 12-13 W is more desirable for frequency-agile DNP sequences such as electron decoupling. 36 W of power was measured directly at the output window, indicating significant power is lost in the first meter of the transmission line, due to poor mode quality emitted from the gyrotron.

This gyrotron was previously employed in the first utilization of chirped microwave pulses in MAS NMR and concomitant demonstration of electron decoupling [1]. The average NMR linewidth change due to electron decoupling from that study is shown in blue in **Figure 2.4a** [1]. Note that electron decoupling was demonstrated in a bandwidth of constant microwave power output.

The dependence of the microwave frequency on voltage is remarkably linear (**Figure 2.4b**) [34,43]. The frequency measurement system records at a rate of 2 sweeps per second, so this

system cannot directly measure the fastest frequency sweeps. Frequency agility is inferred from electron decoupling performance and the observed change in anode voltage [1].

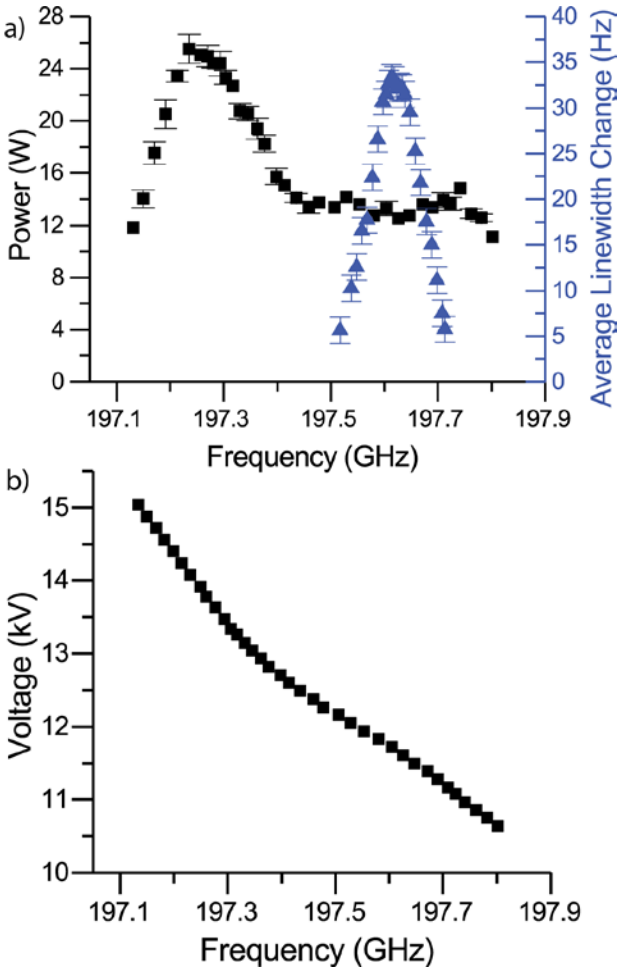

Figure 2.4 a) Gyrotron output power over tuning bandwidth. Power output is stable over a 300 MHz range and present over a 670 MHz (197.13-197.80 GHz) range. Error bars less than 0.5 W are not shown. Average linewidth change due to electron decoupling (Hz) reproduced with permission from the Journal of the American Chemical Society [1]. b) Response to change in cathode voltage for the same frequency range.

2.3.2 DNP enhancement profiles

Frequency-stepped DNP enhancement profiles were recorded for Finland trityl radical, N@C_{60} endofullerene, and bcTol-M on the DNP spectrometer (**Figure 2.5**) [44,45]. Two trityl samples at concentrations of 10 mM and 40 mM and bcTol-M at a concentration of 20 mM were characterized; all except the fullerene contained 4 M [^{13}C, ^{15}N] urea in 60% glycerol-d_8, 30% D_2O, and 10% H_2O. The Finland trityl radical was purchased from Oxford Instruments

(Abingdon, UK). N@C_{60} endofullerene was prepared and purified following a previously described procedure [46,47]. This useful reference S=3/2 material is stable at room temperature [48,49]. The final powder contained 170 ppm of N@C_{60} within a cubic lattice of C_{60} (C_{60}:N@C_{60}). ^{13}C DNP NMR was performed on natural abundance ^{13}C nuclei in the C_{60} fullerene. I feature the negative enhancement in this chapter, but our group has observed a positive enhancement 150 MHz away. This confirms the DNP mechanism for N@C_{60} endofullerene is the solid effect.

All profiles were recorded on a custom-built 4-channel NMR DNP MAS probe housing 3.2 mm diameter cylindrical sample containers, or rotors, at a B_0 of 7.05 T. The ^{1}H carrier frequency was 300.184 MHz and the ^{13}C frequency was 75.495 MHz. Specific experimental parameters are given in **Table 2.1**. Saturation trains were used to destroy any residual polarization before experiments. The DNP polarization transfer time is defined as τ_{pol}, and the power of the gyrotron was 13-16 W. The temperature was 90 K for all profiles. Profiles were generated by taking individual spectra at varying microwave frequencies and using DMFit [50] to find the areas of resonances recorded with and without microwaves.

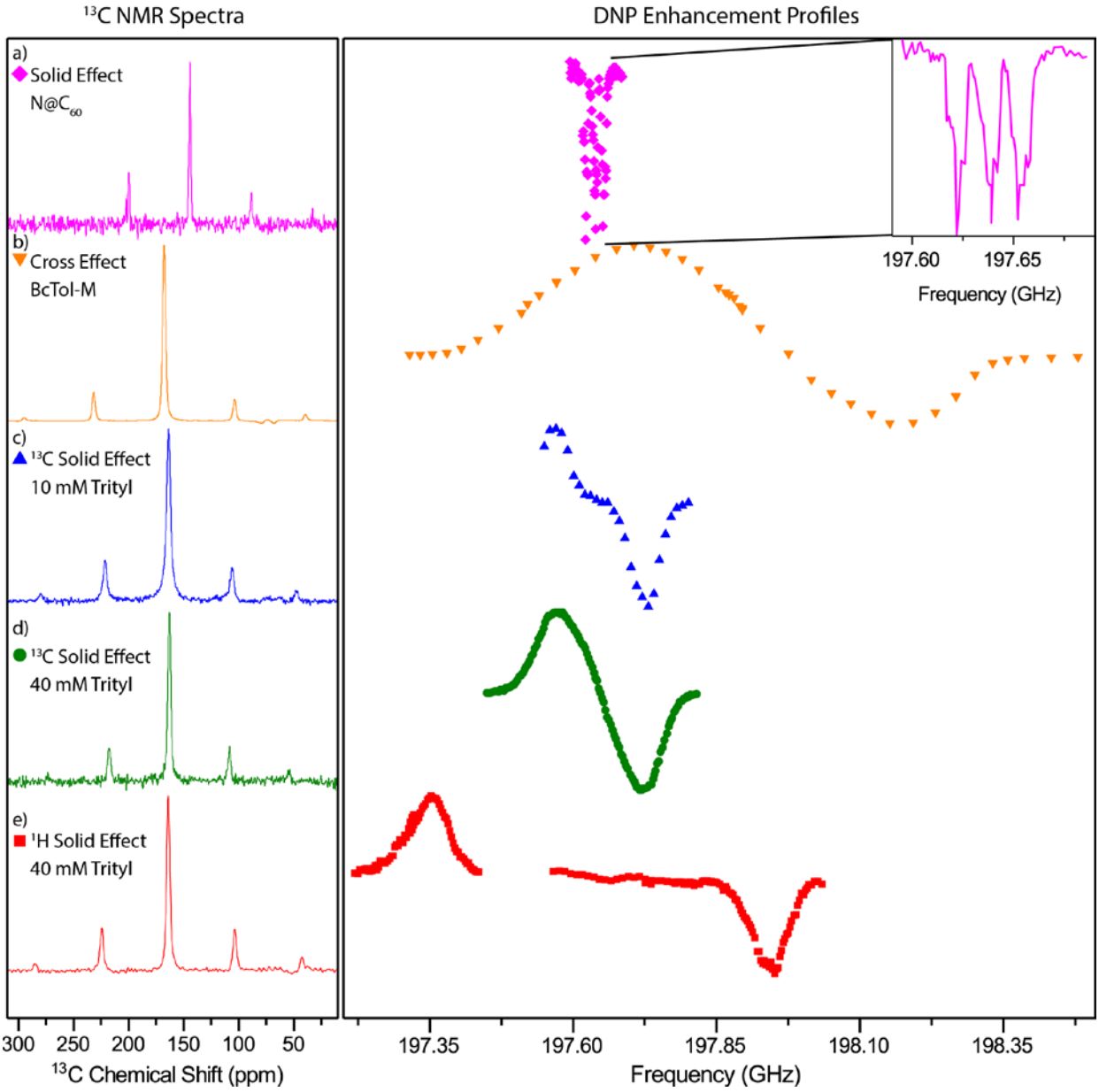

Figure 2.5 The left panel shows DNP-enhanced spectra of a) N@C_{60} endofullerene polarized by solid effect and 4 M [^{13}C, ^{15}N] urea polarized by: b) cross effect to ^{1}H and CP with bcTol-M at 20 mM, c) solid effect directly to ^{13}C with trityl at 10 mM, d) solid effect to ^{13}C with trityl at 40 mM, and e) solid effect to ^{1}H and CP with trityl at 40 mM. The right panel shows the full enhancement profiles, NMR signal areas vs. microwave irradiation frequency, of each radical. The inset shows a larger scale negative enhancement profile of the N@C_{60} endofullerene. Each of the areas are plotted as a function of microwave frequency.

Table 2.1 Experimental NMR parameters.

Radical Profile	Sequence	ν_{1H} (kHz)	ν_{13C} (kHz)	τ (μs)	ν_{rot} (kHz)	τ_{pol} (s)	Transients	Maximum Enhancement	DNP Mechanism
bcTol-M	CPMAS	67	83	215	4.6	3	8	342	Cross Effect
10 mM trityl	Hahn echo	67	83	250	4.0	7	8	8	Solid Effect
40 mM trityl	Hahn echo	67	83	250	4.0	7	4	242	Solid Effect /Cross Effect
40 mM trityl	CPMAS	67	83	250	4.0	7	4	21	Solid Effect
$N@C_{60}$	Bloch decay	-	83	-	4.2	30	8	1.3	Solid Effect

$\nu_{1H}=\omega_{1,1H}/2\pi$, $\nu_{13C}=\omega_{1,13C}/2\pi$, τ=Hahn echo delay time, ν_{rot}=rotation frequency, τ_{pol}=polarization time.

2.3.3 Spectral purity

The spectral purity is difficult to directly observe with the frequency measurement system due to the instability in the mixer's local oscillator (LO) frequency. As the frequency of the local oscillator changes, so does the difference between the LO signal and the gyrotron output frequency. This results in the appearance of a broadened linewidth as the receiver sweeps across the selected frequency window. However, here I introduce a novel experiment to determine the spectral purity of microwave sources which should have a broad applicability. The spectral purity can be seen indirectly by overlaying DNP enhancement profile of $N@C_{60}$ with the frequency-shifted EPR signal (**Figure 2.6**). The echo-detected field-sweep EPR spectrum of $N@C_{60}$ was recorded on a 263 GHz Bruker Elexsys E780 puled EPR spectrometer (Bruker, Billerica, MA) using a custom-built resonator. Pulses with a Rabi frequency of 5 MHz were used, the echo delay was set to 600 ns. The superconducting sweep coil of a Bruker Ascent DNP magnet (B_0 = 9.4 T) was used for the field-sweep (sweep rate: 0.01 mT/s).

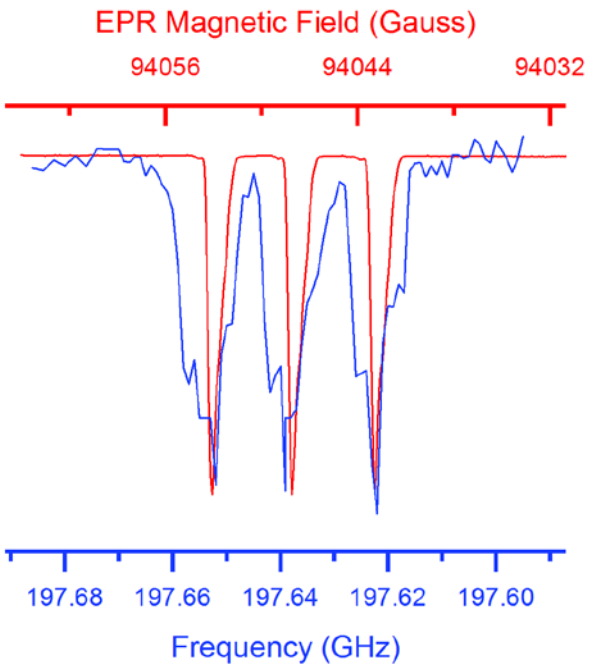

Figure 2.6 The top axis and red spectrum show the EPR echo detected field sweep of N@C_{60} endofullerene. The bottom axis and blue spectrum show the enhancement profile of N@C_{60} endofullerene.

Temperature was regulated at 100 K inside a cryostat (Oxford Instruments). N@C_{60} endofullerene is unique in a sense that the active paramagnetic species is a nitrogen atom in its electronic ground state (S=3/2) which is trapped inside the highly symmetric cavity of a C_{60} fullerene. This results in an effectively isotropic EPR spectrum with a *g* value close to the free electron and 15.8 MHz hyperfine coupling to the central ^{14}N. If the gyrotron emits a wider range of frequencies over the time course of the experiment (minutes), each peak of the resolved ^{14}N hyperfine triplet in the enhancement profile will be broadened with respect to the EPR spectrum. The enhancement profile of the fullerene, taken together with the EPR spectrum exhibiting 2 MHz broad resonance features, indicates that the spectral bandwidth is a maximum of 7 MHz. The spectral purity is most likely far more narrow at shorter timescales. For instance, the frequency, and therefore phase, should be stable over the 14 microsecond, 100 MHz microwave chirps employed for electron decoupling [1]. I therefore expect frequency-agile gyrotrons will

have the requisite frequency and phase stability to perform chirped microwave pulses also for pulsed DNP transfers.

2.3.4 Microwave duty cycle

The gyrotron is most often operated at a 100% duty cycle, but here I show that the power output can also be gated on a microsecond timescale. This is achieved by quickly jumping the acceleration voltage of the MIG between a potential which yields power emission, and a potential which does not support microwave power generation. In **Figure 2.7**, the duty cycle is synchronized with the rotor period. Rotor period synchronization alone did not yield larger DNP enhancement, however, this on/off microwave control is a useful feature that could be utilized in rotor-synchronized EPR and DNP experiments in the future.

2.3.5 Upgrading continuous-wave gyrotrons

Dozens of continuous-wave gyrotrons are already in use for DNP, and many of these gyrotrons could be modified for fast frequency chirps using similar voltage agility techniques to those described here. The anode and cavity body are often electrically connected in gyrotrons currently implemented for DNP, but separated from the collector to measure body current. Therefore the anode would need to be connected to a high voltage power supply, rather than connected to ground via a resistor which is the more common arrangement. In principle, such an upgrade would require modifications to the control system and wiring, yet would not require a new gyrotron tube, super conducting magnet, or cathode power supply. The bandwidth of commercially available gyrotrons typically employed for MAS DNP is in the range of 50-130 MHz; not as wide a tuning range as the device I present in this chapter, but still sufficient to chirp through narrow-line radicals. Such modified devices could also in principle implement the rotor-synchronized microwave gating demonstrated in **Figure 2.7**. If upgrades to DNP

spectrometers already in use lead to improved microwave chirping and gating abilities, then the progress of DNP from continuous to pulsed regimes could be substantially accelerated.

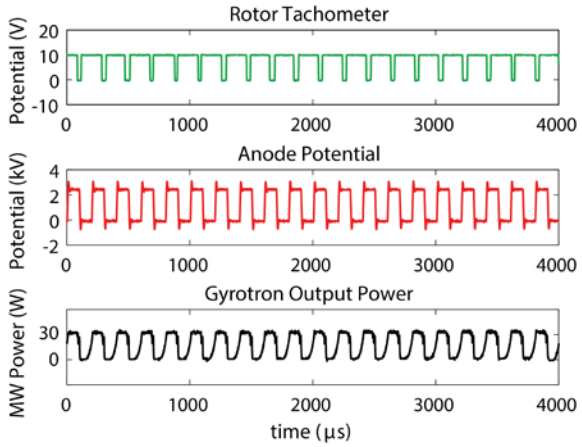

Figure 2.7 Anode voltage and microwave duty cycle synchronized to the rotor period.

2.4. Conclusion and outlook

Frequency-agile gyrotrons enable a new class of experiments for DNP-NMR spectroscopy. Control of the microwave frequency with our spectrometer allows for chirped microwave pulses in conjunction with MAS NMR. The frequency agility of the gyrotron depends on a low capacitance circuit equipped with an arbitrary waveform generator on the electrically isolated anode. The interaction cavity is long enough to support hybridized axial modes, yielding a continuous microwave power output over a spectral width of 670 MHz at a single magnetic field. The frequency response is linear with respect to voltage, and the microwave power is nearly constant over a 100 MHz tuning range previously employed for electron decoupling. The gyrotron is used to characterize a variety of radicals including Finland radical trityl, bcTol-M, and N@C_{60} endofullerene. From the fullerene EPR spectrum and DNP enhancement profile, I determine that the spectral bandwidth of the gyrotron is no more than 7 MHz over a timescale of minutes, but on a microsecond timescale, phase and frequency stability are sufficient for electron

decoupling experiments. The gyrotron power emission can be gated with MAS frequency to enable rotor synchronized DNP.

Importantly, I describe how existing DNP spectrometers could be upgraded to permit similar microwave-chirped and microwave-gated control. Improvements in frequency agile gyrotron design will result in higher microwave power levels than the 36 W generated in this device. Applications of frequency agile gyrotrons include electron decoupling and frequency-chirped pulsed DNP. Frequency agile gyrotron technology, if adopted, could usher in a paradigm shift from CW to time domain DNP.

References

[1] E.P. Saliba, E.L. Sesti, F.J. Scott, B.J. Albert, E.J. Choi, N. Alaniva, A.B. Barnes, Electron Decoupling with Dynamic Nuclear Polarization in Rotating Solids, J. Am. Chem. Soc. 139 (2017) 6310–6313. doi:10.1021/jacs.7b02714.

[2] C. Song, K.-N. Hu, C.-G. Joo, T.M. Swager, R.G. Griffin, TOTAPOL: A Biradical Polarizing Agent for Dynamic Nuclear Polarization Experiments in Aqueous Media, J. Am. Chem. Soc. (2006) 11385–11390. doi:10.1021/JA061284B.

[3] D. Lee, E. Bouleau, P. Saint-Bonnet, S. Hediger, G. De Paëpe, Ultra-low temperature MAS-DNP, J. Magn. Reson. 264 (2016) 116–124. doi:10.1016/j.jmr.2015.12.010.

[4] V. Weis, M. Bennati, M. Rosay, J.A. Bryant, R.G. Griffin, High-field DNP and ENDOR with a novel multiple-frequency resonance structure, J. Magn. Reson. 140 (1999) 293–299. doi:10.1006/jmre.1999.1841.

[5] A.B. Barnes, E. Markhasin, E. Daviso, V.K. Michaelis, E.A. Nanni, S.K. Jawla, E.L. Mena, R. DeRocher, A. Thakkar, P.P. Woskov, J. Herzfeld, R.J. Temkin, R.G. Griffin,

Dynamic nuclear polarization at 700MHz/460GHz, J. Magn. Reson. 224 (2012) 1–7. doi:10.1016/j.jmr.2012.08.002.

[6] L.R. Becerra, G.J. Gerfen, R.J. Temkin, D. Singel, R.G. Griffin, Dynamic nuclear polarization with a cyclotron resonance maser at 5 T, Phys. Rev. Lett. 71 (1993) 3561–3564. doi:10.1103/PhysRevLett.71.3561.

[7] Y. Matsuki, T. Idehara, J. Fukazawa, T. Fujiwara, Advanced instrumentation for DNP-enhanced MAS NMR for higher magnetic fields and lower temperatures, J. Magn. Reson. 264 (2016) 107–115. doi:10.1016/j.jmr.2016.01.022.

[8] A.B. Barnes, E.A. Nanni, J. Herzfeld, R.G. Griffin, R.J. Temkin, A 250 GHz gyrotron with a 3 GHz tuning bandwidth for dynamic nuclear polarization, J. Magn. Reson. 221 (2012) 147–153. doi:10.1016/j.jmr.2012.03.014.

[9] M. Garwood, L. DelaBarre, The Return of the Frequency Sweep: Designing Adiabatic Pulses for Contemporary NMR, J. Magn. Reson. 153 (2001) 155–177. doi:10.1006/jmre.2001.2340.

[10] Ē. Kupce, R. Freeman, Optimized Adiabatic Pulses for Wideband Spin Inversion, J. Magn. Reson. Ser. A. 118 (1996) 299–303. doi:10.1006/jmra.1996.0042.

[11] I. Kaminker, R.P. Barnes, S.-I. Han, Arbitrary waveform modulated pulse EPR at 200 GHz, J. Magn. Reson. 279 (2017) 81–90. doi:10.1016/j.jmr.2017.04.016.

[12] S.K. Jain, G. Mathies, R.G. Griffin, Off-resonance NOVEL, J. Chem. Phys. 147 (2017).

[13] V.S. Bajaj, C.T. Farrar, M.K. Hornstein, I. Mastovsky, J. Vieregg, J.A. Bryant, B. Eléna, K.E. Kreischer, R.J. Temkin, R.G. Griffin, Dynamic nuclear polarization at 9T using a novel 250GHz gyrotron microwave source, J. Magn. Reson. 160 (2003) 85–90. doi:10.1016/S1090-7807(02)00192-1.

[14] A. Henstra, T.-S. Lin, J. Schmidt, W.T. Wenckebach, High Dynamic Nuclear Polarization at Room Temperature, 165 (1990) 6–10.

[15] A. Bornet, J. Milani, B. Vuichoud, A.J. Perez Linde, G. Bodenhausen, S. Jannin, Microwave Frequency Modulation to Enhance Dissolution Dynamic Nuclear Polarization, Chem. Phys. Lett. 602 (2014) 63–67. doi:10.1016/j.cplett.2014.04.013.

[16] Y. Hovav, A. Feintuch, S. Vega, D. Goldfarb, Dynamic nuclear polarization using frequency modulation at 3.34 T, J. Magn. Reson. 238 (2014) 94–105. doi:10.1016/j.jmr.2013.10.025.

[17] T. V. Can, R.T. Weber, J.J. Walish, T.M. Swager, R.G. Griffin, Frequency-Swept Integrated Solid Effect, Angew. Chemie - Int. Ed. 56 (2017) 6744–6748. doi:10.1002/anie.201700032.

[18] S. Un, T.F. Prisner, R.T. Weber, M.J. Seaman, K.W. Fishbein, A.E. McDermott, D. Singel, R.G. Griffin, K.W. Fishbeina, Pulsed dynamic nuclear polarization at 5 T, Chem. Phys. Lett. 189 (1992) 54–59. doi:10.1016/0009-2614(92)85152-Z.

[19] L.R. Becerra, G.J. Gerfen, B.F. Bellew, J.A. Bryant, D.A. Hall, S.J. Inati, R.T. Weber, S. Un, T.F. Prisner, A.E. McDermott, K.W. Fishbein, K.E. Kreischer, R.J. Temkin, D.J. Singel, R.G. Griffin, A Spectrometer for Dynamic Nuclear-Polarization and Electron-Paramagnetic-Resonance at High-Frequencies, J. Magn. Reson. Ser. A. 117 (1995) 28–40.

[20] E.A. Nanni, S.M. Lewis, M.A. Shapiro, R.G. Griffin, R.J. Temkin, Photonic-band-gap traveling-wave gyrotron amplifier, Phys. Rev. Lett. 111 (2013) 1–5. doi:10.1103/PhysRevLett.111.235101.

[21] S. Alberti, F. Braunmueller, T.M. Tran, J. Genoud, J.P. Hogge, M.Q. Tran, J.P. Ansermet, Nanosecond Pulses in a THz Gyrotron Oscillator Operating in a Mode-Locked Self-

Consistent Q-Switch Regime, Phys. Rev. Lett. 111 (2013) 205101.

[22] A.C. Torrezan, S.T. Han, I. Mastovsky, M.A. Shapiro, J.R. Sirigiri, R.J. Temkin, A.B. Barnes, R.G. Griffin, Continuous-Wave Operation of a Frequency-Tunable 460-GHz Second-Harmonic Gyrotron for Enhanced Nuclear Magnetic Resonance, IEEE Trans. Plasma Sci. 38 (2010) 1150–1159. doi:10.1109/tps.2010.2046617.

[23] J.H. Booske, R.J. Dobbs, C.D. Joye, C.L. Kory, G.R. Neil, G.S. Park, J. Park, R.J. Temkin, Vacuum electronic high power terahertz sources, IEEE Trans. Terahertz Sci. Technol. 1 (2011) 54–75. doi:10.1109/TTHZ.2011.2151610.

[24] G.S. Nusinovich, Gyrotron Oscillators for Controlled Fusion Experiments, in: Introd. to Phys. Gyrotrons, The John Hopkins University Press, 2004: pp. 215–238.

[25] D.T. Edwards, Y. Zhang, S.J. Glaser, S.-I. Han, M.S. Sherwin, Phase cycling with a 240 GHz, free electron laser-powered electron paramagnetic resonance spectrometer, Phys. Chem. Chem. Phys. 15 (2013) 5707. doi:10.1039/c3cp44492a.

[26] C.D. Joye, A.M. Cook, J.P. Calame, D.K. Abe, A.N. Vlasov, I.A. Chernyavskiy, K.T. Nguyen, E.L. Wright, D.E. Pershing, T. Kimura, M. Hyttinen, B. Levush, Demonstration of a high power, wideband 220-GHz traveling wave amplifier fabricated by UV-LIGA, IEEE Trans. Electron Devices. 61 (2014) 1672–1678. doi:10.1109/TED.2014.2300014.

[27] Y.M. Shin, L.R. Barnett, N.C. Luhmann, Phase-shifted traveling-wave-tube circuit for ultrawideband high-power submillimeter-wave generation, IEEE Trans. Electron Devices. 56 (2009) 706–712. doi:10.1109/TED.2009.2015404.

[28] C.S. Kou, Q.S. Wang, D.B. McDermott, N.C. Luhmann, K.R. Chu, A.T. Lin, High-Power Harmonic Gyro-TWT's—Part I: Linear Theory and Oscillation Study, IEEE Trans. Plasma Sci. 20 (1992) 155–162. doi:10.1109/27.142815.

[29] E.N. Comfoltey, M.A. Shapiro, J.R. Sirigiri, R.J. Temkin, Design of an overmoded W-band TWT, 2009 IEEE Int. Vac. Electron. Conf. IVEC 2009. (2009) 127–128. doi:10.1109/IVELEC.2009.5193391.

[30] C.D. Joye, M.A. Shapiro, J.R. Sirigiri, R.J. Temkin, Demonstration of a 140-GHz 1-kW confocal gyro-traveling-wave amplifier, IEEE Trans. Electron Devices. 56 (2009) 818–827. doi:10.1109/TED.2009.2015802.

[31] D.E.M. Hoff, B.J. Albert, E.P. Saliba, F.J. Scott, E.J. Choi, M. Mardini, A.B. Barnes, Frequency swept microwaves for hyperfine decoupling and time domain dynamic nuclear polarization, Solid State Nucl. Magn. Reson. 72 (2015) 79–89. doi:10.1016/j.ssnmr.2015.10.001.

[32] T. Idehara, E.M. Khutoryan, Y. Tatematsu, Y. Yamaguchi, A.N. Kuleshov, O. Dumbrajs, Y. Matsuki, T. Fujiwara, High-Speed Frequency Modulation of a 460-GHz Gyrotron for Enhancement of 700-MHz DNP-NMR Spectroscopy, J. Infrared, Millimeter, Terahertz Waves. 36 (2015) 819–829. doi:10.1007/s10762-015-0176-2.

[33] D. Yoon, M. Soundararajan, P. Cuanillon, F. Braunmueller, S. Alberti, J.P. Ansermet, Dynamic nuclear polarization by frequency modulation of a tunable gyrotron of 260 GHz, J. Magn. Reson. 262 (2016) 62–67. doi:10.1016/j.jmr.2015.11.008.

[34] S. Alberti, J.P. Ansermet, K.A. Avramides, F. Braunmueller, P. Cuanillon, J. Dubray, D. Fasel, J.P. Hogge, A. MacOr, E. De Rijk, M. Da Silva, M.Q. Tran, T.M. Tran, Q. Vuillemin, Experimental study from linear to chaotic regimes on a terahertz-frequency gyrotron oscillator, Phys. Plasmas. 19 (2012). doi:10.1063/1.4769033.

[35] B.J. Albert, S.H. Pahng, N. Alaniva, E.L. Sesti, P.W. Rand, E.P. Saliba, F.J. Scott, E.J. Choi, A.B. Barnes, Instrumentation for cryogenic magic angle spinning dynamic nuclear

polarization using 90 L of liquid nitrogen per day, J. Magn. Reson. 283 (2017) 71–78. doi:10.1016/j.jmr.2017.08.014.

[36] E.L. Sesti, N. Alaniva, P.W. Rand, E.J. Choi, B.J. Albert, E.P. Saliba, F.J. Scott, A.B. Barnes, Magic Angle Spinning NMR Below 6 K with a Computational Fluid Dynamics Analysis of Fluid Flow and Temperature Gradients, J. Magn. Reson. (2017). doi:10.1016/j.jmr.2017.11.002.

[37] J. Schaefer, R.A. McKay, Multi-Tuned Single Coil Transmission Line Probe for Nuclear Magnetic Resonance Spectrometer, 1999.

[38] S.J. Kim, L. Cegelski, D. Stueber, M. Singh, E. Dietrich, K.S.E. Tanaka, T.R. Parr, A.R. Far, J. Schaefer, Oritavancin Exhibits Dual Mode of Action to Inhibit Cell-Wall Biosynthesis in Staphylococcus aureus, J. Mol. Biol. 377 (2008) 281–293. doi:10.1016/j.jmb.2008.01.031.

[39] M. Rosay, L. Tometich, S. Pawsey, R. Bader, R. Schauwecker, M. Blank, P. Borchard, S.R. Cauffman, K.L. Felch, R.T. Weber, R.J. Temkin, R.G. Griffin, W.E. Maas, Solid-state dynamic nuclear polarization at 263 GHz: spectrometer design and experimental results, Phys. Chem. Chem. Phys. 12 (2010) 5741–5751. doi:10.1039/c003685b.

[40] J.L. Doane, Propagation and Mode Coupling in Corrugated and Smooth-Wall Circular Waveguides, Infrared Millim. Waves, Vol. 13. (1985) 123–170.

[41] S.N. Vlasov, L.I. Zagryadskaya, M.I. Petelin, Transformation of a Whispering Gallery Mode, Propagating in a Circular Waveguide, into a Beam of Waves, Radio Eng. Electron. Phys. 10 (1975) 14–17.

[42] S. V. Kagwade, C.R. Clayton, D. Chidambaram, G.P. Halada, Photochemical breakdown of acetone on copper, Electrochim. Acta. 46 (2001) 2337–2342. doi:10.1016/S0013-

4686(01)00359-0.

[43] B. Piosczyk, A. Arnold, G. Dammertz, M. Kuntze, G. Michel, O.S. Lamba, M.K. Thumm, Step-frequency operation of a coaxial cavity from 134 to 169.5 GHz, IEEE Trans. Plasma Sci. 28 (2000) 918–923. doi:10.1109/27.887753.

[44] A.P. Jagtap, M.-A. Geiger, D. Stöppler, M. Orwick-Rydmark, H. Oschkinat, S.T. Sigurdsson, bcTol: a highly water-soluble biradical for efficient dynamic nuclear polarization of biomolecules, Chem. Commun. 52 (2016) 7020–7023. doi:10.1039/C6CC01813K.

[45] M.-A. Geiger, A.P. Jagtap, M. Kaushik, B. Corzilius, H. Oschkinat, S.T. Sigurdsson, Efficiency of water-soluble nitroxide biradicals for dynamic nuclear polarization in rotating solids at 9.4 T: bcTol-M and cyolyl-TOTAPOL as new polarizing agents, Manuscr. Prep. (2017).

[46] T. Almeida Murphy, T. Pawlik, A. Weidinger, M. Höhne, R. Alcala, J.M. Spaeth, Observation of atomlike nitrogen in nitrogen-implanted solid C60, Phys. Rev. Lett. 77 (1996) 1075–1078. doi:10.1103/PhysRevLett.77.1075.

[47] P. Jakes, K.-P. Dinse, C. Meyer, W. Harneit, A. Weidinger, Purification and optical spectroscopy of N@C60, Phys. Chem. Chem. Phys. 5 (2003) 4080. doi:10.1039/b308284a.

[48] C. Meyer, W. Harneit, B. Naydenov, K. Lips, A. Weidinger, N@C60 and P@C60 as Quantum Bits, Appl. Magn. Reson. 27 (2004) 123–132. doi:10.1007/BF03166307.

[49] M. Eckardt, R. Wieczorek, W. Harneit, Stability of C60 and N@C60 under thermal and optical exposure, Carbon N. Y. 95 (2015) 601–607. doi:10.1016/j.carbon.2015.08.073.

[50] D. Massiot, F. Fayon, M. Capron, I. King, S. Le Calvé, B. Alonso, J.-O. Durand, B.

Bujoli, Z. Gan, G. Hoatson, Modelling one- and two-dimensional Solid State NMR spectra, Magn. Reson. Chem. 40 (2002) 70–76. doi:10.1002/mrc.984.

Chapter 3: A versatile custom cryostat for dynamic nuclear polarization supports multiple cryogenic magic angle spinning transmission line probes

This chapter is adapted from a manuscript of the same title in preparation by Faith J. Scott, Nicholas Alaniva, Natalie C. Golota, Erika L. Sesti, Edward J. Saliba, Lauren E. Price, Brice J. Albert, Pinhui Chen, Robert D. O'Connor and Alexander B. Barnes. This work was done in collaboration with Robert D. O'Connor from the Laboratory of Bioorganic Chemistry at the National Institute of Diabetes and Digestive and Kidney Diseases. The work for the cryostat and waveguide was primarily completed by me. The work on the rigid vacuum jacketed transfer lines was a collaboration between myself and Nicholas Alaniva, and the probe was built by many of the co-authors.

Abstract

Dynamic nuclear polarization (DNP) with cryogenic magic angle spinning (MAS) provides significant improvements in NMR sensitivity, yet presents unique technical challenges. Here I describe a custom cryostat and suite of NMR probes capable of manipulating nuclear spins with multi-resonant radiofrequency circuits, cryogenic spinning below 6 K, sample exchange, and microwave coupling for DNP. The corrugated waveguide and six transfer lines needed for DNP and cryogenic spinning functionality are coupled to the probe from the top of the magnet. Transfer lines are vacuum-jacketed and provide bearing and drive gas, variable temperature fluid, two exhaust pathways, and a sample ejection port. The cryostat thermally isolates the magnet bore, thereby protecting the magnet and increasing cryogen efficiency. This novel design

supports cryogenic MAS-DNP performance over an array of probes without altering DNP functionality. I present three MAS probes (two supporting 3.2 mm rotors and one supporting 9.5 mm rotors) interfacing with the single cryostat. Mechanical details, transmission line radio frequency design, and performance of the cryostat and three probes are described.

3.1. Introduction

Dynamic nuclear polarization (DNP) is a recognized method for enhancing nuclear magnetic resonance (NMR) sensitivity by transferring electron spin polarization [1–4]. Cryogenic temperatures improve DNP efficiency due to increased spin coherence time, and also increase spin polarization according to Boltzmann polarization:

$$P = \tanh\left(\frac{\gamma\hbar B_0}{2k_B T}\right) \quad (1)$$

where γ is the gyromagnetic ratio, $\hbar$ is Planck's constant divided by 2π, B_0 is the static magnetic field, k_B is Boltzmann's constant, and T is the temperature. Therefore, DNP is often performed at or below 100 K [5–9].

However, cryogenic sample temperatures present several logistic issues. Proper insulation is required to improve cryogen efficiency and protect the superconducting magnet. Often, vacuum-insulated transfer lines and a cryostat provide sufficient thermal isolation to thermally protect the O-rings sealing the bore tube within the magnet while also maintaining cryogenic sample temperatures [10].

Here I describe a custom DNP-NMR cryostat and a suite of probes for cryogenic magic angle spinning (MAS) experiments from 100 K to 4.2 K (**Figure 1.5**). The cryostat has seven ports accessed from the top of the magnet: waveguide, sample input/eject, drive gas, bearing gas,

variable temperature (VT) fluid, and two lines for gas exhaust. Multiple probes can be integrated to the same cryostat without fabricating additional transfer lines or waveguides. The versatile cryostat therefore greatly accelerates MAS-DNP instrumentation development.

I describe mechanical and cryogenic engineering details of the cryostat and transfer lines. Designs of the waveguide and radio-frequency (RF) circuits of three transmission line probes are also presented.

3.2. Cryogenic MAS-DNP system

3.2.1 DNP spectrometer design

The MAS-DNP NMR spectrometer show in **Figure 1.5** includes a frequency-agile gyrotron [11], waveguide, fluid transfer lines, heat exchanger [5], and NMR probe. The frequency-agile gyrotron generates microwaves for DNP, and also chirped pulses for electron decoupling [12]. Microwaves exit the gyrotron though a sapphire window and propagate through corrugated overmoded waveguide to the DNP cryostat. Transfer lines for drive and bearing gas, exhaust gas, and variable temperature fluid also mate into the top of the DNP cryostat. A cryogenic sample eject apparatus allows the exchange of samples while the probe remains in place at cryogenic temperatures [10]. A single 260 L N_2 (l) dewar supplies enough liquid nitrogen to the heat exchanger for 60 hours of continual MAS at 90 Kelvin [5]. Alternatively, 100 L of He (l) cools spinning samples to <6 K for 3 hours [13].

Probes can be exchanged within the DNP cryostat, which is mounted to the room-temperature shim stack of a 7 T magnet. Equipping the cryostat with cryogenic DNP functionality including vacuum jacketed transfer lines, waveguide, and sample exchange, reduces the experimental requirement for each probe. Probes only require RF circuitry, a stator, and optics for spinning and temperature detection. This has allowed us to fabricate three transmission line probes for a

fraction of the resources typically required for cryogenic MAS DNP instrumentation. A Tecmag console generates RF pulses for control of ^{1}H, ^{31}P, ^{13}C, and ^{15}N nuclear spins, and also voltage profiles for chirped microwaves pulses and electron spin control (Tecmag, Inc, Houston, TX).

3.2.2 Cryostat

The cryostat protects the magnet and helps establish cryogenic sample temperatures (**Figure 3.1**) [14]. Introducing cryogens into the warm bore of a superconducting magnet can result in a quench if the O-rings sealing the magnet bore tube freeze.

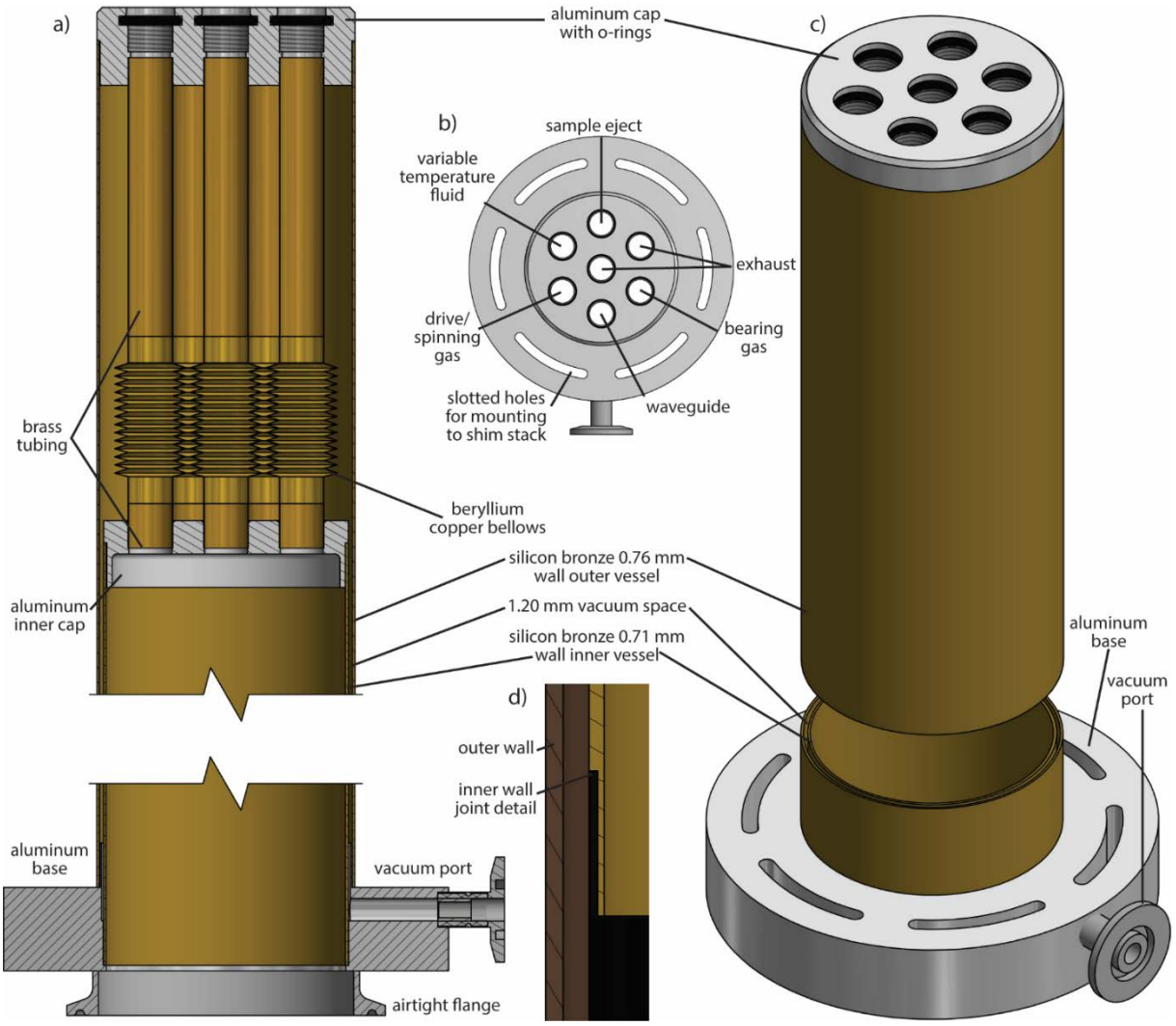

Figure 3.1 a) CAD section view of cryostat. b) Top view CAD of cryostat indicating the location of transfer lines for the probe containing the 3.2 mm rotor. c) Isometric CAD of cryostat. d) Wall detail to show interlocking cryostat wall joints. All seals were made with cryogenic-grade epoxy.

A vacuum insulated bronze cryostat provides the necessary protective thermal insulation between the sample chamber and magnet bore, while conserving valuable space. The cryostat is 0.90 m long and extends 0.86 m into the magnet bore. Inner and outer cryostat vessel walls are 0.71 and 0.76 mm thick bronze, respectively. The vessels are aligned concentrically with a 1.20 mm gap evacuated to $<5 \times 10^{-6}$ Torr (**Figure 3.1c**). The vessels were machined from 3" round bar C65500 silicon bronze. Silicon bronze results in a homogenous magnetic field for high-resolution NMR, and can also be machined to thin walls to maximize interior volume [14]. Due to machining restrictions, the inner vessel is constructed in three sections and the outer vessel in four sections, with sections cut to overlap as shown in Figure 2d to align the joined sections along the central axis. Beryllium copper bellows (Mini-Flex Corporation, Ventura, CA) are included into each port to accommodate thermal contraction of the inner vessel. The vessels and aluminum cap and base were fabricated in the Washington University in Saint Louis (WUSTL) chemistry department machine shop and sent to Precision Cryogenics, Inc. (Indianapolis, IN) for assembly with cryogenic epoxy.

The cryostat has an internal diameter of 68.3 mm to accommodate probes, and the aluminum base is attached to the shim-stack under the magnet. A tri-clover type flange mates to a collar on the NMR probe stack to provide a tight seal. Seven smaller threaded ports in the top aluminum cap allow gases (bearing, drive, VT, exhaust), microwaves, and NMR samples to enter and exit the NMR probe (**Figure 3.1b**). The ports are equally sized so that transfer lines can be rearranged into any probe configuration. To seal the inner space of the cryostat O-rings, (0.4375" inner diameter, Buna-N, McMaster-Carr, Elmhurst, IL) surround each line and are compressed with a brass plate mirroring the port pattern of the cryostat (**Figure 3.2**). Rods are threaded into a

brass anchor plate fixed to the top of the magnet to compress the O-rings. This anchor plate has channels that allow room temperature air to circulate at the top of the magnet.

3.2.3 Transfer lines

The seven ports on the top of the cryostat are identical to allow rearrangement of the transfer lines and waveguide and adaptation to different probe configurations. Vacuum-jacketed transfer lines provide excellent thermal isolation for cryogen delivery to the sample space. The rigid transfer lines mate into the cryostat and are connected to flexible vacuum-jacketed lines via bayonet connections (Precision Cryogenics, Inc.). The flexible lines purchased from Precision Cryogenics, Inc. supply gases to and from the heat exchanger. (**Figure 3.3**).

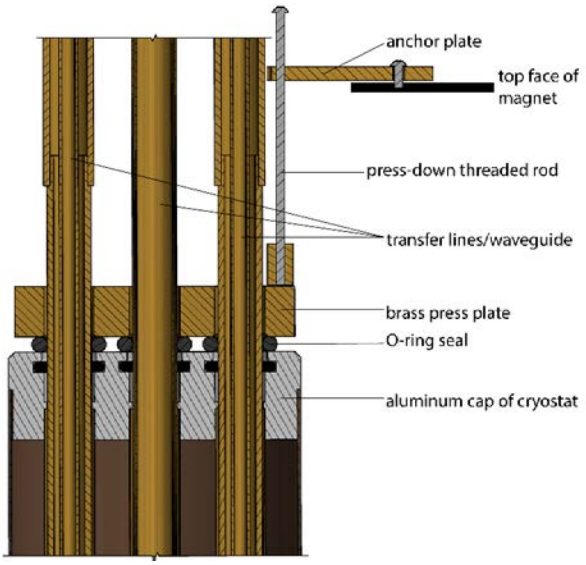

Figure 3.2 Section view detailing the top of the cryostat with brass press plate and transfer lines installed.

The bearing and drive gas, VT fluid, and exhaust ports each have their own transfer line, which allows for fine temperature and flow control of different cryogenic channels. The VT line can also transfer liquid helium, while drive and bearing lines transfer helium or nitrogen gas [13]. Two exhaust lines are used: one to carry cryogens through counterflow coils in the heat exchanger to act as a refrigerant, and the other to reduce backpressure during liquid helium experiments, thus improving spinning stability.

The rigid transfer lines are constructed from brass tubing. The vacuum chamber is sealed at the bottom with a brass plug and extends through the bayonet connector to provide insulation at the rigid and flexible transfer line interface.

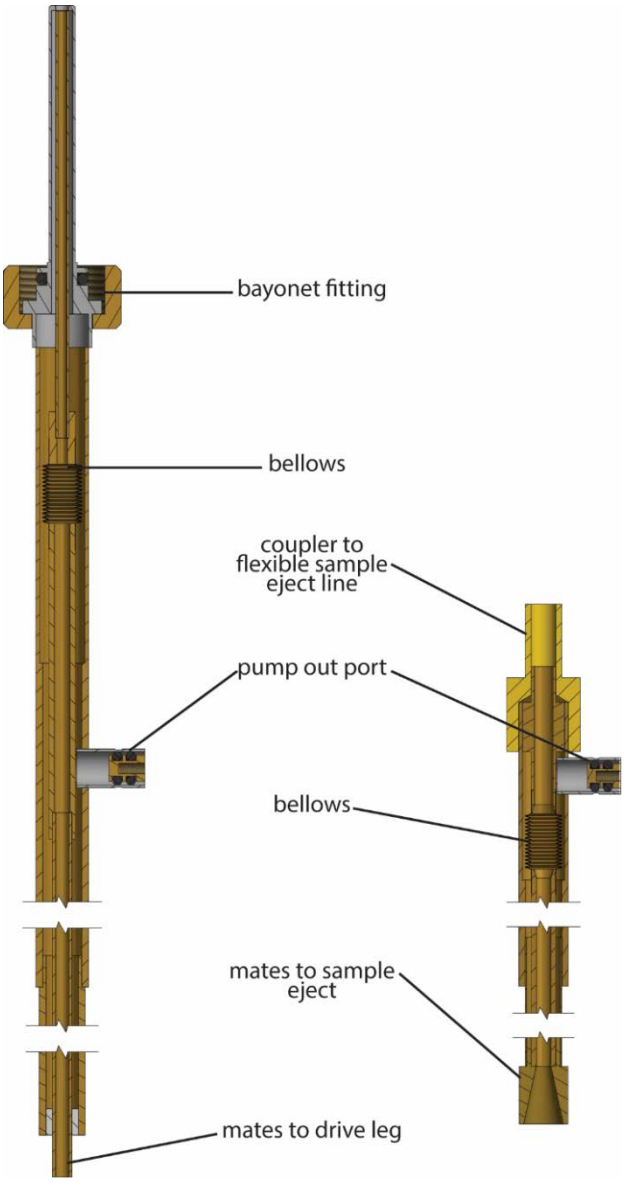

Figure 3.3 CAD section view of drive gas line (left) and sample eject line (right). The vacuum space between the inner and outer brass tubes is kept in the order of 10^{-4} Torr. The drive gas line delivers cryogenic gas to spin the rotor; the sample-eject inner path is modified to allow for rotor transfer in and out of the probe space.

A port soldered to the outer jacket with an actuator sealed by two O-rings is used to access the vacuum space, which is evacuated to $<10^{-4}$ Torr through a flexible thin-walled hose connected to a vacuum manifold. Multiple ports on the vacuum manifold allow all transfer lines to be continually connected, pressure monitored, and evacuated as needed, to reduce downtime of the instrument.

Beryllium copper bellows are soldered to the inner brass tube of the rigid transfer lines to accommodate thermal contraction of the inner transfer tube. While the cryogenic transfer lines are similar in geometry, the sample eject line must be able to transfer rotors to and from the stator. The top of the vacuum space terminates in a brass ejection fitting (**Figure 3.3**), allowing smooth exchange of sample rotors [10]. To eject samples, the probehead is pressurized with either nitrogen or helium gas via the exhaust line. The sample is carried out of the probe by the pressurized gas through a PTFE tube to slow the rotor and bring it to rest in a collection chamber [10].

Each rigid transfer line has an 0.50” outer tube soldered to a 0.4375” OD brass tube via a telescoping joint. This outer tube continues down to the probehead, where it fits into a polyethylene probehead cap and onto a Gore-Tex surface that duplicates the cryostat port pattern. The cap and Gore-Tex help to seal the probehead during operation.

3.2.4 Corrugated waveguide for microwave transmission

Microwaves are coupled from the gyrotron to the sample using a system of overmoded corrugated waveguide, mirrors, and tapers (**Figures 1.5,3.4**) [15–17]. The waveguide has three main sections: the first has a 25.4 mm OD and a 19.0 mm ID and extends from the gyrotron to the top of the magnet; the second section reduces the OD to 12.7 mm and the ID to 9.5 mm (**Figure 3.4c**); and the third section continues at the smaller OD and ID until ending at the probe.

Mirror reflections through the larger inner diameter sections allow for lower loss [16]. The waveguide ID decreases in the last section to pass into the port at the top of the cryostat.

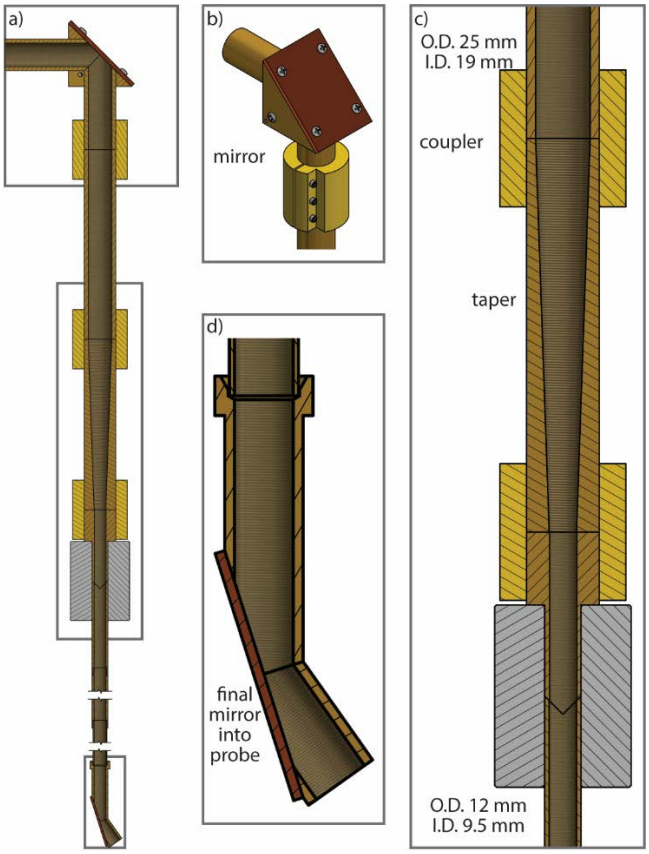

Figure 3.4 a) CAD section view of waveguide including the last two mirrors before the sample space. b) CAD isometric view of 90° mirror bend. c) CAD section view of taper from 19 mm to 9.5 mm ID. d) Final mirror as the waveguide enters the stator for the 3.2 mm rotor. The bottom portion is installed in each probe and is interchangeable. The top portion seats into the tapered coupling.

All sections are made of 360 brass and are corrugated on the inner surface with a custom tap (Midwest Precision Tool and Die, Inc., Sioux Falls, SD) with 56 threads per inch and a cut depth of 0.3 mm (**Figure 3.5**) [15]. The waveguide pieces are drilled straight at a tolerance of ±0.076 mm to allow the tap to run continuously though the 19” sections of brass tube (Grover Gundrilling, Norway, ME). The outside of each piece is turned down after drilling the center hole to ensure concentricity of the hole and outside surface for good alignment. The taper piece

could not be tapped, so grooves were milled into the interior surface at a depth of 0.3 mm and spacing of 22 grooves per cm.

The corrugated waveguide is cut at each mirror bend to maintain ID continuity to the mirror surface. Each mirror is a polished copper plate secured by a brass block (**Figure 3.4b**). Miter bend mirrors are set at a 45° angle of incidence to maximize reflection until the final mirror [16]. In the 3.2 mm probehead, the final mirror is set at an incident angle of 73° to couple into the stator perpendicular to the rotor. In the 9.5 mm probehead, the final mirror angle of incidence is 63° to couple along the rotor's spinning axis. The waveguide loss is 0.4 dB over the first meter and 4.4 dB over the entire waveguide (6 m); 36 W of power from the gyrotron window results in 13 W of microwave power at the sample (**Figure 3.6**). The gyrotron is frequency agile to control electron spins within the sample beyond continuous wave irradiation [11,12].

Figure 3.5 a) Taps welded to rods to drive through 19" lengths of waveguide. b) Detail of tap head. c) Illustration of finished tap width and depth with 56 threads per inch.

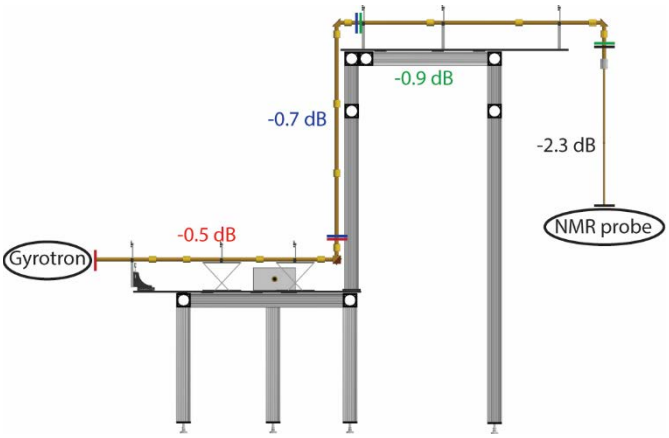

Figure 3.6 CAD view of the waveguide with microwave power losses in dB for each section.

3.3 Transmission line circuits for cryogenic MAS-NMR

Fluid transfer lines and the microwave waveguide descend from the top of the cryostat to the center of the magnet bore, where they couple to the probehead. This probehead contains the stator body, which in turn contains the sample coil. The sample coil is electrically connected to the inner and outer conductors of a transmission line in the form of the Schaefer-McKay transmission line probe [18,19]. A main advantage of this design is the remote location of the tuning and matching capacitors, which allows for easy, room temperature access while the sample is maintained at cryogenic temperatures [20]. Impedance matched to 50 ohms is necessary for efficient power delivery to the sample and subsequent signal detection.

Proton decoupling and multi-resonance manipulation are essential for most modern NMR experiments. Here I describe two probes designed for ^{1}H and ^{13}C experiments (3.2 and 9.5 mm) and a third 3.2 mm probe for ^{1}H, ^{13}C, ^{31}P, and ^{15}N experiments.

The coincident manipulation and detection of different nuclear spins requires electrical isolation between channels. **Figure 3.7** shows the combined circuit schematic. The elements that comprise both two-channel probes are shown in black and the additional components for the four-channel

probe are shown in blue. **Table 3.1** lists the capacitor values of all probes, and **Tables 3.2-3.4** report the isolation values between the various probe channels.

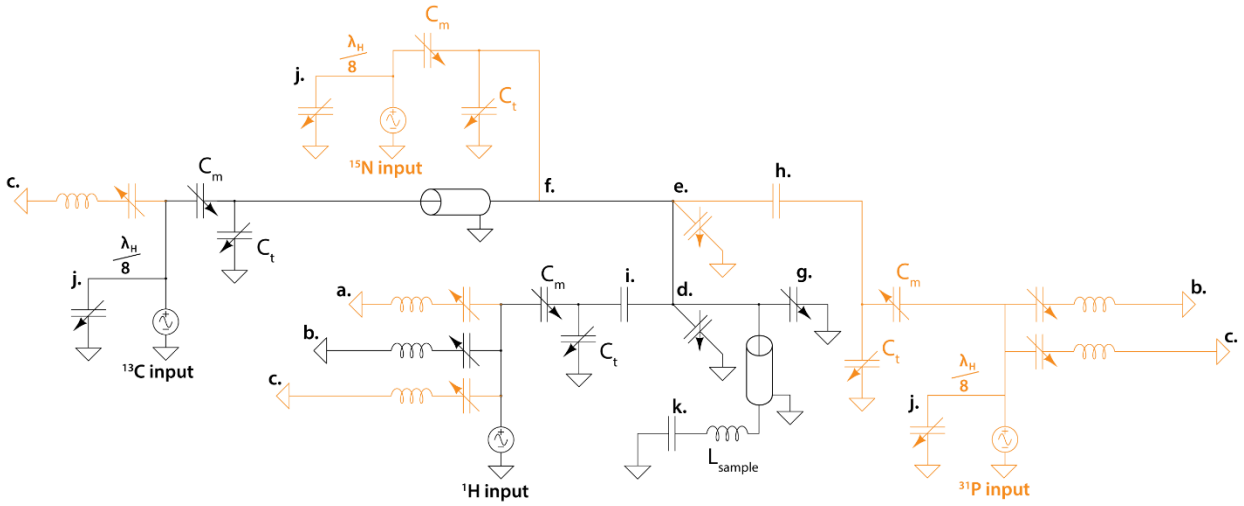

Figure 3.7 Circuit schematic of the radio frequency (RF) probes. Shown in black are the components that make up a two-channel ^{1}H, ^{13}C probe. The components shown in blue are those that must be added for a four-channel ^{1}H, ^{31}P, ^{13}C, ^{15}N probe. a.) ^{31}P RF trap. b.) ^{13}C RF trap. c.) ^{15}N RF trap. d.) ^{1}H current node with phosphorus node adjust capacitor. e.) ^{31}P current node with ^{13}C node adjust capacitor. f.) ^{13}C current node. g.) ^{1}H current node adjust capacitor. h.) In-line capacitor. i.) Teflon disk capacitor j.) One-eighth ^{1}H wavelength and variable capacitor for ^{1}H trap k.) ATC chip capacitor. Transmission line probes described here are modeled after the probes described in [19].

Table 3.1 Capacitor value summary for all probes.

Capacitor	3.2 mm rotor 4-channel probe	3.2 mm rotor 2-channel probe	9.5 mm rotor 2-channel probe	Description
a.	1-14 pF	--	--	*Variable capacitor in ^{31}P trap*
b.	1-14 pF	1-14 pF	1-14 pF	*Variable capacitor in ^{13}C trap*
c.	1-14 pF	--	--	*Variable capacitor in ^{15}N trap*
d.	5-10 pF	--	--	*Teflon cap + air gap at ^{1}H node*
e.	5-10 pF	--	--	*Teflon cap + air gap at ^{31}P node*
g.	0.3-3.3 pF	0.8-8.8 pF	0.8-8.8 pF	*Proton node adjust, end cap*
h.	25 pF	--	--	*^{31}P in-line capacitor*
i.	10 pF	10 pF	10 pF	*Teflon disk capacitor*
j.	1-14 pF	1-14 pF	1-14 pF	*Variable capacitor for ^{1}H trap*
k.	220 pF	220 pF	110 pF	*Chip capacitor*
C_m	3-30 pF	3-30 pF	3-30 pF	*Matching capacitor*
C_t	3-30 pF	3-30 pF	3-30 pF	*Tuning capacitor*

3.3.1 Fabrication and engineering detail

Three probes were built at WUSTL with a combination of commercially available and custom-machined parts. Transmission lines consist of an inner conductor centered within the outer conductor using Teflon spacers. The inner conductor is made of type K ¾" copper pipe cut to length and fitted with copper shims, and the outer conductor is constructed of type M 2½" copper pipe. All outer conductor couplings are cut in half for easy access to the center conductor and secured with 316 stainless steel hose clamps.

Isolation of the highest frequency ^{1}H channel is primarily achieved with a current node. A length equivalent to ¾ of the 300 MHz ^{1}H wavelength is connected between ground and the ^{1}H current node to provide isolation from the ^{1}H channel to the lower frequency channels (**Figure 3.7d**). A copper cap on the elbow connecting the vertical transmission is capacitively coupled to the grounded outer conductor through a variable plate to allow fine adjustment of the ^{1}H node. (**Figure 3.7g**). Lower frequency channels are isolated from higher frequency channels using in-line capacitors such as those shown in **Figure 3.7h** and **i**. For improved isolation, LC traps are added into the rectangular boxes housing the tuning and matching capacitors (**Figure 3.8**) (Jennings, Memphis, TN). These LC traps contain an adjustable capacitor to fine-tune the isolation. A chip capacitor in the probehead matches the sample coil to 50 ohms inductance for maximum RF transmission (American Technical Ceramics Corp, Huntington Station, NY).

Due to the cryogenic temperatures present at the probehead in DNP-NMR experiments, a 0.33 m section of the inner and outer conductors in the vertical stack leading to the NMR coil is composed of 316 stainless steel as a thermal break, followed by 0.1 m of copper to prevent magnetic field distortion near the NMR sample. The inner surface of the stainless steel outer conductor and the outer surface of the stainless steel inner conductor are coated; first in gold to activate the surface, then 1.27 μm of silver for electrical conduction, followed by another gold

coating to prevent oxidation of the silver. The silver coating on stainless steel allows electrical conduction through the probe stack while preserving thermal insulation.

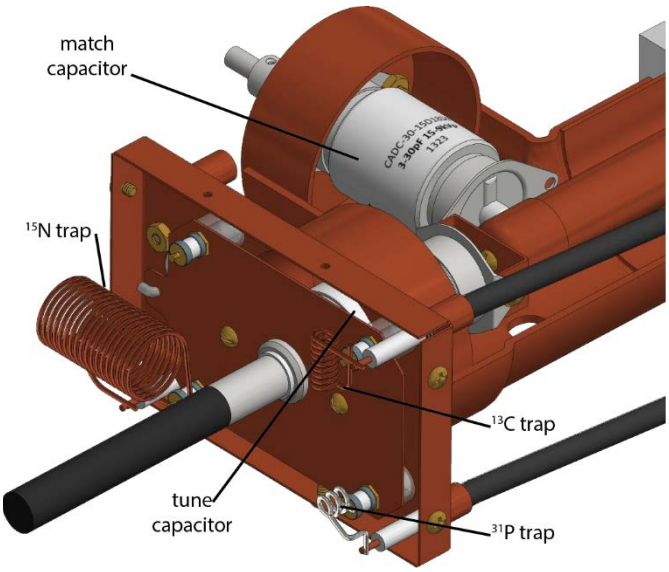

Figure 3.8 CAD detail view of the tune and match box showing tune and match capacitors and three LC traps terminating in ¼ wavelength cables to ground.

Probehead for 3.2 mm rotor

Probeheads for the 3.2 mm and 9.5 mm rotor probes have the same circuitry but differ in fluid delivery configurations and microwave coupling schemes.

The stator for the 3.2 mm probehead was custom machined from Kel-F in the Washington University in St. Louis machine shop with the addition of ceramic bearings and a brass drive cup (Revolution NMR, Fort Collins, CO). A Kel-F coil block attached to the bottom of the stator secures the coil leads and fiber optic cables for spinning detection.

The NMR coil (100 nH, 5 turns, 5.7 mm long, 18 gauge copper wire) is mounted to the inner conductor with a set screw and an ATC capacitor that is grounded to the outer conductor (**Table 3.1**). Teflon in the probehead electrically isolates the inner and outer conductors. The back leg (**Figure 3.9a**, green) for bearing gas is machined from Kel-F. The yellow leg in the foreground

contains channels that deliver drive gas and VT fluid to the stator and was 3D printed from ABS-like plastic by 3D Systems (Rock Hill, SC). A sample eject piece over the stator opening allows for cryogenic sample exchange within minutes (3D Systems) [10]. Connections from the transfer lines to the probehead can top and the stator legs are airtight. The waveguide irradiates the sample rotor perpendicular to its spinning axis at an electron Rabi frequency of 0.38 MHz with 5 W of microwave irradiation [21]. The maximum spinning frequency of this probe is 20 kHz ± 5 Hz, and the coil inductance is 100 nH.

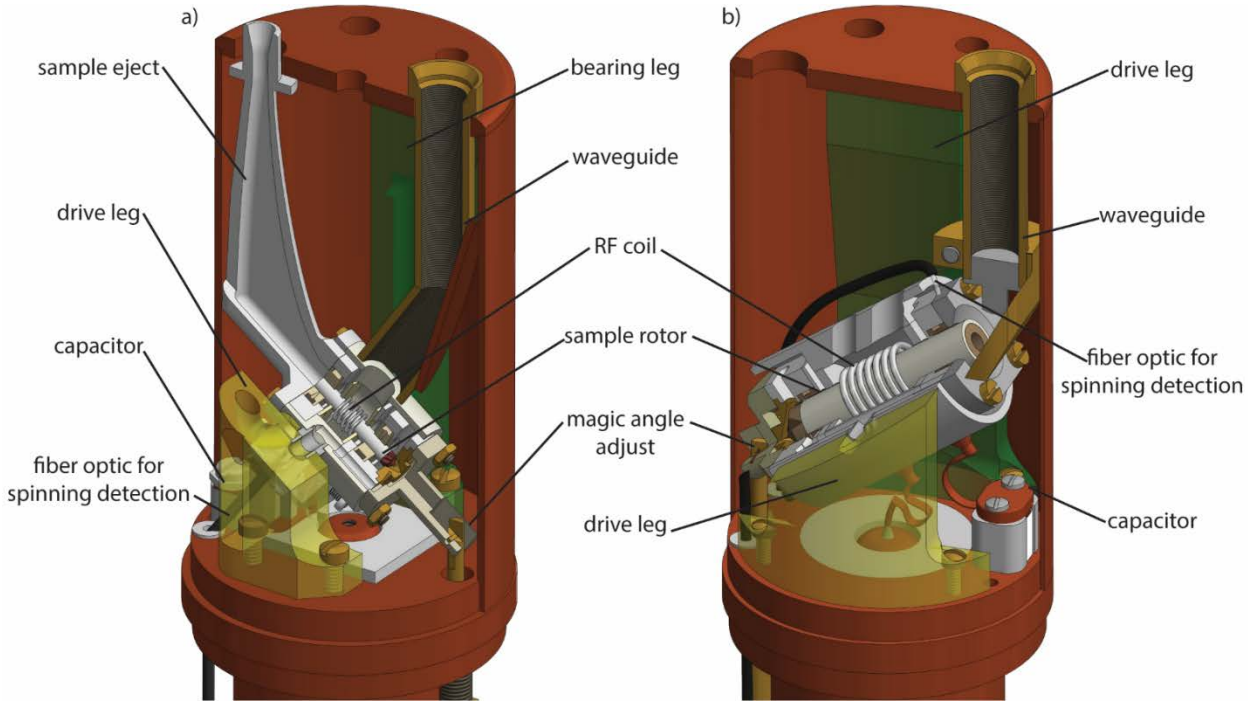

Figure 3.9 CAD detail view of probehead for a) 3.2 mm OD rotor and b) 9.5 mm OD rotor.

Probehead for 9.5 mm rotor

The stator for the 9.5 mm rotor (**Figure 3.9b**) is larger and sits within the same volume probehead as the 3.2 mm rotor stator, leaving no room for a sample eject. Stator bearings, drive cup, and rotor were purchased from Revolution NMR, and 3D Systems 3D printed the drive and bearing legs using ABS-like plastic. The coil leads are a flat copper ribbon; one side of the ribbon is soldered to the inner conductor and the other lead is clamped in line with a 110 pF chip

capacitor to ground. The coil inductance is 630 nH (7 turns, 14.3 mm, 18 gauge copper wire). Stator orientation is reversed such that the drive and bearing lines are transposed and the exhaust line goes through the port previously used for the sample eject line. A lens is added before the final waveguide mirror to focus the Gaussian beam, with the waveguide directing the microwaves along the rotor's spinning axis. The electron Rabi frequency using this on-axis microwave coupling method was 0.34 MHz with a 5 W input using Ansys High Frequency Structure Simulator (HFSS, Canonsburg, PA).

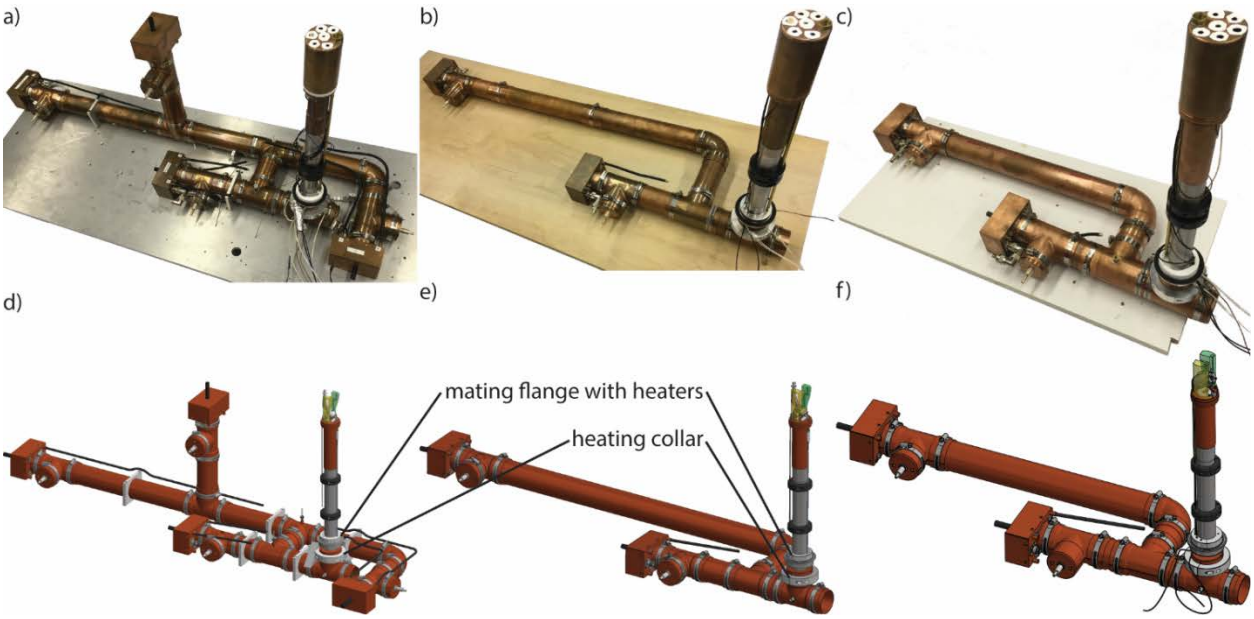

Figure 3.10 Photographs of a) 4-channel probe with 3.2 mm OD rotor, b) 2-channel probe with 3.2 mm OD rotor, and c) 2-channel probe with 9.5 mm OD rotor. CAD views of d) 4-channel probe with 3.2 mm OD rotor, e) 2-channel probe with 3.2 mm OD rotor, and f) 2-channel probe with 9.5 mm OD rotor with can top removed.

3.3.2 Four-channel probe with 3.2 mm MAS

The four-channel NMR probe with 3.2 mm OD MAS rotor (**Figure 3.10a,d**) has been used in a variety of experiments [5,11–13,22]. The combination of ^{1}H, ^{31}P, ^{13}C, and ^{15}N channels allows investigation of biological systems, with ^{13}C and ^{15}N isotopes found in proteins and used for a variety of labeled and unlabeled 2D-NMR experiments. ^{31}P is also a useful biological isotope

found in phospholipid head groups in cellular membranes, while the ^{1}H channel, which can be used for detection or 2D experiments, is most often used for cross-polarization and subsequent decoupling. Isolation values for this probe are shown in **Table 3.2**.

Table 3.2 Isolation values and nutation frequencies of four-channel probe with 3.2 mm OD rotor. Power value used for nutation frequency is given in the last row.

Transmitting→ Receiving↓	^{1}H	^{31}P	^{13}C	^{15}N
^{1}H	--	-60 dB	-60 dB	-60 dB
^{31}P	-54 dB	--	-67 dB	-43 dB
^{13}C	-52 dB	-37 dB	--	-34 dB
^{15}N	-58 dB	-50 dB	-38 dB	--
Nutation Frequency	222 kHz	125 kHz	154 kHz	181 kHz
Power from amplifier	800 W	900 W	820 W	910 W

3.3.3 Two-channel probe with 3.2 mm MAS

The two-channel version of the 3.2 mm OD rotor probe (**Figure 3.10b,e**) is capable of a variety of DNP-NMR experiments on biological samples and materials. ^{13}C capability is useful for fully or partially isotopically labelled proteins. The ^{1}H channel is used for cross polarization and proton decoupling for increased resolution. This probe can be interchanged quickly for the four-channel probe to further customize either probe. ^{13}C nutation frequency (**Table 3.3**) is slightly higher for the two-channel probe, but the ^{1}H nutation frequency is nearly halved, indicating that less power is available for decoupling.

Table 3.3 Isolation values and nutation frequencies of two-channel probe with 3.2 mm OD rotor. Power value used for nutation frequency is given in the last row.

Transmitting → Receiving↓	^{1}H	^{13}C
^{1}H	--	-54 dB
^{13}C	-36 dB	--
Nutation frequency	125 kHz	167 kHz
Power from amplifier	800 W	820 W

3.3.4 Two-channel probe with 9.5 mm MAS

The two-channel probe built for 9.5 mm OD MAS rotors (**Figure 3.10c,f**) is capable of the carbon–proton experiments described above but with a 600 μL sample size, 17-times that of the 3.2 mm rotor. The ^{13}C nutation frequency in the 9.5 mm rotor probe is 71 kHz at 600 W input power (**Table 3.4**). At 820 W, the ^{13}C nutation frequency is 97 kHz, i.e., 1.72-times lower than the 167 kHz nutation frequency of the 3.2 mm two-channel probe but providing an overall gain of ~10-times NMR sensitivity for these much larger samples. This sensitivity gain can be exploited for inexpensive samples with low levels of isotopic labeling such as in naturally abundant whole cells. Alternatively, the large rotor can be used for a secondary Teflon microwave lens leading into a smaller sample volume. This strategy is particularly advantageous for pulsed DNP research because of the drastically increased electron Rabi frequency and homogeneity in small samples (as small as 3 μL in preliminary calculations). Overall, the large rotor contained in the 9.5 mm MAS probe allows the flexibility to use large sample sizes for samples dilute in isotopic labels and increased electron Rabi frequency for pulsed DNP.

Table 3.4 Isolation values and nutation frequencies of two-channel probe with 9.5 mm OD rotor. Power value used for nutation frequency is given in the last row.

Transmitting → Receiving↓	^{1}H	^{13}C
^{1}H	--	-68 dB
^{13}C	-46 dB	--
Nutation frequency	40 kHz	71 kHz
Power from amplifier	800 W	600 W

3.4. Mechanical and cryogenic engineering

3.4.1 Heaters on probe stack

Two sets of heating collars are integrated into the designs of each of the three probes introduced above. The cryostat-mating collar contains two cartridge heaters inserted into the body of the collar from the underside (OMEGA Engineering, Inc, Norwalk, CT). This collar is clamped around the 316 stainless-steel vertical stack of the probe and compresses an O-ring to seal the cryostat-probe connection below the magnet (**Figure 3.1, 3.10**). There is an additional heating collar mounted around the vertical portion of the copper outer conductor at the final T, which mates to the vertical stack. The heating elements maintain ambient temperature of the outer conductor of the transmission lines located below the magnet bore. This heating collar is crucial for preventing ice formation within the transmission lines and probe de-tuning. To further combat ice formation, high-flow air is pumped around the cryostat-vertical stack interface using air displacement units. A high flow of room temperature nitrogen gas is also injected into the space between inner and outer conductors at the center of the final probe T.

3.4.2 MAS adjustment

The ability to adjust the angle of the sample spinning axis relative to the main magnetic field is a necessity in solid-state NMR. This is achieved using a threaded rod to push and pull one end of the sample housing as it pivots about its bearing and drive gas import channels. This simple solution requires modification for experiments at cryogenic temperatures.

When spinning with gases at 80 K and cooling with fluids down to 4.2 K, the stator shrinks, which can alter the stator angle set at room temperature. It is crucial that the probe design allows for magic angle adjustment at these temperatures. The main body of the magic angle adjustment rod is a 0.5” OD brass rod with threading at the end to mate with threading in the probehead base. A freely rotatable brass end piece attaches to an extension of the stator body. The rod adjust then extends downward to protrude below the under-side of the probe stack heater/cryostat

coupler. A Gore-Tex plug is fixed to the rod above the interface between the rod adjust and the top side of this stack heater. The plug prevents any potential cryogen leak through the small clearance between the rod adjust and the through hole in the stack heater while maintaining free rotation of the rod adjust. This design allows for magic angle adjustment at cryogenic temperatures and ensures integrity of the magic angle during DNP-MAS.

3.4.3 Temperature measurements of MAS at 4.2-6 K (with and without microwaves)

Attaining sub-6 K temperatures requires application of liquid helium to the center of the sample as it spins in the stator. To accurately determine the temperature, a Cernox temperature sensor is inserted at the interface between the stator body and the VT outlet. Lake Shore Cryotronics, Inc. calibrated the temperature sensor to a temperature of 1.2 K within a magnetic field of 7 T, matching laboratory conditions. This temperature sensor reports temperatures of 4.2 – 5.0 K without microwave irradiation and 5.3 – 6.0 K with microwave irradiation. This experimental data, together with fluid dynamics simulations [13], shows that these MAS-DNP experiments with liquid helium VT fluid are conducted at sample temperatures between 4.2 and 6 K.

3.4.4 Quality factor at 298 K and 6 K

In NMR, the quality factor Q indicates the power loss within the sample coil at a given frequency. $Q = \omega L/R$, where R is the effective resistance of the inductor coil, ω is the operating frequency, and L is the effective inductance of the coil [23]. A higher Q factor indicates that more RF power is delivered to the sample. **Figure 3.11** shows a comparison of resonant tuning dip plots obtained using a Vector Network Analyzer (SDR-Kits, Melskam, Wilts, UK) at 300.179 MHz of the 3.2 mm, four-channel transmission line probe at room temperature (298 K), 90 K, and 6 K. Q at 296 K=390, Q at 90 K=790, and Q at 6 K=880. As the sample temperature de-creases, the Q factor of the inductor at 300.179 MHz increases. This increase in Q factor at

the proton frequency allows for decoupling at lower power from the high-power amplifier, or, in turn, for high ^{1}H decoupling (Tomco, Stepney, South Australia).

3.5 Conclusions and Outlook

The adaptable nature of this cryostat-transfer line system allows for novel MAS-DNP NMR probes to be constructed and implemented at a reduced cost. The vacuum-jacketed cryostat protects the NMR magnet during cryogenic experiments, and vacuum-jacketed transfer lines and a sample eject line decrease down-time in MAS-DNP experiments conducted below 6 K. This system allows for the manufacture, modification, and testing of stator design, microwave delivery, and probe circuitry with relative ease.

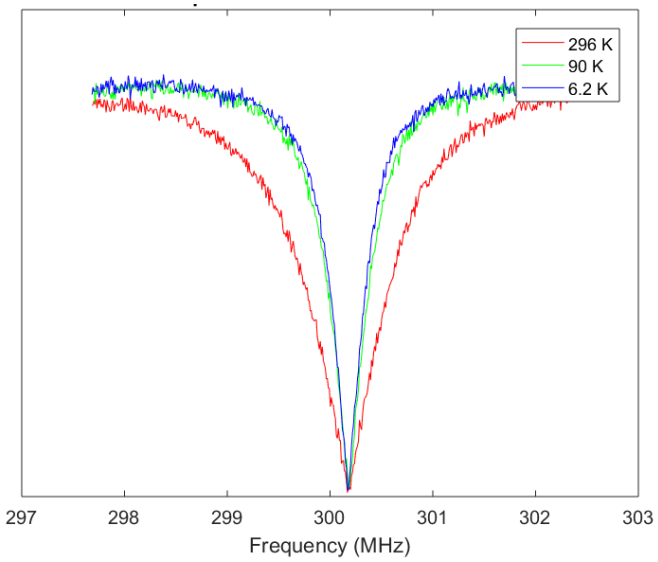

Figure 3.11 Magnitude plots of the impedances of the proton circuit of the 3.2 mm, four-channel probe at sample temperatures of 296 K (red), 90 K (blue), and 6.2 K (green). The impedances are matched to 50 ohms at 300.179 MHz, and the quality factor of this circuit increases with decreasing temperatures. These plots were generated with a Vector Network Analyzer. Q at 296 K= 390, Q at 90 K=790, and Q at 6 K = 880.

The customizable nature of the presented NMR probes allows for future development. One proposed addition to the two-channel 3.2 mm probe is a ^{19}F channel (282.231 MHz). A $\lambda_F/4$ open-circuit transmission line (JS trap) can be implemented to isolate ^{19}F frequency from going into the ^{1}H channel [24]. ^{19}F is a desirable isotope for NMR due to its stability, high natural

abundance, and high NMR sensitivity. It is suitable for physiological and pharmacological studies in vivo by virtue of its bioorthogonal nature. ^{19}F has previously been integrated into a biological sample for REDOR distance measurements [25]. The 4-channel 3.2 mm rotor probe is also compatible with a ^{2}H channel for additional REDOR and ^{2}H-^{13}C and ^{2}H-^{15}N correlation experiments [26]. Flexibility in available probes also allows for future instrumentation development such as sample rotors of different geometries able to spin at frequencies >20 kHz. The DNP cryostat described in this chapter facilitates innovation in future MAS-DNP probes and other instrumentation.

References

[1] A.S. Lilly Thankamony, J.J. Wittmann, M. Kaushik, B. Corzilius, Dynamic nuclear polarization for sensitivity enhancement in modern solid-state NMR, Prog. Nucl. Magn. Reson. Spectrosc. 102–103 (2017) 120–195. doi:10.1016/j.pnmrs.2017.06.002.

[2] M. Renault, S. Pawsey, M.P. Bos, E.J. Koers, D. Nand, R. Tommassen-Van Boxtel, M. Rosay, J. Tommassen, W.E. Maas, M. Baldus, Solid-state NMR spectroscopy on cellular preparations enhanced by dynamic nuclear polarization, Angew. Chemie - Int. Ed. 51 (2012) 2998–3001. doi:10.1002/anie.201105984.

[3] L.R. Becerra, G.J. Gerfen, R.J. Temkin, D. Singel, R.G. Griffin, Dynamic nuclear polarization with a cyclotron resonance maser at 5 T, Phys. Rev. Lett. 71 (1993) 3561–3564. doi:10.1103/PhysRevLett.71.3561.

[4] A. Lesage, M. Lelli, D. Gajan, M.A. Caporini, V. Vitzthum, P. Miéville, J. Alauzun, A. Roussey, C. Thieuleux, A. Mehdi, G. Bodenhausen, C. Copéret, L. Emsley, Surface enhanced NMR spectroscopy by dynamic nuclear polarization., J. Am. Chem. Soc. 132

(2010) 15459–61. doi:10.1021/ja104771z.

[5] B.J. Albert, S.H. Pahng, N. Alaniva, E.L. Sesti, P.W. Rand, E.P. Saliba, F.J. Scott, E.J. Choi, A.B. Barnes, Instrumentation for cryogenic magic angle spinning dynamic nuclear polarization using 90 L of liquid nitrogen per day, J. Magn. Reson. 283 (2017) 71–78. doi:10.1016/j.jmr.2017.08.014.

[6] K.R. Thurber, R. Tycko, Low-temperature dynamic nuclear polarization with helium-cooled samples and nitrogen-driven magic-angle spinning, J. Magn. Reson. 264 (2016) 99–106. doi:10.1016/j.jmr.2016.01.011.

[7] C. von Morze, J. Tropp, A.P. Chen, I. Marco-Rius, M. Van Criekinge, T.W. Skloss, D. Mammoli, J. Kurhanewicz, D.B. Vigneron, M.A. Ohliger, M.E. Merritt, Sensitivity enhancement for detection of hyperpolarized 13C MRI probes with 1H spin coupling introduced by enzymatic transformation in vivo, Magn. Reson. Med. 41 (2017) 36–41. doi:10.1002/mrm.27000.

[8] D. Lee, E. Bouleau, P. Saint-Bonnet, S. Hediger, G. De Paëpe, Ultra-low temperature MAS-DNP, J. Magn. Reson. 264 (2016) 116–124. doi:10.1016/j.jmr.2015.12.010.

[9] J.H. Ardenkjaer-Larsen, B. Fridlund, A. Gram, G. Hansson, L. Hansson, M.H. Lerche, R. Servin, M. Thaning, K. Golman, Increase in signal-to-noise ratio of 10,000 times in liquid-state NMR, Proc. Natl. Acad. Sci. 100 (2003) 10158–10163. doi:10.1073/pnas.1733835100.

[10] A.B. Barnes, M.L. Mak-Jurkauskas, Y. Matsuki, V.S. Bajaj, P.C. a van der Wel, R. DeRocher, J.A. Bryant, J.R. Sirigiri, R.J. Temkin, J. Lugtenburg, J. Herzfeld, R.G. Griffin, Cryogenic sample exchange NMR probe for magic angle spinning dynamic nuclear

polarization, J. Magn. Reson. 198 (2009) 261–270. doi:10.1016/j.jmr.2009.03.003.

[11] F.J. Scott, E.P. Saliba, B.J. Albert, N. Alaniva, E.L. Sesti, C. Gao, N.C. Golota, E.J. Choi, A.P. Jagtap, J.J. Wittmann, M. Eckardt, W. Harneit, B. Corzilius, S. Th. Sigurdsson, A.B. Barnes, Frequency-agile gyrotron for electron decoupling and pulsed dynamic nuclear polarization, J. Magn. Reson. 289 (2018) 45–54. doi:10.1016/j.jmr.2018.02.010.

[12] E.P. Saliba, E.L. Sesti, F.J. Scott, B.J. Albert, E.J. Choi, N. Alaniva, A.B. Barnes, Electron Decoupling with Dynamic Nuclear Polarization in Rotating Solids, J. Am. Chem. Soc. 139 (2017) 6310–6313. doi:10.1021/jacs.7b02714.

[13] E.L. Sesti, N. Alaniva, P.W. Rand, E.J. Choi, B.J. Albert, E.P. Saliba, F.J. Scott, A.B. Barnes, Magic Angle Spinning NMR Below 6 K with a Computational Fluid Dynamics Analysis of Fluid Flow and Temperature Gradients, J. Magn. Reson. (2017). doi:10.1016/j.jmr.2017.11.002.

[14] A.B. Barnes, E. Markhasin, E. Daviso, V.K. Michaelis, E.A. Nanni, S.K. Jawla, E.L. Mena, R. DeRocher, A. Thakkar, P.P. Woskov, J. Herzfeld, R.J. Temkin, R.G. Griffin, Dynamic nuclear polarization at 700MHz/460GHz, J. Magn. Reson. 224 (2012) 1–7. doi:10.1016/j.jmr.2012.08.002.

[15] P.P. Woskov, V.S. Bajaj, M.K. Hornstein, R.J. Temkin, R.G. Griffin, Corrugated Waveguide and Directional Coupler for CW 250-GHz Gyrotron DNP Experiments, IEEE Trans. Microw. Theory Tech. 53 (2005) 1863–1869.

[16] E.A. Nanni, S.K. Jawla, M.A. Shapiro, P.P. Woskov, R.J. Temkin, Low-loss transmission lines for high-power terahertz radiation, J. Infrared, Millimeter, Terahertz Waves. 33 (2012) 695–714. doi:10.1007/s10762-012-9870-5.

[17] Y. Matsuki, T. Idehara, J. Fukazawa, T. Fujiwara, Advanced instrumentation for DNP-enhanced MAS NMR for higher magnetic fields and lower temperatures, J. Magn. Reson. 264 (2016) 107–115. doi:10.1016/j.jmr.2016.01.022.

[18] E.O. Stejskal, J. Schaefer, J.S. Waugh, Magic-Angle Spinning and Polarization Transfer in Proton-Enhanced NMR, J. Magn. Reson. 28 (1977) 105–12. doi:https://doi.org/10.1016/0022-2364(77)90260-8.

[19] J. Schaefer, R.A. McKay, Multi-Tuned Single Coil Transmission Line Probe for Nuclear Magnetic Resonance Spectrometer, 1999.

[20] R.A. McKay, Probes for Special Purposes, Encycl. Magn. Reson. (2007) 1–4. doi:10.1002/9780470034590.emrstm0416.

[21] D.E.M. Hoff, B.J. Albert, E.P. Saliba, F.J. Scott, E.J. Choi, M. Mardini, A.B. Barnes, Frequency swept microwaves for hyperfine decoupling and time domain dynamic nuclear polarization, Solid State Nucl. Magn. Reson. 72 (2015) 79–89. doi:10.1016/j.ssnmr.2015.10.001.

[22] F.J. Scott, E.L. Sesti, E.J. Choi, A.J. Laut, J.R. Sirigiri, A.B. Barnes, Magic Angle Spinning NMR with Metallized Rotors as Cylindrical Microwave Resonators, Magn. Reson. Chem. 56 (2018) 831–835. doi:10.1002/mrc.4744.

[23] D.D. Traficante, Impedance: What it is, and why it must be matched, Concepts Magn. Reson. Part A1. 1 (1989) 73–92. doi:https://doi.org/10.1002/cmr.1820010205.

[24] J.A. Stringer, G.P. Drobny, Methods for the analysis and design of a solid state nuclear magnetic resonance probe, Rev. Sci. Instrum. 69 (1998) 3384–3391.

doi:10.1063/1.1149104.

[25] H. Yang, D. Staveness, S.M. Ryckbosch, A.D. Axtman, B.A. Loy, A.B. Barnes, V.S. Pande, J. Schaefer, P.A. Wender, L. Cegelski, REDOR NMR reveals multiple conformers for a protein kinase c ligand in a membrane environment, ACS Cent. Sci. 4 (2018) 89–96. doi:10.1021/acscentsci.7b00475.

[26] K.A. Collier, S. Sengupta, C.A. Espinosa, J.E. Kelly, J.I. Kelz, R.W. Martin, Design and construction of a quadruple-resonance MAS NMR probe for investigation of extensively deuterated biomolecules, J. Magn. Reson. 285 (2017) 8–17. doi:10.1016/j.jmr.2017.10.002.

Chapter 4: Magic angle spinning NMR with metallized rotors as cylindrical microwave resonators

Adapted from "Magic angle spinning NMR with metallized rotors as cylindrical microwave resonators" published by Faith J. Scott, Erika L. Sesti, Eric J. Choi, Alexander J. Laut, Jagadishwar R. Sirigiri, and Alexander B. Barnes in Magnetic Resonance in Chemistry, 56 (2018) 831-835. Doi: https://doi.org/10.1002/mrc.4744. Jagadishwar Sirigiri and Alexander Laut from Bridge12 Technologies, Inc. in Framingham MA collaborated on this project.

Abstract

I introduce a novel design for millimeter wave electromagnetic structures within magic angle spinning (MAS) rotors. In this demonstration, a copper coating is vacuum deposited onto the outside surface of a sapphire rotor at a thickness of 50 nanometers. This thickness is sufficient to reflect 197 GHz microwaves, yet not too thick as to interfere with radiofrequency fields at 300 MHz or prevent sample spinning due to eddy currents. Electromagnetic simulations of an idealized rotor geometry show a microwave quality factor of 148. MAS experiments with sample rotation frequencies of $\omega_r/2\pi$ = 5.4 kHz demonstrate that the drag force due to eddy currents within the copper does not prevent sample spinning. Spectra of sodium acetate show resolved ^{13}C J-couplings of 60 Hz and no appreciable broadening between coated and uncoated sapphire rotors, demonstrating that the copper coating does not prevent shimming and high-resolution NMR spectroscopy. Additionally, ^{13}C Rabi nutation curves of $\omega_1/2\pi$ = 103 kHz for both coated and uncoated rotors indicate no detrimental impact of the copper coating on radiofrequency coupling of the nuclear spins to the sample coil. I present this metal coated rotor as a first step towards an MAS resonator. MAS resonators are expected to have a significant

impact on developments in electron decoupling, pulsed DNP, room temperature DNP, DNP with low power microwave sources, and EPR detection.

4.1. Introduction

Dynamic nuclear polarization (DNP) increases nuclear magnetic resonance (NMR) sensitivity, resulting in signal enhancements of 115 in biological samples and >500 in model systems [1–5]. Microwave irradiation at specific DNP matching condition frequencies results in the transfer of polarization from electron spins to nuclear spins. DNP can be combined with magic angle spinning (MAS) to yield high sensitivity and high resolution spectra in amorphous and crystalline samples [6,7]. Unlike in static electron paramagnetic resonance (EPR) experiments which commonly employ a microwave cavity to increase the quality factor (Q), the spinning apparatus in MAS DNP probes complicates the application of resonators [8–11]. This lack of microwave resonators in MAS DNP probes results in quality factors near unity. The "single pass" irradiation strategy results in poor conversion of the microwave power into B_{1S} field intensity and a resulting low electron Rabi frequency ($\omega_{1S}/2\pi$). For example, microwave simulations indicate the average $\omega_{1S}/2\pi$ over a 18.6 μL sample is 500 kHz with 5 watts of microwave power [12]. Generation of microwave fields sufficiently intense to nearly saturate polarization transfer currently requires irradiation with high power sources, cryogenic cooling to below 25 K, or focusing of the microwave power into a small sample volume [13–15].

Microwave resonators implemented in combination with MAS will result in higher electron Rabi frequencies, and provide DNP spectroscopists with superior control over internal interactions within the spin Hamiltonian. Microwave MAS resonators have significant potential to impact applications of pulsed DNP, electron decoupling, and EPR detection [16–21]. Such time domain DNP methods show promise to increase DNP enhancements at room temperature, improve

targeted DNP transfers, mitigate paramagnetic relaxation effects, and yield structural constraints encoded by the dipolar hyperfine interaction. Pulsed DNP can be achieved with either short, hard pulses at a single frequency, or swept microwave frequency profiles, both of which require more intense microwave fields than are currently available without a resonator [12,19,20,22,23]. In general, microwave cavities increase the electron Rabi frequency by enhancing the B_{1s} field across the sample. Resonators can also be designed to minimize the electric field throughout the sample, which contributes to dielectric heating [24–28].

In this chapter I present a MAS rotor coated with metal as a first step towards an MAS resonator. Frequency adjustments of the resonance mode can be made by changing the dielectric constant of the sample within the sample space. The design consists of a thin metal coating on the outside of a sapphire MAS rotor with a gap in the center for resonance mode excitation. The 50 nm copper coating allows sample spinning and passage of radiofrequencies, yet should still reflect 197 GHz to form the boundaries of a resonator [29]. I describe the design and fabrication of a copper coated rotor and demonstrate effective spinning in a magnetic field with minimal attenuation of NMR signal.

4.2 Theory and fabrication

The concept of a metal coated rotor as a resonator hinges on the difference in skin depths between electron and nuclear resonance frequencies. The skin depth describes the penetration of electromagnetic radiation and is dependent on the wavelength. Whereas the microwave wavelength at 197 GHz resonant with electron spins is 1.52 mm in free space, the RF wavelength corresponding to ^{1}H at 300 MHz is 1.0 m. The corresponding skin depths within copper are 0.147 μm for 197 GHz microwaves, and 3.7 μm for 300 MHz radio frequency waves. If

frequencies corresponding to the ^{1}H Zeeman frequency pass freely through the metal coating, all frequencies to control and detect nuclear spins with lower gyromagnetic ratios follow.

4.2.1 Electromagnetic quality factor analysis

To gain insight into the range of microwave quality factors achievable with this type of design, we performed an electromagnetic treatment of an idealized metalized rotor geometry. The geometry below describes a smaller diameter cylinder of 1.8 mm outside diameter, with the metal coating in this case on the inner surface of the rotor. To permit meshing of the thin metal coating, we used a coating of 500 nm compared to the 50 nm thickness demonstrated in MAS NMR experiments. The required thickness of the metal will decrease at cryogenic temperature, following the temperature dependence of the skin depth. For example, our group is currently conducting MAS DNP experiments at a temperature of 5 K, where the copper skin depth at 197 GHz is 11 nm compared to 150 nm at room temperature. This means that although the 500 nm coating simulated and discussed in the section below may indeed result in substantial eddy currents, future implementations of the metal coating to establish a microwave boundary condition could be <11 nm thick. The geometry described and simulated below also includes conductive caps on the cylindrical resonator. Although these geometries and design are feasible to implement, I opted to perform the first experimental demonstration on the larger 3.2 mm rotors discussed in the previous section, due to experimental overlap with our currently operational MAS DNP probe housing 3.2 mm rotors.

A good metric of microwave coupling efficiency is the generated microwave field per watt of incident power. Previously reported [25] values of MAS DNP probes are 0.37 MHz/W$^{1/2}$, where the microwave field is given in the experimentally relevant units of the electron Rabi frequency, ω_{1S}. We simulated the geometry shown in **Figure 4.1, 4.2** which included a sample with a dielectric constant of 3.5 and loss tangent of 0.009, as well as the coupling horn and RF solenoid.

The frequency dependent response of the resonator is shown in **Figure 4.3**. A microwave resonance is observed at 197.6 GHz, which will yield 4.5 MHz/ $W^{1/2}$ using the same microwave source as reported above. Applying this resonator to future DNP experiments will represent a 12-fold improvement in electron Rabi frequency and a quality factor of 148. With the 15 watts of incident power at the sample we can now achieve in our laboratory, I expect an electron Rabi frequency of 17 MHz, which will be sufficient for pulsed DNP transfers utilizing the frequency swept integrated solid effect. Such a quality factor could also allow the same continuous wave DNP performance with 148x less microwave power.

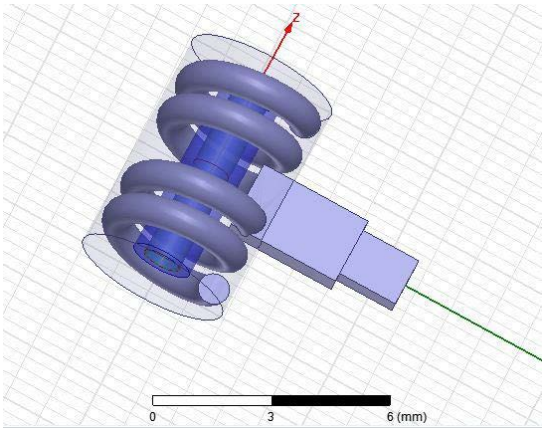

Figure 4.1 Electromagnetic simulation geometry for Q determination

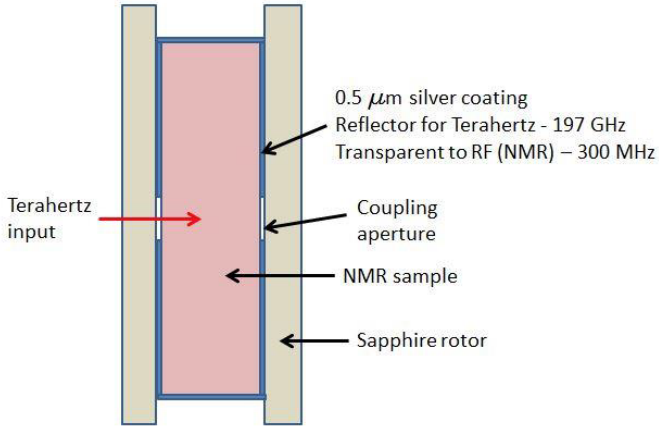

Figure 4.2 2D schematic of the model used in HFSS

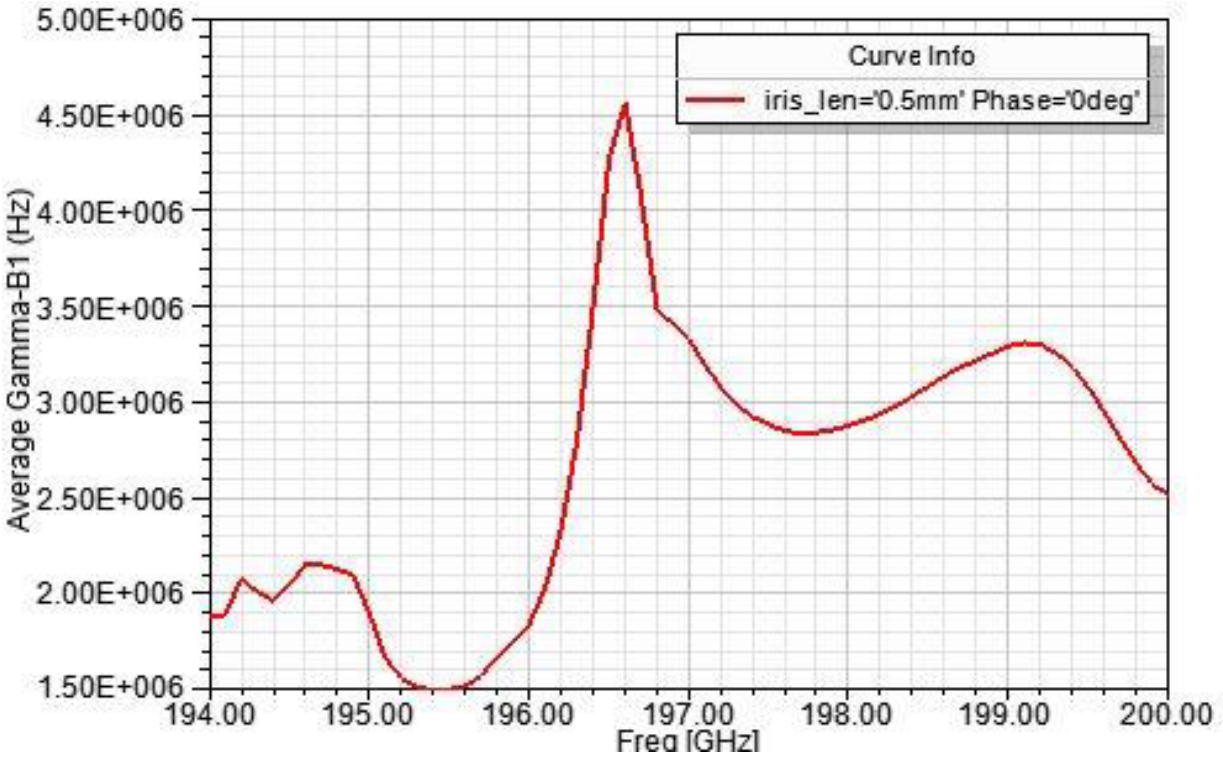

Figure 4.3 Electron Rabi frequency provided by the 1.8 mm OD resonator shown in **Figure 4.1 and 4.2** over the frequency band 194-200 GHz.

4.2.2 Skin depth of electromagnetic waves in copper

Although a thicker metal coating of 500 nm was employed in HFSS simulations due to meshing requirements of the electromagnetic calculation, far thinner metallized layers can be employed at cryogenic temperature. For instance, we now routinely perform MAS DNP experiments at 5 Kelvin in our laboratory [30]. The skin depth at 197 GHz of copper at 5 Kelvin is 11 nm compared to 150 nm at 298 K [31].

Skin depth is not an absolute boundary, but a description of the decay of the electric and magnetic fields within a conductor. The magnetic field $\mathbf{H}_c$ and electric field $\mathbf{E}_c$ inside a conductive layer are defined by the following equations [29]: $\mathbf{H}_c = \mathbf{H}_{\square} e^{-\xi/\delta} e^{i\xi/\delta}$ and

$\mathbf{E}_c = \sqrt{\frac{\mu_c \omega}{2\sigma}}(1-i)(\mathbf{n}\times\mathbf{H}_{\square})e^{-\xi/\delta}e^{i\xi/\delta}$ where $\mathbf{H}_{\square}$ is the magnetic field tangent to the outside surface of the conductor, μ_c is the magnetic permeability of the conductor, ω is the electromagnetic

frequency, σ is the conductivity, ξ is the coordinate into the conductor, and δ is the skin depth. If ξ is set equal to a value of 50 nm, $\mathbf{H}_c$ is 70% of initial intensity ($\mathbf{H}_{\square}$) for 197 GHz and 99% of initial intensity for 300 MHz. If the rotor coating is set to 50 nm, passage of 300 MHz and partial reflection of 197 GHz radiation is expected. Complete reflection of microwaves is not required to establish a resonant mode within the rotor.

4.2.3 Electromagnetic mode analysis

The metal coating described in this chapter is designed as a resonant structure for microwaves, but its resonant frequency depends on the dielectric constants of its constituent parts and contents. Additionally, the inner and outer diameter of the sapphire rotor tube will affect its resonant frequency. To determine the resonant frequency of the cylindrical structure, I first calculated eigenmode solutions using the Ansys HFSS (High Frequency Structure Simulator) software suite. Simulations were completed on a simplified rotor system consisting of a sapphire cylinder with a 3.175 mm outer diameter, 2.286 mm inner diameter, and 19.07 mm length (see **Figure 4.4**). The sample volume over the length of the radiofrequency (RF) coil is 25.4 μL. The rotor sleeve in the simulations was coated with a boundary layer with a conductivity of $5.8*10^7$ Siemens/m and a real relative permeability of 1. The skin depth at 197 GHz in ideal copper is 0.147 μm, thus the copper coating is one third the skin depth resulting in partial microwave confinement. The expected attenuation of the radio frequency NMR signal at 300 MHz from such a coating is negligible. An uncoated section of a width 2.77 mm (~2 wavelengths at 197 GHz) was included in the middle of the resonator for input of the microwaves and excitation of the mode. These initial simulations model an empty rotor (permittivity of free space is $8.85*10^{-12}$ F/m).

Figure 4.4 shows a strong TE_{02} mode resonating at 190.015 GHz. The frequency of the resonant mode is strongly dependent on the dielectric constant of the sample and the diameter of the rotor. The frequency of the resonant mode can be readily tuned to the EPR frequency by implementing cylinders with different diameters, or adjusting the dielectric constant of the sample.

The left portion of **Figure 4.4** shows a cross sectional view along the spinning axis of the rotor. There are multiple maxima in the magnetic field (**Figure 4.4b**) along the length of the rotor, indicating that strong H_1 fields are established over a large sample volume. The useful length of the microwave resonator is limited by the length of the RF coil required to manipulate and detect the nuclear spins. The cross-section view on the right of **Figure 4.4** illustrates the field intensity at the plane orthogonal to the spinning axis. The highest electric field intensity (shown in red in **Figure 4.4a**) is near the rotor wall, while the electric field is minimized in the regions of high H_1 intensity. The sapphire rotor has a high thermal conductivity which can readily dissipate heat generated by dielectric heating. The resonant rotor structure therefore should provide intense H_1 fields to improve EPR and NMR performance, while minimizing electric fields to mitigate microwave dielectric heating. Frequency adjustments can be made by changing the dielectric constant of the sample within the sample space [5].

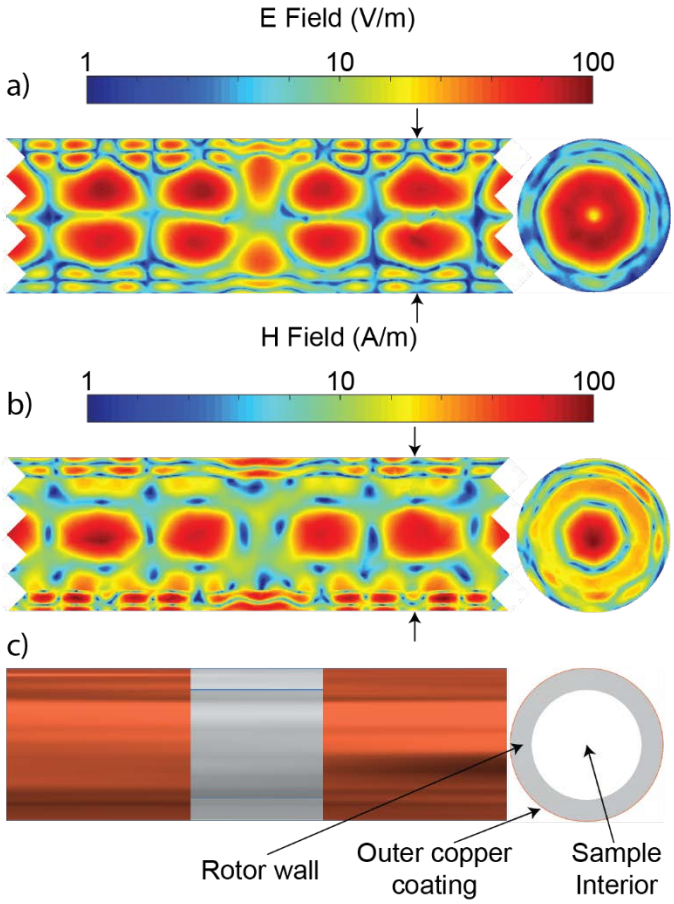

Figure 4.4 HFSS illustrations of TE_{02} mode inside the rotor. a) Electric (E) field phase independent plot. b) Magnetic (H) field phase independent plot. The left side of the figure shows a longitudinal cross section and the right side shows a transverse cross section taken at the point indicated on the right plot by black arrows. Scales for E and H are normalized from 1 to 100 and the color values follow a logarithmic scale. Red areas indicate the highest field intensity while blue areas indicate the lowest field intensity. c) Computer assisted design (CAD) of the resonator section illustrated above.

4.2.4 Fabrication

A sapphire rotor (Insaco, Inc., Quakertown, PA) was coated with copper to a thickness of 50 nm using vacuum deposition (New Wave Thin Films, Newark, CA). The sapphire cylinder was cleaned and areas not intended for coating were covered with masks. The masked cylinder was then placed in a vacuum chamber and the copper source material was bombarded with an electron beam. Atoms then evaporated off the source and coated all exposed surfaces in the vacuum chamber. A band 2.77 mm wide (~2 wavelengths at 197 GHz) was left uncoated to simulate the iris for the final resonator [32]. In addition, the copper coating was withheld from

the edges of the rotor by 4.3 mm to ensure that no copper would rub off on the stator bearings. The rotor design is shown in **Figure 4.5**.

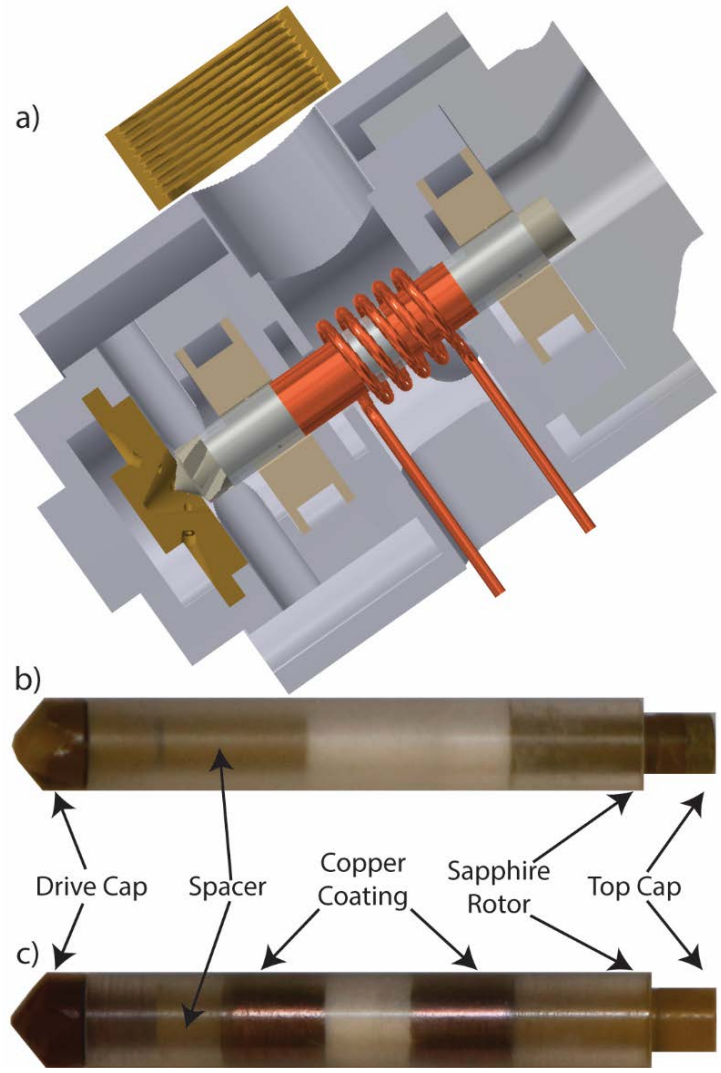

Figure 4.5 a) A CAD illustration of the rotor shown in the context of the stator. b) A sapphire rotor without any coating. c) The rotor with a copper coating of 50 nm.

4.3 NMR analysis of the coated rotor

The copper coated rotor was packed with 22.4 mg of sodium acetate-$^{13}C_2$ (Sigma-Aldrich) and an uncoated sapphire rotor was packed with 26.2 mg of sodium acetate-$^{13}C_2$ for comparison (**Figure 4.5b,c**). Rotors were spun at a frequency of $\omega_r/2\pi$ = 5.4 kHz in a custom machined stator equipped with a drive cup and bearings from Revolution NMR (Fort Collins, CO) pictured in

Figure 4.5a. The ^{1}H and ^{13}C carrier frequencies were 300.184 MHz and 75.495 MHz respectively at a magnetic field of 7 T. Cross polarization was performed with a ^{1}H Rabi frequency ($\omega_1/2\pi$) of 67 kHz, $\omega_1/2\pi$ of 62 kHz on ^{13}C, and a mixing time of 1 ms. The ^{13}C signal was acquired with a Hahn echo ($\omega_1/2\pi$ = 80 kHz for the carbon π pulse) and TPPM ^{1}H decoupling [33]. TPPM parameters were ^{1}H $\omega_1/2\pi$ of 70 kHz, pulse widths of 7.1 μs, and phase increments of 12°. The recycle delays were 500 ms. The intensity of each spectrum was scaled to reflect the weight of sample in each rotor. Resonances were fit and integrated using DMFit [34].

Nutation curves were measured to determine the effect of the copper coating on RF coupling to the sample (**Figure 4.6**). Nutation curves were recorded with 8 transients, and indirectly detected via CP to ^{13}C. **Figure 4.6** shows the $\omega_1/2\pi$ for ^{1}H is 103 kHz for both the coated and uncoated rotor. The fact that both $\omega_1/2\pi$ values are the same indicates that the RF is not being attenuated by the coating, which is important for ^{1}H decoupling and cross polarization.

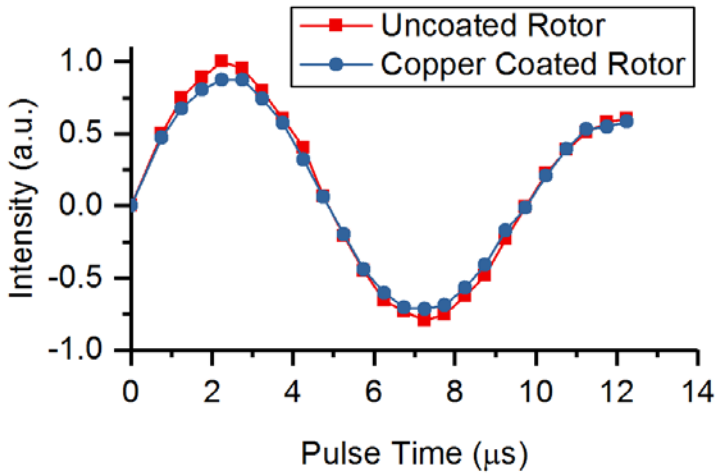

Figure 4.6 ^{1}H nutation curves of pulse time for copper coated and uncoated rotors containing sodium acetate-$^{13}C_2$. Signal intensity was found by fitting spectra in DMfit[34] and integrating the fit of each peak. The red curve is from the uncoated rotor, and the blue curve is from the copper coated rotor. Each set of data points was fit to a damped sine function to find the $\omega_1/2\pi$=103 kHz in both cases.

A cross-polarization Hahn echo experiment with and without copper coating on the rotor is shown in **Figure 4.7**, with 32 transients per spectrum. The spectra show both ^{1}H and ^{13}C frequencies passing through the copper coating in a cross-polarization experiment on sodium acetate-$^{13}C_2$. I observed a 10% attenuation of the intensity, but resolution of fine features in the spectrum such as J-splitting is conserved (see **Figure 4.7b** and **4.7c**). The preservation of narrow linewidths is important for high resolution NMR.

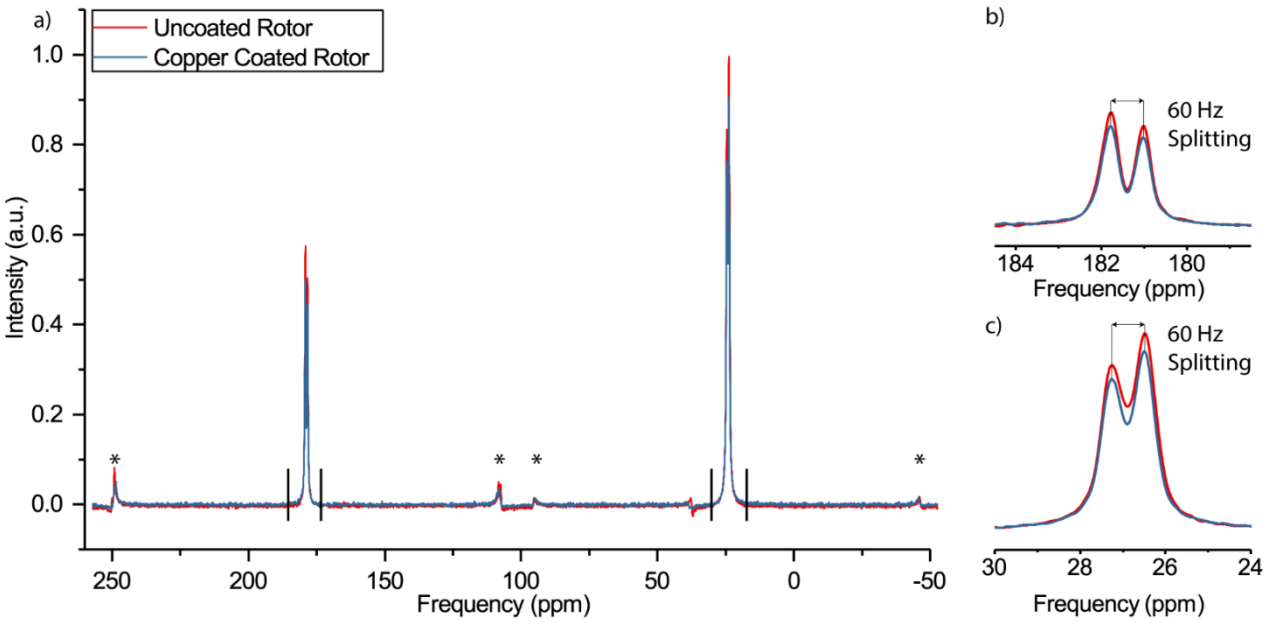

Figure 4.7 a) $^{13}C\{^{1}H\}$ CPMAS spectra taken on a sodium acetate-$^{13}C_2$ sample spinning at 5.4 kHz. 60 Hz J-splitting is visible in b) the carboxyl peak and c) the aliphatic peak. Spinning sidebands are denoted by an asterisk.

4.4 Discussion

In previous trials, the thickness of the metal coating prevented spinning and NMR radiofrequency passage. The first coating method attempted was to encase a rotor in a plastic mask and submerge it into a silver ion solution. The addition of a reducing solution then plated silver onto the exposed sapphire surface [35]. However, the thickness of this silver coating was difficult to control or measure. Furthermore, the initial metal coated rotor could only be spun at $\omega_r/2\pi$ = 1.5 kHz, and resulted in less than 1% NMR signal intensity compared to the uncoated

rotor. In the second trial, two rotors were plated by vacuum deposition at a thickness of 200 nm in copper and aluminum (New Wave Thin Films, Newark, CA; VTI, Reedsburg, WI). The copper coating gave 70% of the signal of the uncoated sample, and the aluminum sample gave 30% signal intensity. A 50 nm coating of copper produced the best results as presented above.

4.5 Conclusion

A novel MAS rotor design intended for use as a microwave cavity has been experimentally demonstrated to allow sufficient MAS NMR performance. The NMR experiments show that the MAS rotor spins at a frequency of 5.4 kHz and NMR resolution is retained. These results suggest resonant structures of this design are a viable strategy for MAS DNP development. Further experiments are required to optimize the MAS resonator frequency. Increased control over electron spin and hyperfine interactions should enable pulsed DNP and electron decoupling experiments in rotating solids.

References

[1] K.K. Frederick, V.K. Michaelis, B. Corzilius, T.-C. Ong, A.C. Jacavone, R.G. Griffin, et al., Sensitivity-Enhanced NMR Reveals Alterations in Protein Structure by Cellular Milieus, Cell. 163 (2015) 620–628. doi:10.1016/j.cell.2015.09.024.

[2] A.B. Barnes, G. De Paëpe, P.C. a van der Wel, K. Hu, C.-G. Joo, V.S. Bajaj, et al., High-Field Dynamic Nuclear Polarization for Solid and Solution Biological NMR, Appl. Magn. Reson. 34 (2008) 237–263. doi:10.1007/s00723-008-0129-1.

[3] C. Song, K.-N. Hu, C.-G. Joo, T.M. Swager, R.G. Griffin, TOTAPOL: A Biradical Polarizing Agent for Dynamic Nuclear Polarization Experiments in Aqueous Media, J. Am. Chem. Soc. (2006) 11385–11390. doi:10.1021/JA061284B.

[4] D. Lee, E. Bouleau, P. Saint-Bonnet, S. Hediger, G. De Paëpe, Ultra-low temperature MAS-DNP, J. Magn. Reson. 264 (2016) 116–124. doi:10.1016/j.jmr.2015.12.010.

[5] D.J. Kubicki, A.J. Rossini, A. Purea, A. Zagdoun, O. Ouari, P. Tordo, et al., Amplifying Dynamic Nuclear Polarization of Frozen Solutions by Incorporating Dielectric Particles, J. Am. Chem. Soc. 136 (2014) 15711–15718. doi:10.1021/ja5088453.

[6] A.B. Barnes, B. Corzilius, M.L. Mak-Jurkauskas, L.B. Andreas, V.S. Bajaj, Y. Matsuki, et al., Resolution and polarization distribution in cryogenic DNP/ MAS experiments, Phys. Chem. Chem. Phys. 12 (2010) 5861–5867. doi:10.1039/c003763j.

[7] K. Märker, M. Pingret, J.M. Mouesca, D. Gasparutto, S. Hediger, G. De Paëpe, A New Tool for NMR Crystallography: Complete 13C/15N Assignment of Organic Molecules at Natural Isotopic Abundance Using DNP-Enhanced Solid-State NMR, J. Am. Chem. Soc. 137 (2015) 13796–13799. doi:10.1021/jacs.5b09964.

[8] V. Weis, M. Bennati, M. Rosay, J.A. Bryant, R.G. Griffin, High-field DNP and ENDOR with a novel multiple-frequency resonance structure, J. Magn. Reson. 140 (1999) 293–299. doi:10.1006/jmre.1999.1841.

[9] F.J. Rosenbaum, Dielectric cavity resonator for ESR experiments, Rev. Sci. Instrum. 35 (1964) 1550–1554. doi:10.1063/1.1719205.

[10] E. Haindl, K. Möbius, H. Oloff, A 94 GHz EPR Spectrometer with Fabry-Perot Resonator, Zeitschrift Für Naturforsch. - Sect. A J. Phys. Sci. 40 (1985) 169–172. doi:10.1515/zna-1985-0211.

[11] I. Amity, A Fabry-Perot cavity for millimeter and submillimeter ESR spectrometers, Rev. Sci. Instrum. 41 (1970) 1492–1494. doi:10.1063/1.1684318.

[12] D.E.M. Hoff, B.J. Albert, E.P. Saliba, F.J. Scott, E.J. Choi, M. Mardini, et al., Frequency swept microwaves for hyperfine decoupling and time domain dynamic nuclear polarization, Solid State Nucl. Magn. Reson. 72 (2015) 79–89.

doi:10.1016/j.ssnmr.2015.10.001.

[13] T.F. Kemp, H.R.W. Dannatt, N.S. Barrow, A. Watts, S.P. Brown, M.E. Newton, et al., Dynamic nuclear polarization enhanced NMR at 187 GHz/284 MHz using an extended interaction Klystron amplifier, J. Magn. Reson. 265 (2016) 77–82. doi:10.1016/j.jmr.2016.01.021.

[14] K.R. Thurber, R. Tycko, Low-temperature dynamic nuclear polarization with helium-cooled samples and nitrogen-driven magic-angle spinning, J. Magn. Reson. 264 (2016) 99–106. doi:10.1016/j.jmr.2016.01.011.

[15] A. Carroll, C. Espinosa, K.W. Zilm, DNP and NMR in the Same Probe: A Room Temperature Approach to Developing DNP NMR for Small Samples, in: 57th Exp. Nucl. Magn. Reson. Conf., 2016.

[16] B. Corzilius, L.B. Andreas, A.A. Smith, Q.Z. Ni, R.G. Griffin, Paramagnet induced signal quenching in MAS – DNP experiments in frozen homogeneous solutions, J. Magn. Reson. 240 (2014) 113–123. doi:10.1016/j.jmr.2013.11.013.

[17] A. Henstra, W.T. Wenckebach, Dynamic nuclear polarisation via the integrated solid effect I : theory, Mol. Phys. 112 (2014) 1761–1772. doi:10.1080/00268976.2013.861936.

[18] A. Leavesley, D. Shimon, T.A. Siaw, A. Feintuch, D. Goldfarb, S. Vega, et al., Effect of electron spectral diffusion on static dynamic nuclear polarization at 7 Tesla, Phys. Chem. Chem. Phys. 19 (2017) 3596–3605. doi:10.1039/C6CP06893F.

[19] E.P. Saliba, E.L. Sesti, F.J. Scott, B.J. Albert, E.J. Choi, N. Alaniva, et al., Electron Decoupling with Dynamic Nuclear Polarization in Rotating Solids, J. Am. Chem. Soc. 139 (2017) 6310–6313. doi:10.1021/jacs.7b02714.

[20] T.A. Siaw, A. Leavesley, A. Lund, I. Kaminker, S.-I. Han, A versatile and modular quasi

optics-based 200 GHz dual dynamic nuclear polarization and electron paramagnetic resonance instrument, J. Magn. Reson. 264 (2016) 131–153. doi:10.1016/j.jmr.2015.12.012.

[21] J.M. Spaeth, I. Tkach, S. Greulich-Weber, H. Overhof, High-field optically detected EPR and ENDOR of semiconductor defects using W-band microwave Fabry-Perot resonators, Magn. Reson. Chem. 43 (2005) 153–165. doi:10.1002/mrc.1663.

[22] S. Takahashi, L.-C. Brunel, D.T. Edwards, J. van Tol, G. Ramian, S.-I. Han, et al., Pulsed electron paramagnetic resonance spectroscopy powered by a free-electron laser, Nature. 489 (2012) 409–413. doi:10.1038/nature11437.

[23] T. Idehara, E.M. Khutoryan, Y. Tatematsu, Y. Yamaguchi, A.N. Kuleshov, O. Dumbrajs, et al., High-Speed Frequency Modulation of a 460-GHz Gyrotron for Enhancement of 700-MHz DNP-NMR Spectroscopy, J. Infrared, Millimeter, Terahertz Waves. 36 (2015) 819–829. doi:10.1007/s10762-015-0176-2.

[24] P.L. Gor'kov, E.Y. Chekmenev, C. Li, M. Cotten, J.J. Buffy, N.J. Traaseth, et al., Using low-E resonators to reduce RF heating in biological samples for static solid-state NMR up to 900 MHz, J. Magn. Reson. 185 (2007) 77–93. doi:10.1016/j.jmr.2006.11.008.

[25] E.A. Nanni, A.B. Barnes, Y. Matsuki, P.P. Woskov, B. Corzilius, R.G. Griffin, et al., Microwave field distribution in a magic angle spinning dynamic nuclear polarization NMR probe, J. Magn. Reson. 210 (2011) 16–23. doi:10.1016/j.jmr.2011.02.001.

[26] G.G. Maresch, R.D. Kendrick, C.S. Yannoni, High-temperature NMR using inductive heating, Rev. Sci. Instrum. 61 (1990) 77–80. doi:10.1063/1.1141903.

[27] V.P. Denysenkov, M.J. Prandolini, A. Krahn, M. Gafurov, B. Endeward, T.F. Prisner, High-field DNP spectrometer for liquids, Appl. Magn. Reson. 34 (2008) 289–299.

doi:10.1007/s00723-008-0127-3.

[28] F.D. Doty, J. Kulkarni, C. Turner, G. Entzminger, A. Bielecki, Using a cross-coil to reduce RF heating by an order of magnitude in triple-resonance multinuclear MAS at high fields, J. Magn. Reson. 182 (2006) 239–253. doi:10.1016/j.jmr.2006.06.031.

[29] J.D. Jackson, Classical Electrodynamics, in: 3rd ed., Wiley, 1998: pp. 352–356.

[30] E.L. Sesti, N. Alaniva, P.W. Rand, E.J. Choi, B.J. Albert, E.P. Saliba, et al., Magic Angle Spinning NMR Below 6 K with a Computational Fluid Dynamics Analysis of Fluid Flow and Temperature Gradients, J. Magn. Reson. (2017). doi:10.1016/j.jmr.2017.11.002.

[31] N.J. Simon, E.S. Drexler, R.P. Reed, Properties of Copper and Copper Alloys at Cryogenic Temperatures, 1992. doi:10.6028/NIST.MONO.177.

[32] G. Annino, J.A. Villanueva-Garibay, P.J.M. van Bentum, A.A.K. Klaassen, A.P.M. Kentgens, A high-conversion-factor, double-resonance structure for high-field dynamic nuclear polarization, Appl. Magn. Reson. 37 (2010) 851–864. doi:10.1007/s00723-009-0091-6.

[33] A.E. Bennett, C.M. Rienstra, M. Auger, K. V. Lakshmi, R.G. Griffin, Heteronuclear decoupling in rotating solids, J. Chem. Phys. 103 (1995) 6951. doi:10.1063/1.470372.

[34] D. Massiot, F. Fayon, M. Capron, I. King, S. Le Calvé, B. Alonso, et al., Modelling one- and two-dimensional Solid State NMR spectra, Magn. Reson. Chem. 40 (2002) 70–76. doi:10.1002/mrc.984.

[35] H.D. Curtis, Methods of Silvering Mirrors, Publ. Astron. Soc. Pacific. 23 (1911) 13–32. doi:10.1086/122040.

Chapter 5: Gyrotron control with LabVIEW

5.1 Overview of LabVIEW

LabVIEW is our chosen interface to the Spellman high power amplifier and by extension, the gyrotron (National Instruments, Austin, TX). There are several other controls that influence microwave output such as the gun coil (TDK Lambda, Tokyo, Japan), main magnet (Cryomagnetics Inc., Oak Ridge, TN), alignment stages (Thorlabs, Newton, NJ), and most notably, the arbitrary waveform generator (AWG) channel on the Redstone spectrometer (TNMR, Tecmag, Inc., Houston, TX). However, LabVIEW protects the electron gun surface by turning off the high voltage immediately if one or more interlocks are triggered.

The virtual instruments or VIs in the "GyroControl_(Date)" project folder monitor many inputs by RS232 electrical interface, and command the power supply to generate AC and DC voltage for the gyrotron. Many of the inputs serve as interlock set points, which turn off the gyrotron in a controlled and safe manner in case of a system failure. The main interlocks are internal gyrotron pressure, water temperature of the gyrotron cooling lines, and the temperature of the magnet surrounding the gyrotron. These interlocks protect the frequency agile gyrotron during electron decoupling experiments and continuous frequency microwave experiments. Construction and processing of a new gyrotron lasts six months to 1.5 years, so it is in the DNP spectroscopist's best interest to keep the gyrotron functioning optimally and protect the gyrotron from damage with the interlocks found in LabVIEW.

5.1.1 Program files

A virtual instrument (VI) is a program file (extension ".vi") that can collect data and trigger connected instrumentation, such as the high voltage power supply. VIs consist of a front end

called the “front panel” and a back end called the “block diagram” and can be linked together into complex units using global variables.

5.1.2 Front panel

The front panel is the VI user interface window with a grey background that first appears when the VI is opened (**Figure 5.1**). When the VI is not running, the various controls, indicators, and formatting objects can be moved around to any orientation and values in control boxes can be saved as the default value. When the VI is running, only front panel control variables are editable and the file cannot be saved. The VI can be started with the straight arrow or repeating arrows in the upper toolbar and if it runs successfully, it can be stopped with the stop sign button.

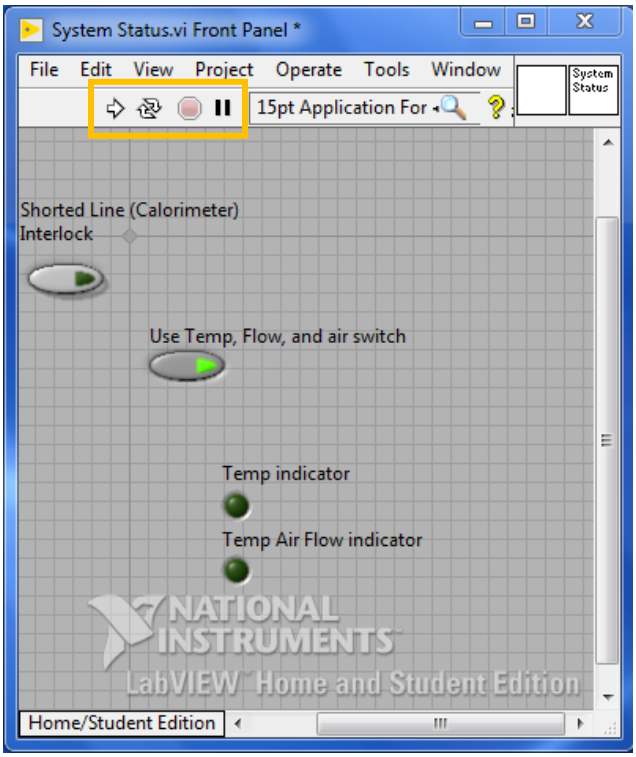

Figure 5.1 Front panel for “System Status.vi” in in stopped mode (white arrows and faded stop sign). Start, stop and pause buttons are indicated by the orange box.

5.1.3 Block diagram

The block diagram window can be accessed by navigating in the top menu to “Window>Show Block Diagram”. A block diagram represents the visual program that is meant to be run by the

current VI (**Figure 5.2**). Controls, indicators, functions, and other components are linked together by “wires” that indicate the order and direction of operations. As with the front panel, it can only be edited when the VI is not running. The lightbulb button helps troubleshooting by slowing the VI and highlighting each step as it activates or fails.

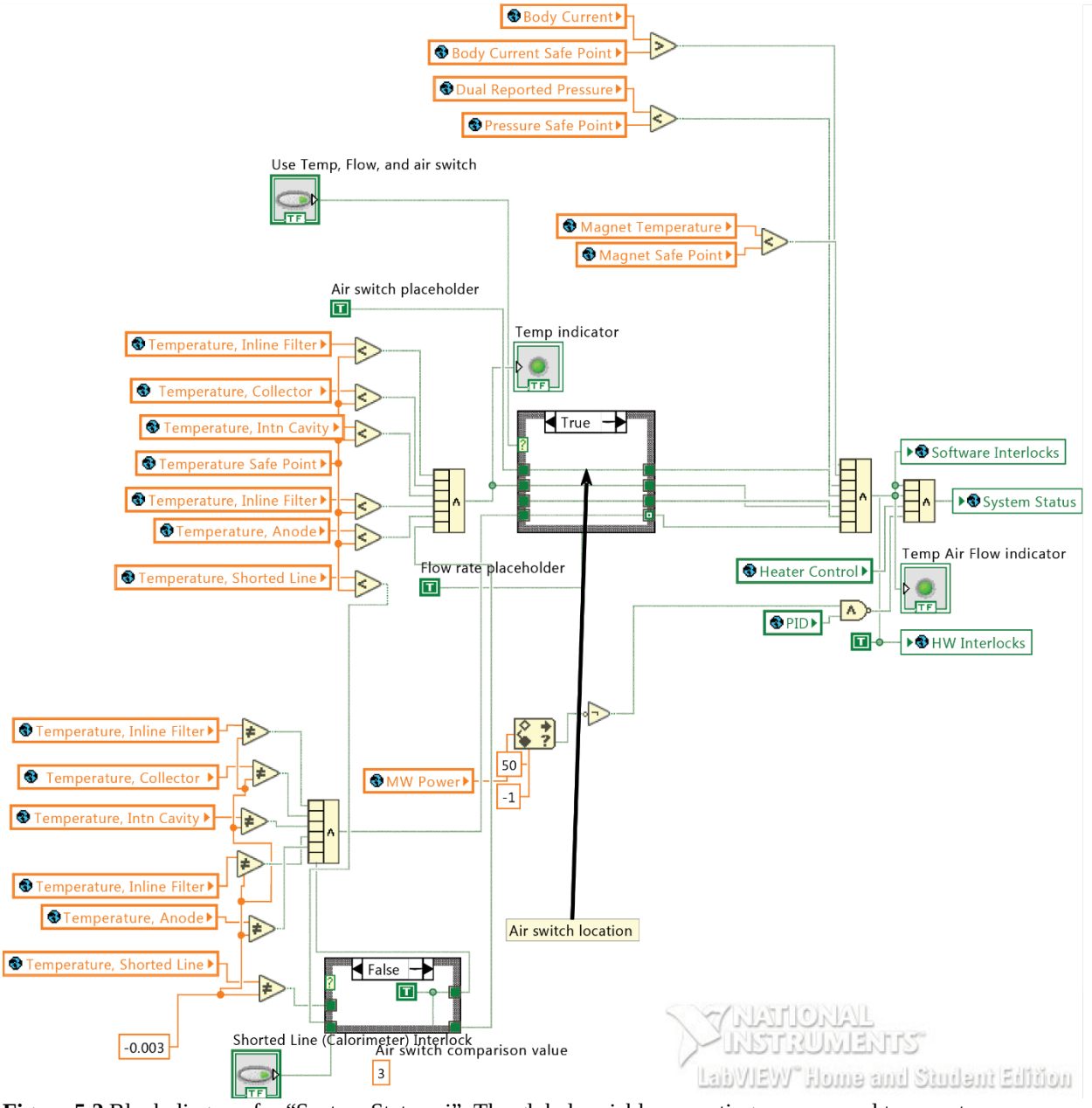

Figure 5.2 Block diagram for “System Status.vi”. The global variables reporting pressure and temperature are brought here. These values are compared with desired safe points to turn “system status” global variable to true or false. If system status reads false, the heater current and DC voltage are set to zero in “Control and Graphing.vi”. Note that that the front panel does not reflect the complexity of the VI function.

5.1.4 Controls and indicators

Controls are variables placed on either window of a VI. They act as a variable writer and can change the value of true/false (Boolean), string (alphanumerical characters), numerical, and many other types of variables. Indicators receive the information from the controls after functions have been performed on that information. Control wires come out of the right side of control blocks, and indicator wires connect into the left side of the block, so that the entire block diagram may be "read" from left to right. A simple example using controls and indicators is shown in **Figure 5.3**. If a control or indicator is placed on the front end, its corresponding marker will be placed on the block diagram. However, a "constant" type control will not generate a front panel equivalent as the value is entered directly in the block diagram.

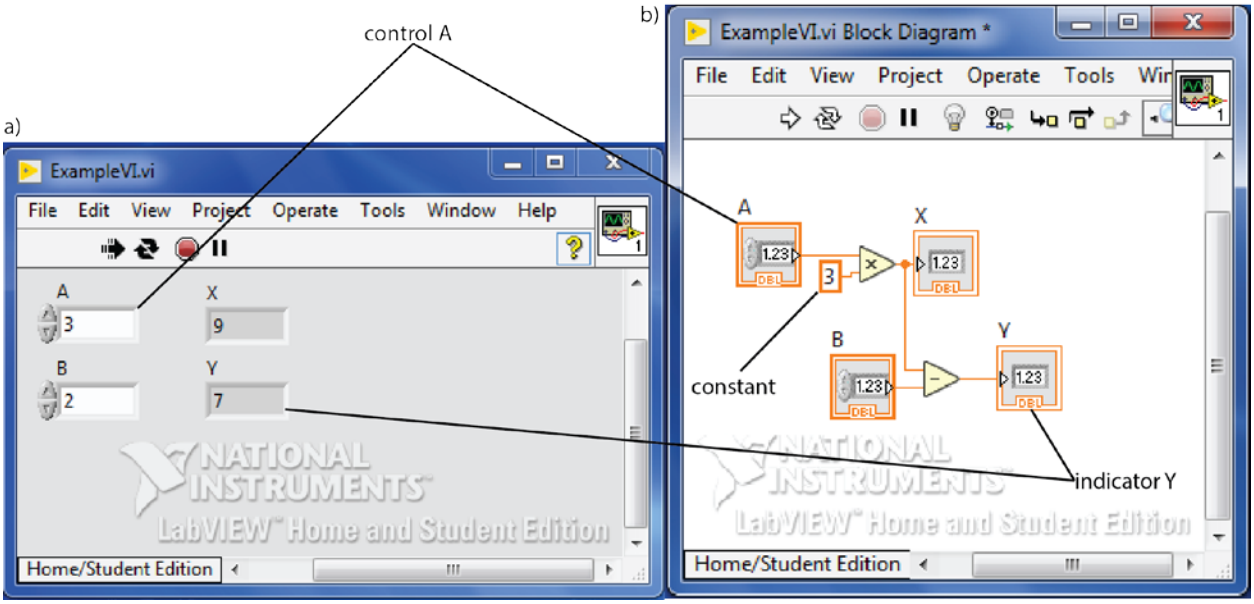

Figure 5.3 a) Front panel and b) block diagram for a simple VI representing the equations A*3=X and A*3-B=Y. The front panel is shown in continuous run mode and the block diagram is shown in the stopped mode.

5.1.5 Global variables

Global variables span different VIs. They can be set as either a control or an indicator type, but it is best practice to "write" only one indicator per global variable. References to a global variable can be found by right-clicking the variable and navigating to "Find>Global References". A collection of all global variables named "Global.vi" can be found under the subfolder "Globals"

in the current “GyroControl_(Date)” folder. “Global.vi” is unique because it does not have a block diagram, but only a front panel (**Figure 5.4**). The pressure safe point, temperature safe point, and heater step size are entered directly into “Global.vi”. Heater step size determines the value by which the heater current can increase or decrease every LabVIEW cycle. Without this value to slow down the heater value, the electron gun would be damaged by rapid heating and cooling. The heater step size can be changed under the “Heater controls” tab in “Global.vi”. Proportional-integral-derivative (PID) values are also entered into “Global.vi” to control the electron beam current by adjusting the AC heater current, but these values do not need to be changed once they are optimized.

Figure 5.4 “Global.vi” front panel showing System Status tab.

5.2 VI functions

The VIs controlling the gyrotron collect data from various sources, analyze it with respect to input values added in the user interface, and determine the set points of the DC voltage and AC

current on the gyrotron (**Figure 5.5**). The user types values into the "Global.vi" for pressure set point, water temperature set point, and heater step size, and sets the desired beam current, heater current, and DC voltage in "Control and Graphing.vi".

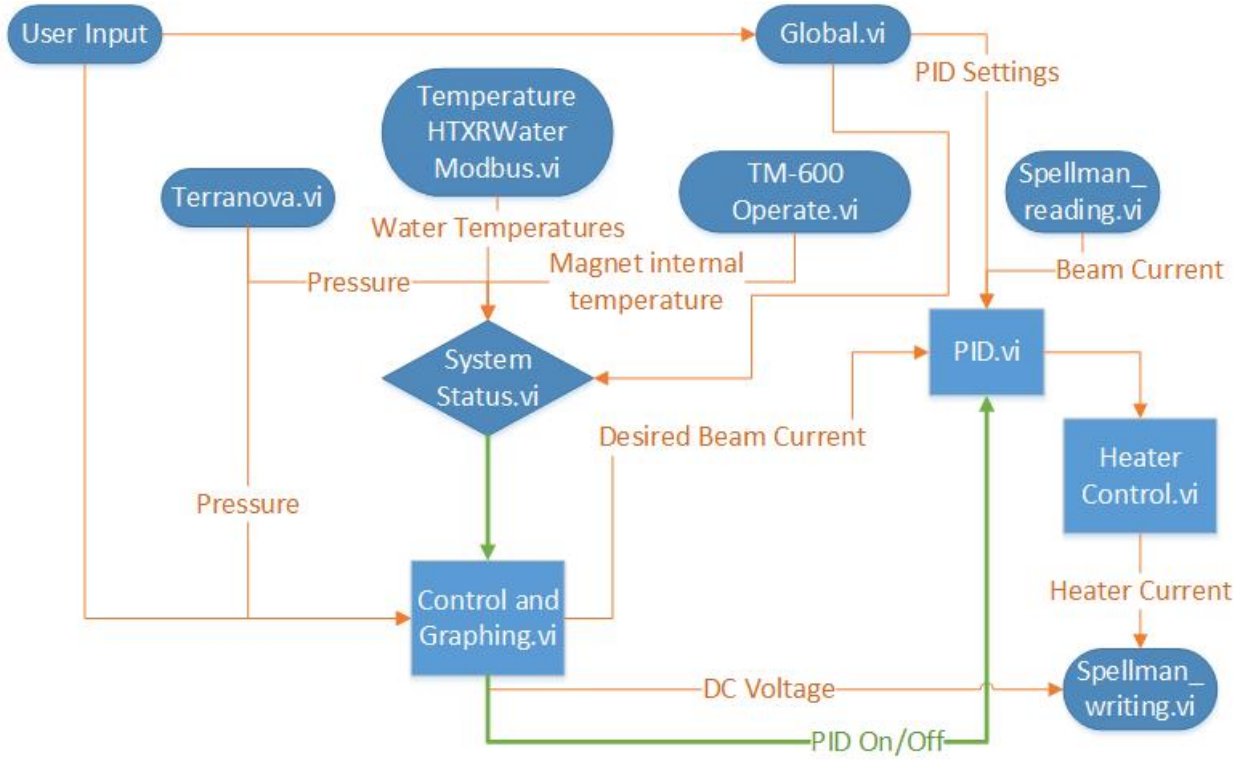

Figure 5.5 Flowchart showing the interactions of VIs. Orange lines show the flow of numerical values. Green lines show transmission of a true/false value.

"Control and Graphing.vi", "Start.vi", and "System status.vi" were originally created at the Massachusetts Institute of Technology and were adapted for use with our gyrotron system. "TM600-operate.vi" was written by Cryomagnetics, Inc. and modified to report the values of the cryogen-free magnet surrounding the gyrotron (Traverse City, MI). A temperature above 5 K is a sign that the magnet coil has quenched and is no longer generating a magnetic field. Without a magnetic field, the electron beam will spread out and electron impact will heat different parts of the gyrotron, causing a rise in pressure. This pressure increase is dangerous for the electron gun, so the interlock will set the gyrotron DC voltage to zero to stop the electron beam and slowly decrease the heater current to zero to protect the electron gun surface from oxidation (**Figure**

5.6). Other interlocks read different values, but shut down the gyrotron in the same manner. The workings of the VIs for the pressure interlock, water temperature interlock, and electron beam current input are described in greater detail below.

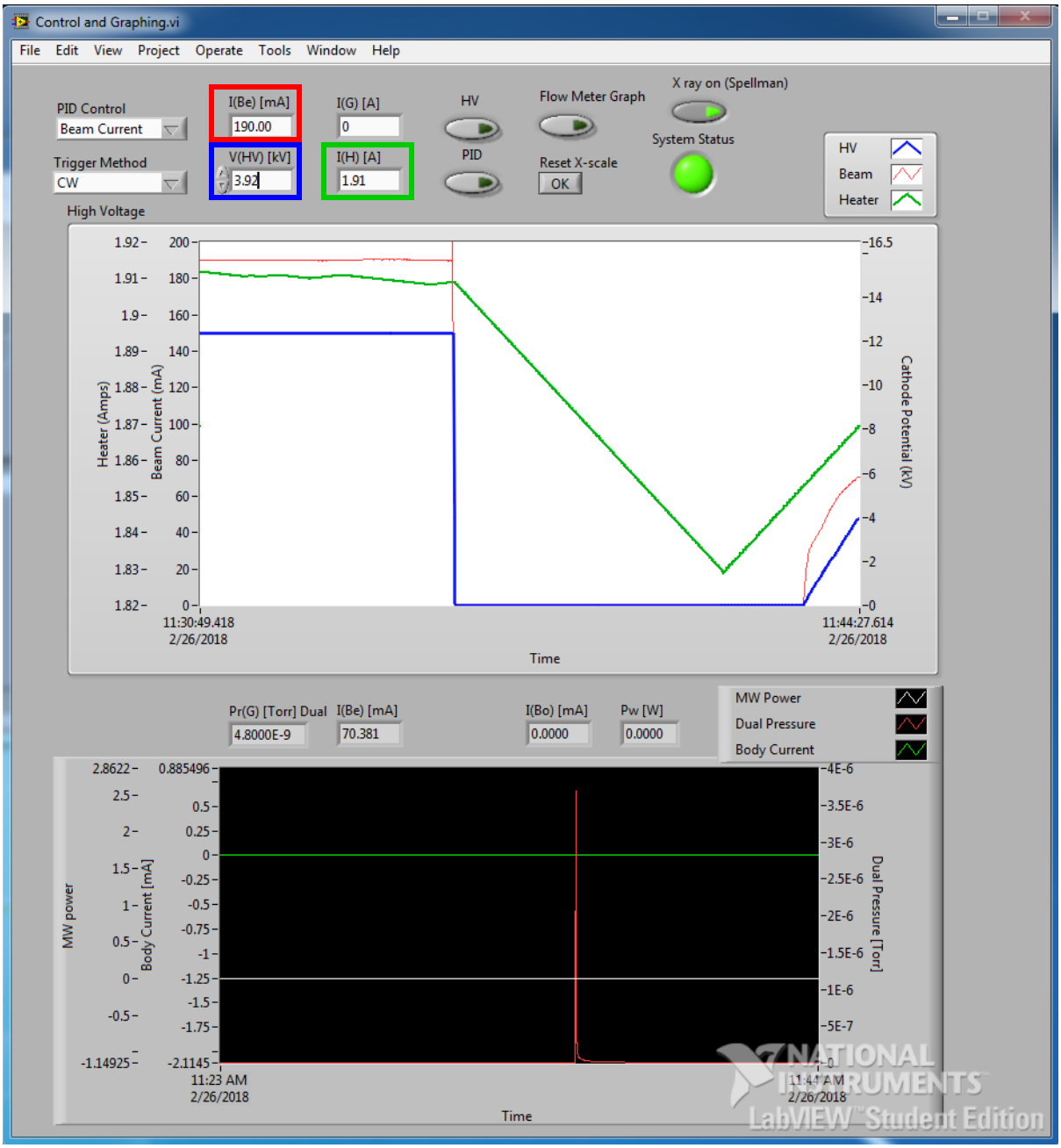

Figure 5.6 "Control and graphing.vi" after an interlock event (pressure spike in red on lower graph) and manual recovery. PID electron beam current set point is indicated in the red box, DC voltage input is indicated in the blue box, and desired AC heater current value is indicated in the green box.

5.2.1 Spellman high voltage power supply

The Spellman power supply is controlled through LabVIEW, unlike the other instruments which simply give information to LabVIEW. The power supply is set up for remote control, and in this mode only "CONTROL POWER ON" can be turned on and off from the front of the unit [1]. No other controls are available from the front of the power supply panel (**Figure 5.7b**). The orange "CONTROL POWER ON" button must be activated before the unit can be controlled through LabVIEW. Note- all three buttons on the front of the power supply should be able to illuminate. If the power supply does not switch to X-RAY ON after the X-RAY ON command is sent in LabVIEW, there may be a burnt-out lightbulb in the cavity behind one of the buttons.

Figure 5.7 a) The front panel of "Spellman_writing.vi" on LabVIEW. The dropdown box to select the VISA port is shown in the upper left hand corner. b) The front panel of the Spellman power supply unit. The buttons for CONTROL POWER ON, X-RAY OFF and X-RAY ON are on the right.

Gyrotron voltage and current values are sent to the power supply by “Spellman_writing.vi”. The COM channel that virtual instrument software architecture (VISA) commands are sent to is selected by a drop down menu on the front panel (**Figure 5.7a**). “VISA resource name” is set to COM3 in the **Figure 5.7a**, but the correct value could change based on the configuration of connections at the back of the LabVIEW computer. Values sent to the Spellman power supply, including the command to turn X-RAY ON, the heater current, and the DC voltage must be converted into an integer format coded according to the Spellman power supply manual and concatenated into a single phrase. A checksum confirms that the phrase is not corrupted- if this value is incorrect, the power supply will not accept the command. The phrase with the checksum at the end is sent to the power supply unit. The command to allow high voltage out of the power supply is labeled “X-RAY ON,” although no X-rays are emitted from the gyrotron. DC voltage is increased to change the potential across the electron gun. A higher potential results in a lower microwave frequency. AC current passes through the heater filament in the electron gun. Electron gun cathode surface temperature determines the current of electrons ejected as part of the electron beam, which contributes to microwave power output.

If LabVIEW is disconnected from the power supply after the program has sent a command for a non-zero AC current or DC voltage, the unit will attempt to remain at those values until a data packet with new AC and DC values is received by the power supply. This could result in damage to the power supply or the electron gun after a power outage. “Spellman_reading.vi” allows the LabVIEW project to read the value of the electron beam current for PID control of the electron gun heater.

"Spellman_reading.vi" has an integer format with a checksum similar to "Spellman_writing.vi", but the data packet contains a request for information instead of a command to change values. The requested value for the electron beam current (**Figure 5.7b**, upper left display) is separated from the return phrase and translated into a numerical format that can be used by "PID.vi".

The Spellman unit will turn off high voltage and beam current on its own if it detects unsafe conditions such as an arc or overcurrent. An overcurrent alarm may occur if the beam current is over 200 mA. The power supply output values only report up to 195 mA.

5.2.2 Terranova vacuum ion pump power supply

The Terranova vacuum ion pump power supply control module (**Figure 5.8a**) supplies a high voltage to operate the vacuum ion pumps and measures the pressure by the small current generated when ionized gases collide with the getter [2]. "Terranova.vi" sends a request for pressure values to the power supply through a VISA interface and receives an alphanumerical string in return (**Figure 5.8b**). That string is interpreted according to the codes given in the Terranova power supply manual and separated into numerical values. These numerical values are then submitted to a global variable. "System Status.vi" compares the global value with the pressure set point defined in "Global.vi" and determines whether the Spellman power supply should be set to zero.

Terranova hardware interlock

The Terranova power supply has a hardware interlock which provides a constant voltage to the interlock input on the back of the Spellman power supply (**Figure 5.9**). If this voltage is ever interrupted by the Terranova unit losing power or the pressure increasing past the hardware interock set point, the gyrotron AC current and DC voltage are instantly set to zero, which is not ideal for the electron gun.

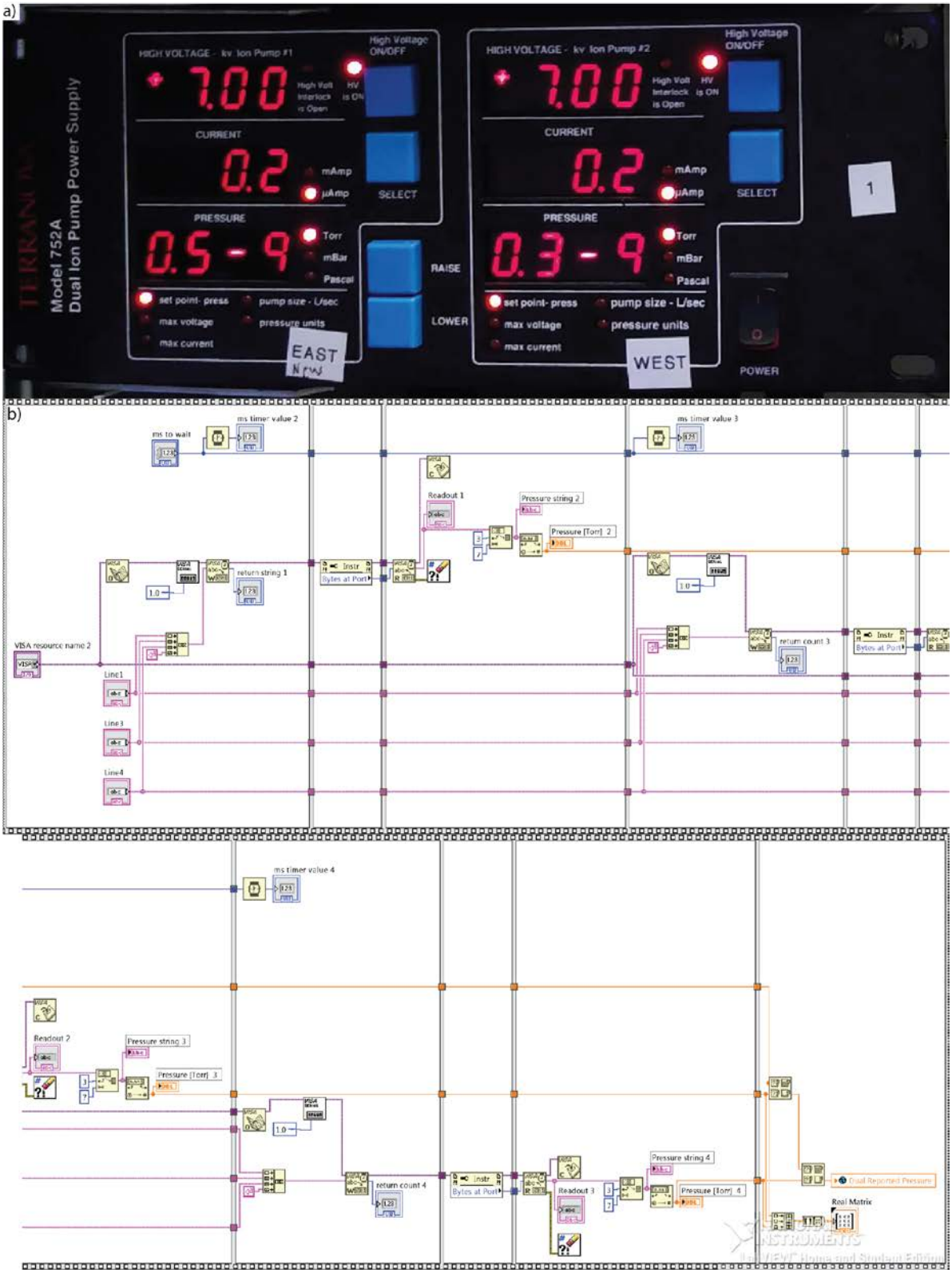

Figure 5.8 a) Terranova vacuum ion pump power supply front panel. b)"Terranova.vi" block diagram (wrapped from top right to bottom left). The film-style boxes ensure that all functions in a frame are activated before proceeding to the next frame.

It is advantageous to set the pressure interlocks to trigger the hardware interlock higher than the software interlock during gyrotron operation. The hardware interlock should be set when the gyrotron is not under LabVIEW control because the supply sends the value on-screen to LabVIEW for the software interlock. The hardware interlock value is changed by pressing the up and down arrows on the front of the Terranova power supply screen and the interlock value is shown on the panel screen. This can cause the software interlock to trigger if the LabVIEW pressure set point is less than the hardware set point during the setting process.

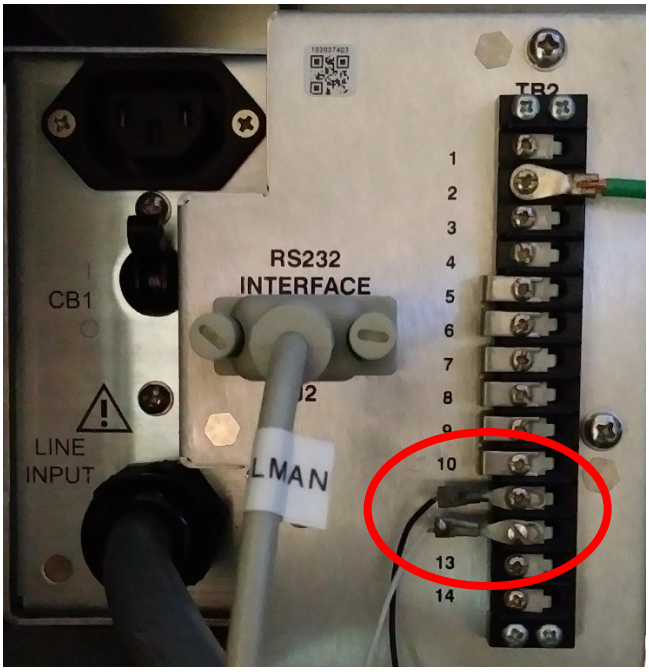

Figure 5.9 Hardware interlock input on the back of the Spellman power supply.

5.2.3 OptiTemp heat exchanger

The OptiTemp water heat exchanger provides cooling water for the gyrotron cavity, collector, and the resistive gun coil magnet. Thermometers inside the heat exchanger return lines operate as Modbus "slave" units and respond to a request for information from a Modbus subVI within "TemperatureHTXRWaterModbus.vi" (**Figure 5.10**) [3]. This provides values for the

temperature of each line, translated and calibrated in LabVIEW so that the shorted line temperature matched the tank output temperature. When the thermometers are disconnected or malfunctioning, they report a value that is read out as -0.003° C on the new calibrated scale. Therefore a section has been added to "systemstatus.vi" (**Figure 5.2**) to activate the interlock if any of the thermometer channels read -0.003. Unlike most other VIs in the GyroControl project, "TemperatureHTXRWaterModbus.vi" must be started manually to read the values from the instrument and convert them into usable temperatures for the interlock. The VI should be started in the continuous state (two revolving arrows button) so that the VI continues to report new temperatures into the global variables.

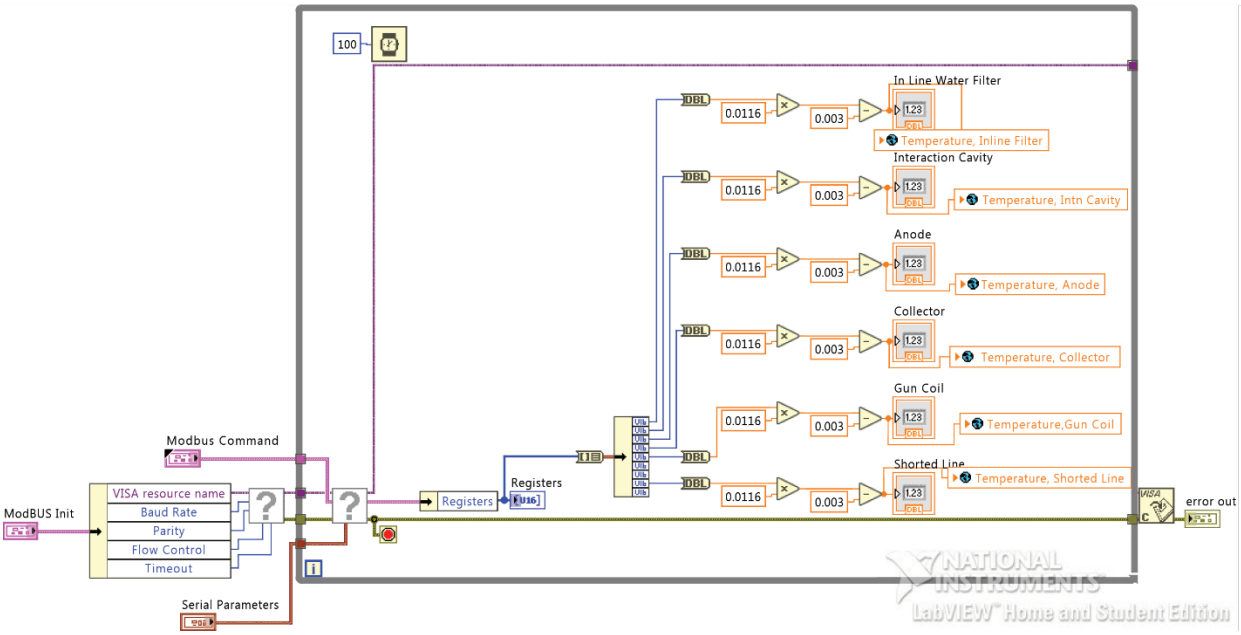

Figure 5.10 "TemperatureHTXRWaterModbus.vi" block diagram. Note the multiplication and subtraction values used to get an accurate water temperature.

5.3 LabVIEW operation

Before using LabVIEW, make sure the gyrotron is ready. The Spellman power supply, OptiTemp temperature monitors, and the Terranova power supply should all be connected to the computer running LabVIEW by RS232 connections. The gyrotron should be connected to the

Spellman high voltage power supply and the gyrotron anode should be grounded. The Terranova vacuum ion pump power supply should be properly connected to the Spellman power supply as detailed above and turned on. The Spellman power supply should be plugged in and the front button “CONTROL POWER ON” pressed so that “CONTROL POWER ON” and “X-RAY OFF” are both illuminated. Open “Start.vi” and “TemperatureHTXRWaterModbus.vi” from the latest folder marked “GyroControl_(Date)” (**Figure 5.11**). When “Start.vi” is opened, “Control and Graphing.vi” will also open.

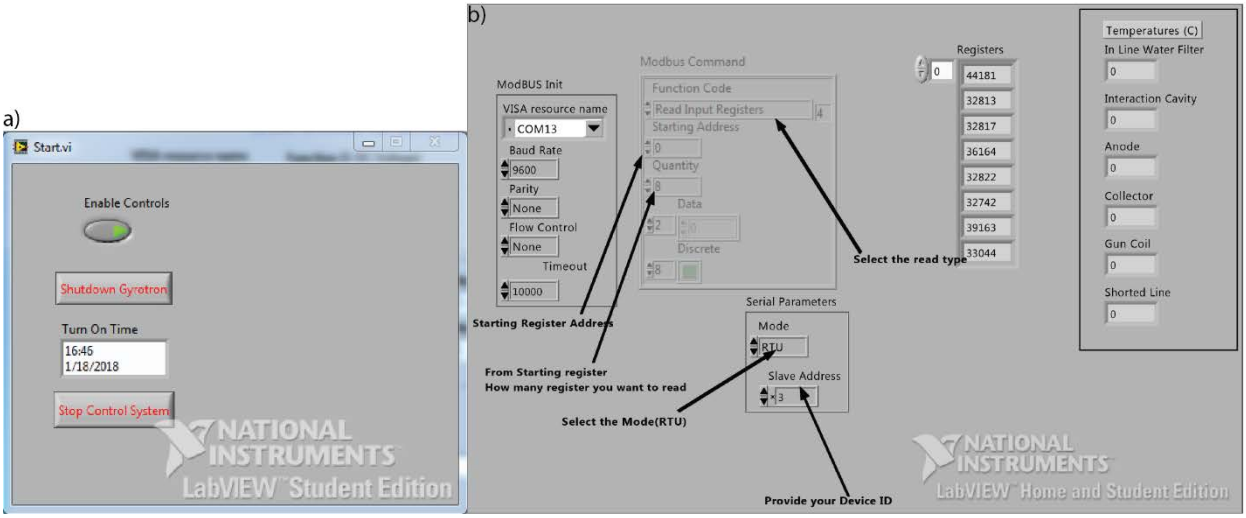

Figure 5.11 a) “Start.vi” front panel in continuous run mode. b) “TemperatureHTXRWaterModbus.vi” front panel.

Start collecting data on the water temperature data by clicking the two revolving arrows button on the water temperature monitor “TemperatureHTXRWaterModbus.vi”. Make sure the heater current and DC voltage are set to zero before using “Start.vi”. To allow DC voltage and AC current input, click the arrow on the “Start.vi”, activate the rocker switch under “enable controls” on “Start.vi”, and activate the “X ray on (Spellman)” rocker switch on “Control and Graphing.vi”. This should cause the Spellman power supply to illuminate to “X-RAY ON.” AC current and DC voltage can now be set in “Control and Graphing.vi.” “Control and Graphing.vi” has a PID functionality that allows for an electron gun heater value to be inserted in the box labeled “I(Be) (mA).” Both the rocker switch for “HV” and “PID” must be active (green

illuminated) for the PID control to work. It is recommended that PID control is not activated until the gyrotron has been brought within 10 mA of the desired beam current manually (**Figure 5.12**). When “Start.vi” is running, the top menus containing the stop buttons for “Control and Graphing.vi” and “Start.vi” will both disappear. To stop the program, make sure AC current and DC voltage are at zero on the front of the Spellman power supply panel (**Figure 5.7a**, upper right and lower left display), then press “Stop Control System.” The “X-RAY ON” button will still be illuminated on the front of the power supply, but now the “X-RAY OFF” button can be activated manually.

5.4 Conclusion

Information from the vacuum ion pumps, water heat exchanger, and magnet is taken into interlocks to keep the gyrotron electron gun safe when it is not observed by users. The LabVIEW program commands the Spellman power supply to provide the base voltage for microwave power output. Microwave output frequency can be changed on a fast timescale by ungrounding the gyrotron anode and connecting it to a separate low capacitance, high voltage power supply (Trek 580), controlled through TNMR. This process allows for frequency agility of the microwaves and electron decoupling during DNP for narrower linewidths and increased intensity of DNP-NMR signals. Frequency agility is only made available by keeping the gyrotron safe so that it can be used for repeated experiments.

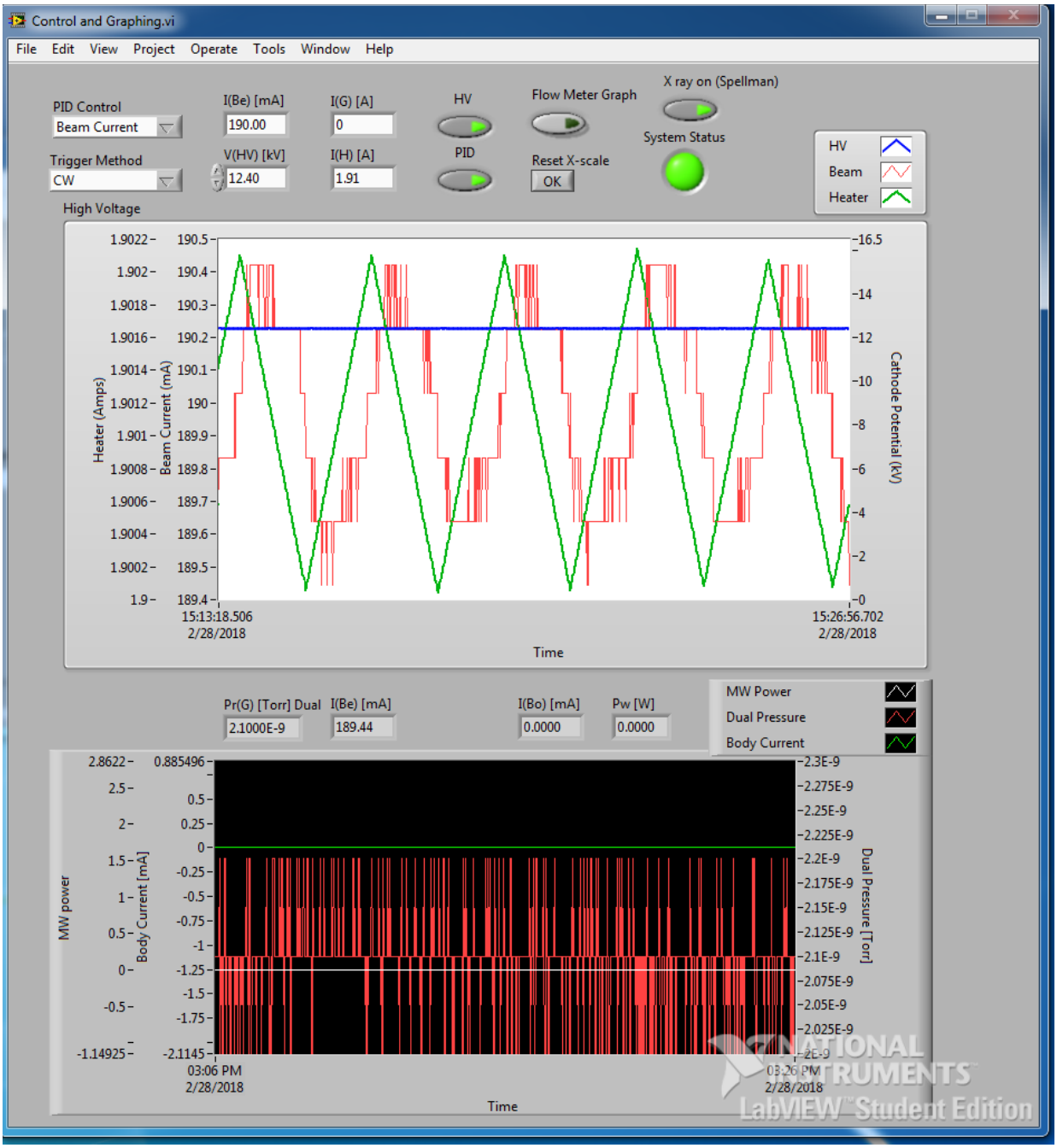

Figure 5.12 "Control and Graphing.vi" during PID. The upper graph tracks voltage (blue), heater current (green) and beam current (red). The heater current value is read into the PID when the PID is active, and the heater value is modulated accordingly.

References

[1] Spellman, Instructional manual-RS232 option- High voltage power supply, (2000) 1–16.

[2] Instruction manual- Terranova model 752A Dual Ion pump control/display, (2007) 1–47.

[3] OTI Series Water to Water Heat Exchanger Operation and Installation Manual, (2011).

Chapter 6: Procedure for bakeout and processing of a frequency agile gyrotron

6.1 Introduction

Ultra-high vacuum (UHV), defined here as 10^{-7} Torr or lower, is important to the operation of gyrotrons. Individual electrons are far less massive than nuclei and can be stopped or diverted before the interaction cavity in the presence of excess molecules. The electron beam cannot propagate through a field of air molecules. The osmium-ruthenium coating on the cathode surface of the electron gun, referred to elsewhere in this manuscript as the magnetron injection gun or MIG, lowers the work function to eject electrons from the surface [1]. If the surface becomes oxidized, the work function increases, and a higher temperature is required to eject electrons at a given potential [2]. This oxidation is known as “poisoning” the cathode. The cathode can still operate with minor oxidation by increasing the heater current driving the heating of the cathode, but if the temperature is too high, the cathode could become inoperable. At slightly high operating pressures (10^{-6} Torr), the cathode emitter surface will become slowly oxidized with available oxygen and water molecules. In the event of a catastrophic pressure event, such as a hot cathode exposed to atmospheric pressure, the cathode can be poisoned beyond recovery.

In order to keep the pressure inside the gyrotron body low, real and virtual leaks are avoided with great care. All joints on the gyrotron are designed as a vacuum tight weld, braze, or CF flange. CF flanges are also known by the brand name Conflat and are sealed by a copper gasket compressed from each side by a stainless-steel knife edge to form a molecule-tight seal. The flange is compressed by six or more bolts depending on the size of the flange.

In addition to vacuum-tight outer seals, precautions are taken against “virtual leaks”, or situations that raise the pressure without the outer seal being breached. Air can become trapped in a tight space, such as between screw threads and a tapped hole, and cannot be removed efficiently by pumping. Virtual leaks can also arise from the presence of surface contaminants such as water and oil, which evaporate into the vacuum space as their boiling point decreases in the low pressure environment [3,4]. Surface contaminants are a problem during processing of the gyrotron because the electron beam will heat certain surfaces and vaporize surface contaminants within the vacuum space, raising the pressure inside the gyrotron. To combat this, the inside surfaces are meticulously cleaned, then assembled and heated under vacuum to remove contaminants.

The process of heating an item under vacuum is referred to colloquially as a “bakeout”. Care is taken after bakeout to avoid reintroducing contaminants, especially water vapor, to the clean inner surface. This chapter records a successful bakeout and processing of a gyrotron built at Washington University in Saint Louis [5].

6.2 Preparing for bakeout

6.2.1 Vacuum test

Parts of the gyrotron outer body were leak checked as they were received from the welding shop or the machine shop. Any part with visible dirt or grease was cleaned before pumping down to avoid contamination of the vacuum pump. A vacuum helium detector was used to pinpoint leaks on an otherwise vacuum-tight weld. All flanges were sealed- usually with CF flanges, but sometimes unfinished parts required the use of rubber plugs and duct seal. Welds that were not under scrutiny were isolated by a sealed bag of nitrogen gas. The leak detector operates by detecting helium gas which is applied externally to the part [6]. Helium gas flowed on the order

of 1 ml/s through a small plastic pipette tip. When not investigating a weld or braze joint, the helium was clamped off to avoid helium diffusion into any leaks.

6.2.2 Cleaning

A special post-machining cleaning procedure is necessary for parts destined for UHV. Machining oils and water vapor are both detrimental to maintaining UHV. Parts of special concern are those with threads, detailed or rough features, or small gaps. Parts later exposed to UHV were cleaned with a series of solvents in the following order: water-based detergent, acetone, and ethanol. Acetone was skipped for pieces that contained a copper surface [7]. Cleaning with detergent removes most machining oils, but often leaves large detergent molecules and water adsorbed to the surface. Acetone is effective at removing the detergent and any leftover oils due to its hydrophobic nature, but can leave a residue of its own. Ethanol molecules are smaller than acetone and are therefore easier to evaporate during bakeout, so ethanol is used to remove acetone residue. 95% ethanol (190 proof) was used as a first wash but 100% ethanol (200 proof) was used for final immersion and rinse to remove all possible H_2O contamination. Some procedures recommend methanol as a final step due to its lighter molecular weight, but a methanol rinse was not necessary to achieve a vacuum of 10^{-10} Torr, the lowest limit available with the vacuum pumps used. Edwards model EXT75DX turbomolecular pump (Burgess Hill, United Kingdom) was used to initially evacuate the gyrotron, and model V20 sputter-ion pumps from Duniway Stockroom Corp. (Fremont, CA) were used later in the bakeout. Since methanol is toxic and does not add any benefit with cleaning, it has been omitted from this protocol.

The parts were gently scrubbed with lint-free wipes and sonicated in the above sequence of solvents when feasible. Sonication is especially beneficial for threads and other rough surfaces

which might tear lint-free wipes. If lint free wipes are torn, they can leave behind fibers in the UHV area which burn during bakeout and leave behind contaminants.

Figure 6.1 Sonicating the internal mode converter taper piece and small screws in ethanol within the sonicator water bath.

Gyrotron parts were submerged in the solvent of choice within a clean glass beaker placed in the water bath of the sonicator. Sonication with flammable and volatile solvents took place within the fume hood. If the water level was higher than solvent level, the beaker capsized, re-contaminating the parts. Sonication proceeded for 30 minutes, then the solvent was changed out for fresh solvent to flush away contaminants. A second 30-minute cycle in the same solvent type was completed before moving on to sonication in the next type of solvent. Clean parts were handled with latex gloves and set down only on fresh sheets of aluminum foil. Each part was

wrapped in aluminum foil and sealed in a plastic zip-top bag to avoid contamination until the full gyrotron was ready to assemble [3]. While the inside of the vacuum chamber was cleaned with special care, the outside was also cleaned to avoid contaminating to the inside of the vacuum chamber via the “clean” latex gloves.

6.2.3 Assembly

When all parts were properly cleaned, the gyrotron was assembled for bakeout. The electron gun was left off in the first bakeout so contaminants from other pieces did not adsorb onto its surface. The vacuum ion pumps were attached, but the magnets and high voltage connections were left off during the beginning of the bakeout and each vacuum ion pump was wrapped in its own independent heating tape.

The table was insulated from the bakeout temperatures of up to 250° C by firebricks and sheets of mineral wool insulation wrapped in aluminum foil. A custom clamp held the gyrotron down to the table (**Figure 6.2**). C-clamps were used to securely clamp the mount to the table before the gyrotron was mounted. After the clamp was mounted, parts were added to the assembly from the center-outward. Interaction cavity and internal mode converter were mounted into the gyrotron once the CF flange between the internal mode converter and the cavity housing was secured (**Figure 6.3**). CF flanges were tightened in a star pattern for six-bolt flanges or another pattern that applied even pressure on the copper gasket [8]. When assembling for bakeout, all bolts used to assemble the gyrotron were new and undamaged, lightly coated with Loctite metal-free lubricant to prevent seizing of the bolts after thermocycle. The new generation of gyrotrons has been designed to minimize the locations where the bolt would need to be machined out in case of bolt failure, but such locations still exist at the electron gun flange and the flange between the collector and the ceramic break and arms section (CBA). Copper flanges for CF flanges are only

meant to be compressed once, and are only rated for one thermocycle or bakeout. Therefore the copper gasket was replaced whenever a flange was removed. When any gyrotron flange was opened, latex gloves were worn to avoid getting body grease inside the gyrotron. Latex gloves were changed often, as they were often contaminated with bolt grease or bodily contact.

6.2.4 Nitrogen backfill

By Le Châtelier's principle, molecules adsorbed onto the surface will enter the gaseous phase when partial pressure of that molecule is decreased, until a new equilibrium is reached [4]. The nitrogen backfill procedure removes low-boiling-point contaminants from the inner gyrotron surfaces by decreasing the partial pressure of said contaminant. A flow of pure nitrogen should theoretically be able to remove all other contaminants, but nitrogen can be adsorbed onto surfaces as well, especially the getter of vacuum ion pumps [9], so bakeout is still required.

Once the tube was mostly assembled, a specialized flange shown in **Figure 6.4a** was attached for nitrogen backfill. While filling the gyrotron with nitrogen, exposure to humid room atmosphere was avoided, especially when the gyrotron was opened after being under vacuum. Nitrogen was introduced to the gyrotron interior through an all-metal valve. A nitrogen feedthrough flange attached to a nitrogen tank was flushed with nitrogen, then attached to the valve. The pressure going into the gyrotron did not exceed 1 atm over atmospheric pressure at any point.

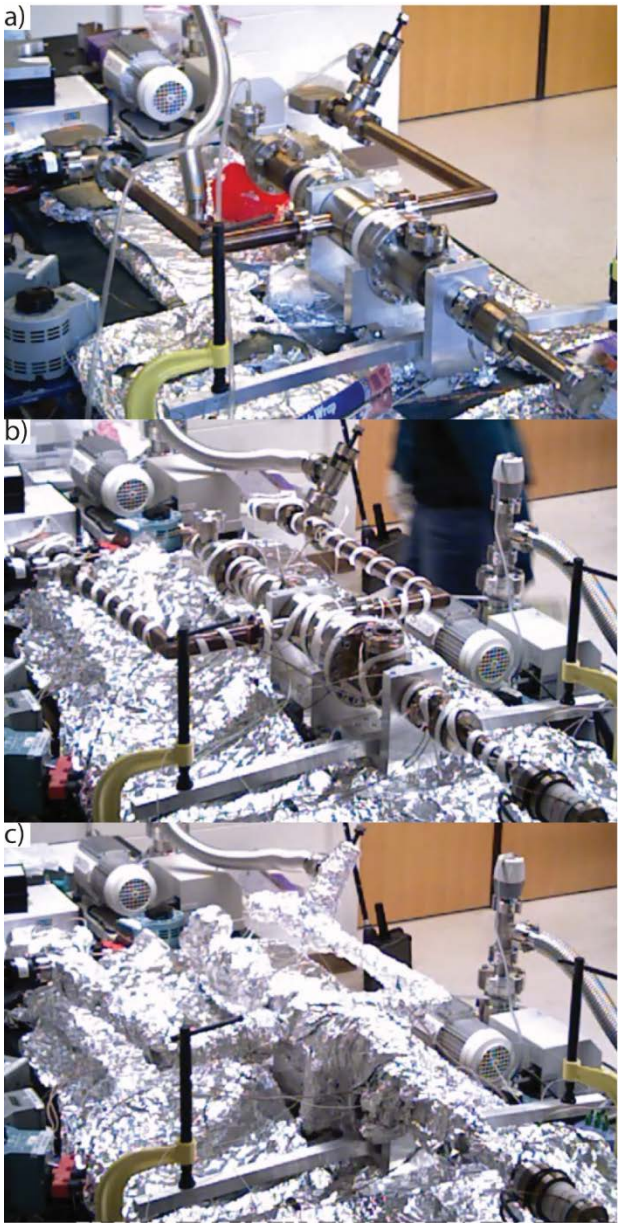

Figure 6.2 a) Gyrotron without electron gun. b) Gyrotron with heating tape and electron gun. c) Gyrotron wrapped in foil for bakeout.

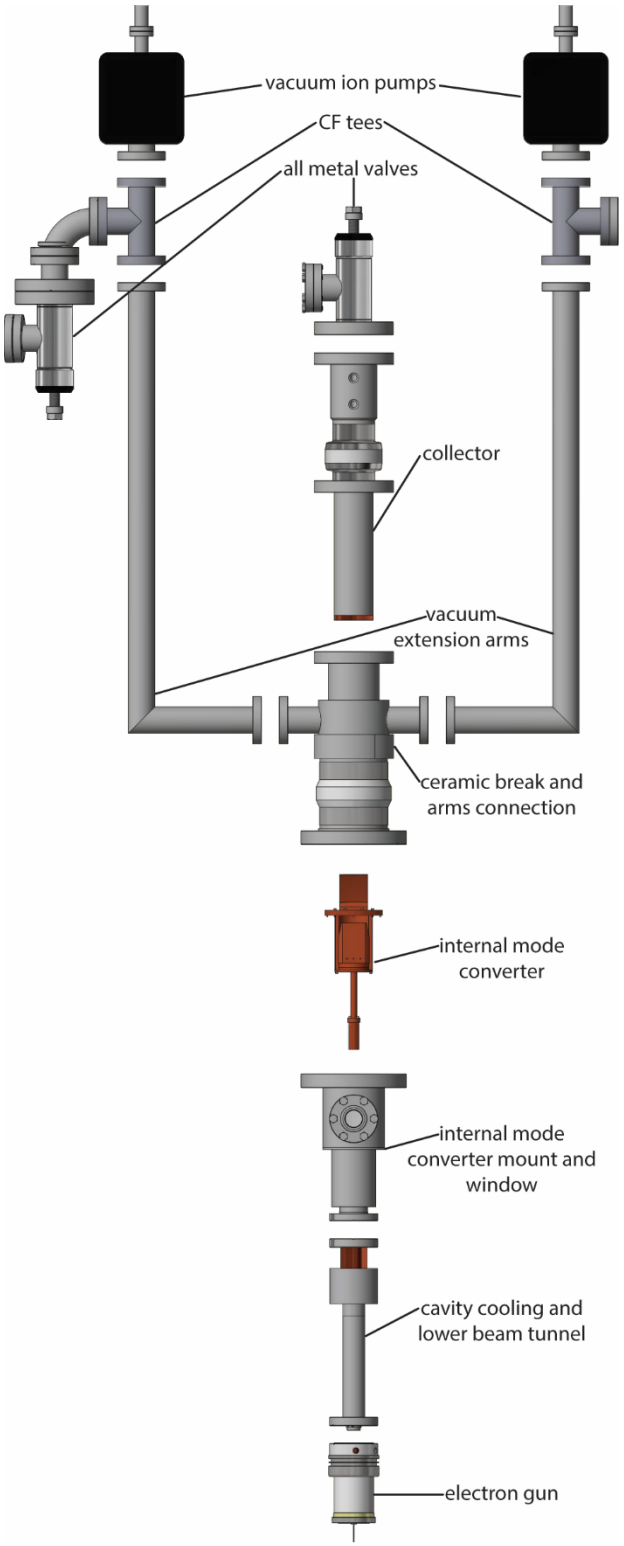

Figure 6.3 Exploded view showing all sections of the gyrotron as separated by CF flanges.

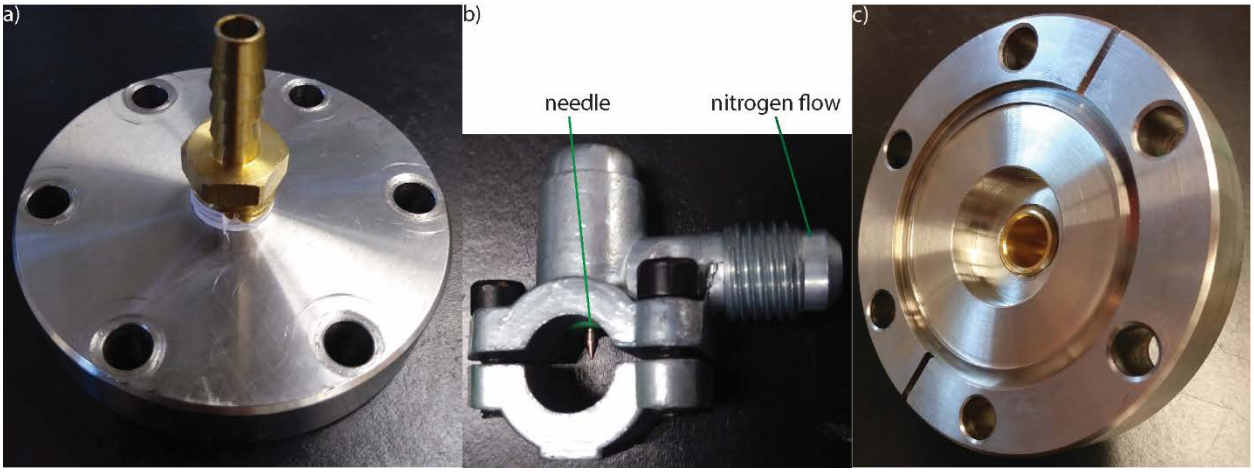

Figure 6.4 Accessories for bakeout: a) nitrogen feedthrough flange, b) piercing attachment for nitrogen backfill of vacuum ion pumps, and c) flange with cutout for lower beam tunnel.

Nitrogen was flushed through the gyrotron by over-pressurization and release. Once the first nitrogen feedthrough flange was attached to the gyrotron, a second feedthrough flange was attached to another location on the gyrotron. The flange's tubing was connected to the same nitrogen tank as the first feedthrough flange, but it was clamped off until just before its attachment to the gyrotron. The second flange was attached more loosely so that the bolts were only finger-tight. When ready to over-pressurize and release, the bolts on the second nitrogen feedthrough flange were loosened slightly so that nitrogen leaked out around the copper gasket. The flange was held down for 10-15 seconds so that pressure built up in the gyrotron, then the flange was released for 0.5 seconds so that nitrogen rushed out around the flange. This cycle of pressure build-and-release was repeated 5-10 times to flush the gyrotron with nitrogen.

A blank flange with a circular cutout 0.750" in diameter and .210" deep was placed at the end of the lower beam tunnel to replace the electron gun (**Figure 6.4c**). The gyrotron assembly was leak checked again once fully assembled to check that all flanges were properly sealed. Once all flanges were confirmed as vacuum tight, the gyrotron was attached to a turbomolecular vacuum pump through an all-metal valve and a short length of flexible metal tubing with CF connections

only. Quik-flange connections were not used as they could not reach the low pressures desired at the end of bakeout.

6.3 Bakeout

In the bakeout procedure, the gyrotron must be heated evenly while a vacuum pulls the previously adsorbed contaminants out of the vacuum chamber. Sometimes other assemblies are baked out in an oven, but heating tape is more feasible for large assemblies. The gyrotron was wrapped in extreme temperature heating tape, which is coated in fiberglass for protection of its electrical wires. Fiberglass fibers are a major skin irritant, so workers wore two layers of latex gloves when handling heating tape. Non-disposable work gloves were not an effective barrier as soon as fibers contaminated the inner surface of the gloves. Heating tape was wrapped evenly around the parts, minimizing overlapping tape which is a risk for overheating. The heating tape was secured to the gyrotron with uncoated copper wire so that it made maximum contact with the gyrotron surface. Pieces that needed more heating, such as the collector, were wrapped with tighter spacing between wraps. The CF flange leading to the turbomolecular vacuum and the aluminum mount were also wrapped in heating tape. Special care was taken to heat the microwave output window so that water did not condense on its inner surface. For the first bakeout, the vacuum ion pumps were wrapped and heated to at least 200° C to expel water and other contaminants adsorbed onto the pumps' getter surfaces. Vacuum ion pumps were wrapped with heating tapes independent from any other gyrotron parts and controlled by a separate Variac variable transformer control unit.

6.3.1 Variac variable transformers and heating tape

Variac variable transformers (referred to as Variac units) control the electric current passed through the heating tapes to generate heat. Up to three heating tape units were controlled with one Variac unit with the use of outlet splitters. Heating tape units were strategically assigned to Variac units with regards to the location of the heating tape and the heat requirements of the location. For instance, two heating tapes wrapped around the same vacuum extension arm were assigned to the same Variac unit. Heating tapes on the collector were assigned to their own Variac unit because the collector was maintained at a higher temperature during bakeout. Variac control unit locations and thermocouple locations were labeled and documented as shown in **Figure 6.5**.

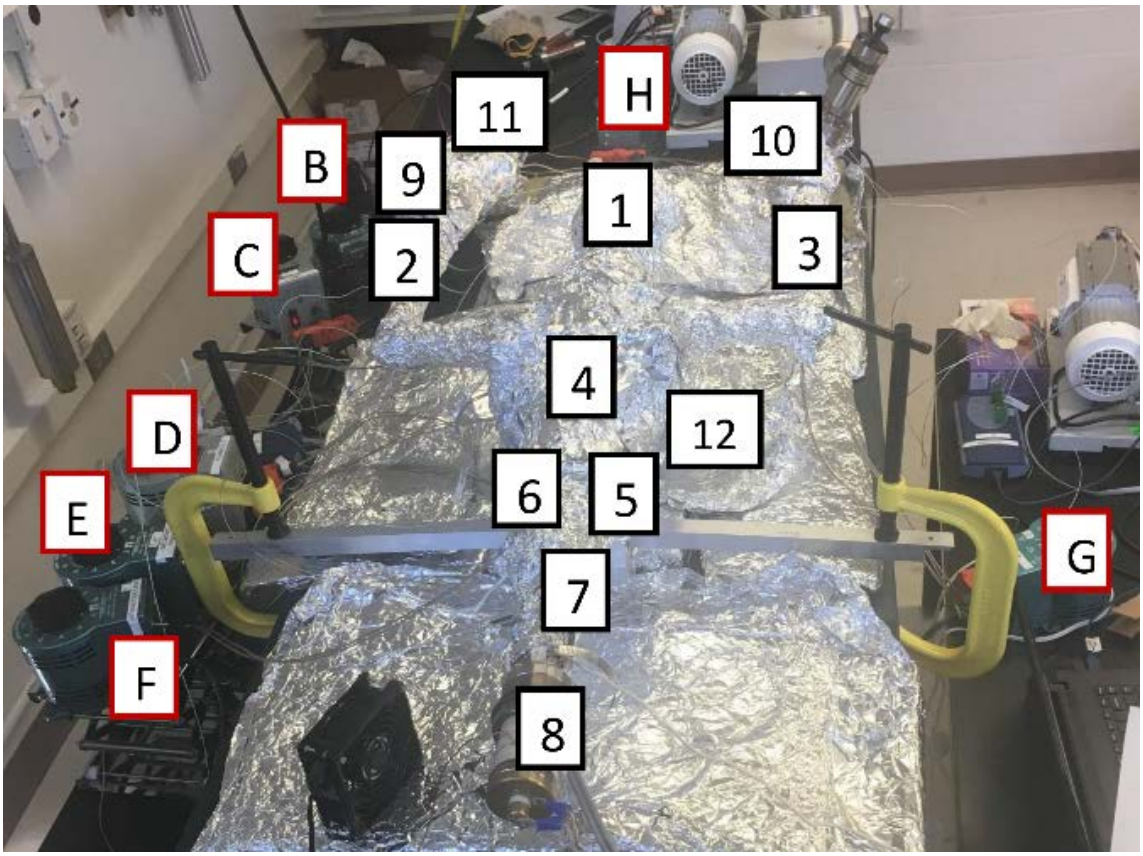

Figure 6.5 Gyrotron schematic as labeled for gyrotron bakeout summer 2017. Variac units are labeled with letters and thermocouples are labeled with numbers**.**

6.3.2 Thermocouples

Throughout the bakeout process, the gyrotron temperature is monitored by up to 20 type J thermocouples read out by USB TC-08 thermocouple data loggers (Pico Technology, St Neots, United Kingdom). The thermocouples were placed securely and strategically to ensure accurate measurement. Special attention was paid to the temperature of the ceramic break, the collector, the vacuum extension arms, the window, and the electron gun. Thermocouple leads were not secured directly under heating tape to prevent charring of the thermocouple casings. The thermocouples were firmly secured with uncoated copper wires so that the head of the thermocouple contacted the gyrotron body. Insecure thermocouples tended to shift with the addition of aluminum foil, resulting in inaccurately low measurements.

After the thermocouples were placed and their placement was documented in the lab record book, the gyrotron was wrapped in aluminum foil to trap convective heat and distribute heat evenly across the gyrotron body. All portions of the gyrotron were encapsulated in aluminum foil. Cords of the heating tape and thermocouples were kept away from the gyrotron surface, and cord exit points were well sealed so that no surface of the gyrotron showed. Three to four layers of foil properly insulated the gyrotron.

6.3.4 Heating the gyrotron

The collector was heated slowly to a maximum temperature of 350° C, and the vacuum ion pumps and the rest of the gyrotron body were heated slowly to 200° C. To avoid runaway temperature increases, the temperature was only increased by 5% of total Variac range over 10 minutes. If the gyrotron was heating unevenly, more aluminum foil was added to trap heat or some Variac units were increased. In some cases, heating tape needed to be rearranged or

replaced. While heaters were increased, the gyrotron was not left unattended for more than 30 minutes. All temperatures were observed to be stable for one hour before the gyrotron was left unattended overnight.

The pressure increased during heating of the gyrotron as contaminants evaporated and were pulled out by the vacuum. Pressure stabilized at maximum bakeout temperature and then started to fall. In different bakeout procedures, stabilization at maximum pressure took between 24 hours and 7 days. Once the pressure stabilized, the bolts were tightened at high temperature, the vacuum ion pumps were "burped," and the gyrotron was gradually cooled.

6.3.5 Tightening bolts at high temperature

Bolts, copper gaskets, and stainless-steel flanges expand at slightly different rates at high temperature. If the bolts are not tightened at high temperature, the flange will be looser at room temperature and may even result in a leak. This leak is usually first observed as an increase in pressure as temperature is decreased. Generally, the pressure should fall as the gyrotron cools. The gyrotron was still extremely hot during tightening at high temperature, so heavy work gloves were used for protection. Foil was peeled back only from the flanges reveal the bolts and Variac units were left at their current settings. The bolts were tightened in a pattern designed to press evenly on the gasket. The aluminum mount was loosened to allow tightening of the flange between the ceramic break and arms connections and the internal mode converter mount.

6.3.6 Activating the vacuum ion pumps

At the end of the bakeout, while the gyrotron was still at high temperature, the vacuum ion pumps were turned on for the first time. This process is known as "burping" because excess gas is expelled from the surfaces of the pump. The vacuum ion pumps were burped while the

gyrotron surfaces were still hot so that the gaseous contaminants did not adsorb onto other locations inside the gyrotron. When the pressure for the first bakeout had stabilized, the heating tape for the vacuum ion pumps were gradually turned off and the foil and heating tape was removed. Once the vacuum ion pump bodies were cool, the magnets were installed around the pumps and the high voltage plugs were attached. All grounding wires were connected to building ground. The vacuum ion pumps were turned on one at a time for a period of less than five seconds at first, and then for longer periods of time as the pressure spikes became less and less extreme [9]. Vacuum ion pumps do not turn on at a pressure of more than 10^{-3} Torr, so the turbomolecular pump was on to pump out the space when the vacuum ion pumps were first turned on. Once the vacuum ion pumps reported a pressure lower than the turbomolecular pump, the valve to the turbomolecular pump was shut to avoid damage to the unit.

6.3.7 Cooling the gyrotron

Once the vacuum ion pumps were burped, the gyrotron was cooled slowly. The Variac units were decreased slowly so that there was no more than 50 degrees Celsius heat differential across the gyrotron. Once all heater units were at 0, the aluminum foil and heating tapes were removed. The pressure should fall as the temperature drops. The pressure rose during cooling when even one gasket was not tight enough. In this case, all the copper gaskets were changed and the gyrotron was baked out again to achieve a tighter flange connection at high temperature. When the gyrotron was back at room temperature, the vacuum ion pumps were turned off and the gyrotron was filled with nitrogen with the feedthrough flange on the CF all-metal valve. Once nitrogen was flowing, another flange was replaced with a feedthrough flange. Now that the inner surface was free of contaminants, nitrogen was made to flow out of the gyrotron whenever a flange was opened so that no part of the gyrotron was exposed to damp air. The getters of the

vacuum ion pumps and the electron gun cathode surface are especially susceptible to contaminants. Every copper gasket was changed in preparation for the next bakeout with the electron gun. New nuts and bolts were used, coated in Loctite anti-size grease as before. The internal mode converter assembly was removed to change the gasket between the cavity and the internal mode converter holder, then re-mounted when the flange was secure. Latex gloves were worn throughout the gasket changing procedure and gloves were changed often.

6.4 Second bakeout with electron gun

6.4.1 Processing the electron gun

If an electron gun has not been used in a few months, activation is required to sustain an electron beam off of the cathode surface (**Figure 6.6a**). The cathode is comprised of a tungsten matrix which supports molten barium. Barium provides the electrons for the electron beam, emitted at the surface where a coating of osmium ruthenium reduces the work function for ejection of electrons. The barium must flow freely to the surface of the cathode. Barium anions can be drawn up to the cathode surface in their molten state with an electric potential. A magnetic field also helps to draw electron-rich barium to the surface. The electron gun is the single most expensive part of the gyrotron, so special care was taken to avoid damage by a fall, overheating, or oxidation of the cathode surface.

To activate the electron gun during the first bakeout, the gun was attached to another turbomolecular pump. The vacuum was kept below 10^{-7} Torr. An AC and DC circuit is required for operation of the electron gun. The AC current heats the electron gun and the DC current provides a potential to draw out electrons. **Figure 6.6 shows t**he circuit diagram for gun activation. The AC current loop was attached to a Variac variable heater and run through a step-

down converter to change the maximum potential. Current was monitored through a multimeter to determine the resistance value- correlated to the temperature of the cathode. The DC potential was supplied by a Tektronix 32 V power supply and current was monitored through a Tektronix multimeter. Note that the AC current was connected through a safety switch that disconnects when no AC voltage is detected so that the electron gun would not be heated without vacuum in case of a power failure. The outer ceramic surface was cooled by a small computer fan. Temperature was monitored by a thermocouple attached to the ceramic surface by a hose clamp on the side opposite the fan, which was warmest. The temperature of the ceramic surface did not exceed 27° Celsius.

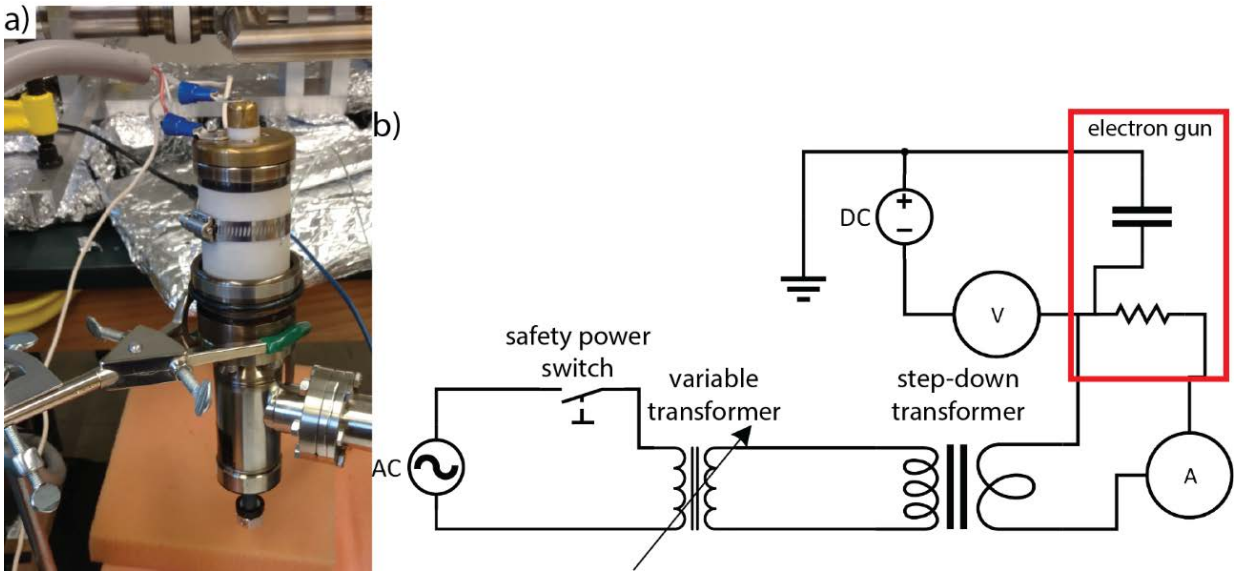

Figure 6.6 a) Electron gun activation in ring stand clamp. b) Circuit diagram of the AC and DC circuits during electron gun activation.

AC potential was increased slowly- the resistance of the cathode circuit will increase as temperature increases, so the temperature can easily increase past a desirable value over time if not monitored. Pressure was monitored during heating as contaminants evaporated from the gun surface. The pressure at the electron gun should never exceed 10^{-7} Torr to avoid surface oxidation at high temperature. The electron gun was heated until the heater current was 2.0 A

and stayed at this stable current as the potential was increased. DC potential was increased very slowly in steps of 1 V until emission was observed on the multimeter as an increase in DC current. At first, the current decreased sharply after the voltage is increased, indicating insufficient electrons had been recruited to the surface. In this case, the potential was dropped back to 0 V and was increased in 1 V steps at a slightly slower pace. Once steady current was observed, the beam emission was compared to the values from the original test of the electron gun shown in **Figure 6.7** (Bridge12 Technologies Inc., Framingham, MA). Calibration tests from Bridge12 Technologies show that the brand-new electron gun reached a higher level of emission at the same voltages and AC current value. Additionally, the power supply used by Bridge12 Technologies reached 50 V instead of 22 V which may have contributed to better activation.

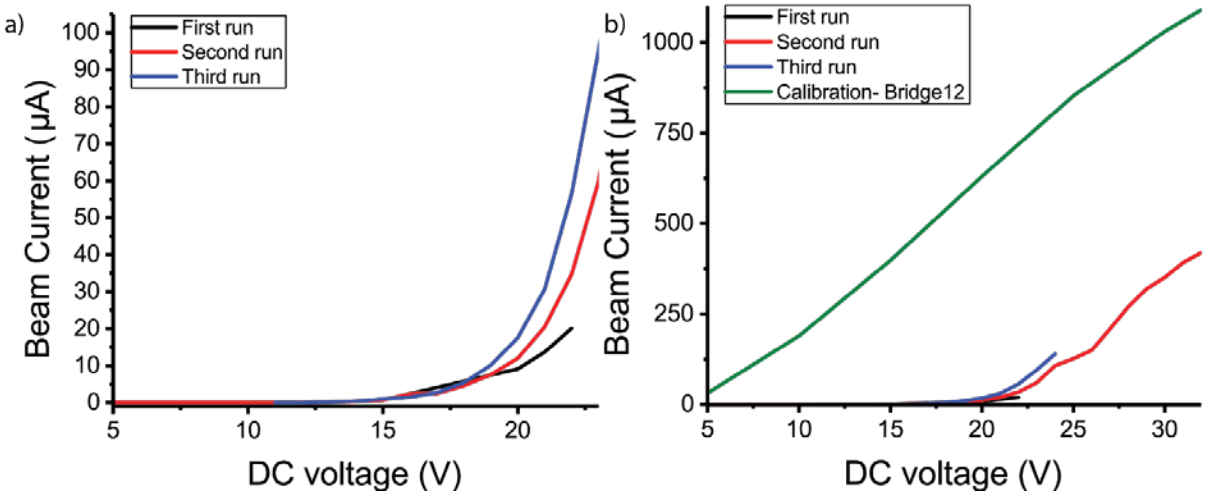

Figure 6.7 a) Current response to voltage increases on subsequent runs. Heater current is at 2.18 A b) Shape and intensity of curve should be compared to the initial tests from Bridge12 Technologies at 2.18 A heater current, used with permission.

When these tests were complete, the electron gun was kept at an AC current of 1.9 A and a DC current of 20 V until the gyrotron body bakeout was finished. Before the gun was removed from vacuum, it was cooled slowly back to room temperature. If the gun was cooled quickly, cracks

could form in the ceramic due to the rapidly falling temperature and thermal shrinkage. The electron gun was set at 0 A for an hour before vacuum was released.

6.4.2 Electron gun installation

When the electron gun was activated and all other gaskets of the gyrotron body were changed, the electron gun was installed on the gyrotron. Copper gaskets, socket head screws greased with Loctite anti-seize grease, and clean wipes and gloves for gun transfer were set aside ahead of time to reduce the amount of time the electron gun was not under vacuum. The electron gun cathode surface should not be exposed to atmosphere at any time during the installation. The electron gun in its current state required socket head screws because of the close clearance to the lower beam tunnel sides. The all-metal valve connected to the electron gun was shut before the turbomolecular pump was turned off and the end occupied by the vacuum pump was attached to a feedthrough flange flushed with pure nitrogen. The gyrotron-side flange was loosened with nitrogen ready to flow through the flange. Several clean copper gaskets were kept at hand. More than one copper gasket fell to the side and was contaminated with grease during installation attempts. The electron gun was then flushed with nitrogen and the flange opened to quickly move the electron gun onto the bottom of the magnet. Once the electron gun was properly attached, the gyrotron was flushed with nitrogen by several rounds of over-pressurization and release. Feedthrough flanges were replaced with their UHV counterparts so that the gyrotron could be immediately pumped out. The turbomolecular pump was attached through the all-metal valve. Once the internal pressure was approximately 10^{-7} Torr, the vacuum ion pumps were turned on and the valve to the turbomolecular pump was closed.

6.4.3 Second bakeout

The second bakeout was completed at lower temperatures than the first bakeout. The electron gun was heated by its internal heater, but no heating tape was added to its outside and a thermocouple confirmed its external temperature as before. Heating the cathode kept contaminants from elsewhere on the gyrotron body from re-adsorbing onto the cool cathode surface. A potential of 20 V kept electrons flowing through the cathode. The pressure in the gyrotron on the second bakeout did not exceed 10^{-7} Torr to protect the electron gun. This required a slower heating of the gyrotron body than the first bakeout. The flanges were tightened at high temperature as before once the pressure stabilized. Then the gyrotron was cooled gradually, with the electron gun cooled last.

6.5 Installation and in-situ processing

6.5.1 Preparing for installation

Once the gyrotron was baked out for a second time, the pressure was low enough for the vacuum ion pumps to turn back on without the assistance of the turbomolecular pump even if they were left off for a short period of time. Once the gyrotron was unwrapped, it was wiped down with paper towels to remove fiberglass detritus, so that it could be handled with bare hands. Before the gyrotron was moved into position in the magnet, all plumbing attachments were connected to the gyrotron as it lay on the table.

The collector and cavity are cooled by water lines attached in the magnet lab to a water heat exchanger. The electron gun was previously water cooled, but the 2nd generation gyrotron arced through the metal attachments to the water lines, therefore the water lines were removed. Current gyrotrons also have external water cooling lines wrapped around the ceramic break to mitigate heating from stray microwaves- see Chapter 2 section 2.5. The heat exchanger water pump has a

very high flow which translates to a high pressure in thin lines. This has caused many water lines to leak, spray, or burst when first connected. This was avoided with a simple test- first the lines were filled with water using a low-pressure pump, then the water circuit was pressurized with about 50 psi of air while connections were searched for leaks and drips. So far, compression fittings have had the lowest failure rate in the gyrotron system when properly installed. Threaded metal pipe fittings with Teflon tape have also had a good success rate. Barbed fittings are not recommended with high water pressure due to repeated failure.

6.5.2 Installation

Gyrotron installation was coordinated so that the vacuum pumps were turned off for the shortest possible amount of time. The gyrotron is held in the magnet by two sets of XY alignment stages and the weight is held by a winch mounted to the ceiling above the magnet. Note- the gyrotron should never be moved when the magnet is at full field. The gyrotron magnet was brought down to 0 T in a few hours. Cross-braces between the two sections of the alignment stage were removed and the clamp plates were loosened and moved out of the way for the old gyrotron to be lifted out by the overhead winch. Clamps on the alignment stages were loosened with caution; the springs have a combined spring constant of over 10 lbs/in. The new gyrotron was adjusted carefully with the winch to the correct z position with respect to the magnet before being clamped in place. The gyrotron cavity should be exactly in the middle of the magnetic field for greatest microwave efficiency. Once the gyrotron was clamped in place, the magnet was energized to a field of 7 T (86.96 A current through the magnet coil). The water lines were attached and tested before the HV connections were put into place. The OptiTemp heat exchanger was turned off before water lines were changed in the magnet lab and additionally

individual water lines were shut off at the back of the heat exchanger unit. The entire heat exchanger tank will empty through one open line given enough time.

The cathode was connected to Spellman high voltage supply by a heavy cable with two ring terminals. Red and white wires on a ring terminal were connected to the larger upper section of the electron gun brass piece (See **Figure 2.3b**). The lower part of the brass was connected to a ring terminal with a single green wire. These connections both carry a high DC voltage, and a smaller amplitude AC voltage difference drives current through the heater filament to increase the electron gun temperature. The anode was connected to ground through a multimeter for all procedures except microwave frequency agility.

The heater current was increased carefully to 1.9 A and the potential was raised in steps of 50 V every five to ten minutes to a voltage of 0.65 kV and a beam current of 0.391 mA. Even with a good bakeout procedure, the pressure increased to $1.2*10^{-8}$ Torr due to the release of contaminants for the heated surface where the electrons impacted in the high magnetic field.

6.5.3 Low power alignment

When the gyrotron was first activated inside the magnet, beam current was maintained under 0.6 mA for alignment at low electron beam power. The anode was connected to ground through a multimeter to detect the current. This current increased when the gyrotron was misaligned and the electron beam hit the beam scraper, referred to as a "rail". This was also usually associated with a pressure spike as a new "dirty" area was bombarded with electrons. In low power alignment, the rails were found by moving the bottom x-stage first, then the bottom y-stage, followed by the top x- and y-stage. At each stage, after finding the two rails, the stage was set in between the value of the two rails. The next stage on the same level was adjusted in the same

way. After many iterations of this process, the cavity was aligned parallel to and concentric with the electron beam which was optimal for microwave power output.

6.5.4 High power alignment

After low power alignment was sufficiently optimized, the DC potential was raised until microwave power was observed. The first microwave power was associated with another rise in pressure and was observed with burn paper, liquid crystal paper, and a calorimeter. When the beam current is above 10 mA, contact with the gyrotron beam scraper may damage or melt the molybdenum beam scraper. To further align the gyrotron at high power, the gyrotron microwave power output was observed through a calorimeter. For alignment at high electron beam power, the x-y stage sets were moved in much smaller increments and left at the settings of maximum microwave power output. After several iterations of high power alignment, the power and frequency were further optimized by adjusting the gun coil, main magnetic field and DC gyrotron potential.

6.5.5 Setup for frequency agility

Once the gyrotron settings were optimized, the gyrotron anode was ungrounded and connected to the second HV circuit attached to the spectrometer AWG through the Trek power supply. This prepared the gyrotron for frequency agility experiments. The gyrotron anode is usually left grounded unless a frequency agility experiment is currently underway.

6.6 Conclusion

A successful bakeout is essential to the operation of the frequency agile gyrotron below 10^{-8} Torr. Moisture and contaminants were expelled from the inner surfaces of the gyrotron to ensure

the efficient performance of the electron gun for high power microwaves. The procedure described herein is expected to result in repeatable success in bakeouts for future gyrotrons.

References

[1] D. Jones, D. McNeely, L.W. Swanson, Surface and emission characterization of the impregnated dispenser cathode, Appl. Surf. Sci. 2 (1979) 232–257. doi:10.1016/0378-5963(79)90036-9.

[2] G. Gaertner, D. Raasch, D. Barratt, S. Jenkins, Accelerated life tests of CRT oxide cathodes, Appl. Surf. Sci. 215 (2003) 72–77. doi:10.1016/S0169-4332(03)00282-4.

[3] M. Taborelli, Cleaning and surface properties, Prep. Vac. Accel. Spec. Course Cern Accel. Sch. (2006) 321–340. doi:10.5170/CERN-2007-003.321.

[4] I.N. Levine, Physical Chemistry, 3rd ed., 1988.

[5] F.J. Scott, E.P. Saliba, B.J. Albert, N. Alaniva, E.L. Sesti, C. Gao, N.C. Golota, E.J. Choi, A.P. Jagtap, J.J. Wittmann, M. Eckardt, W. Harneit, B. Corzilius, S. Th. Sigurdsson, A.B. Barnes, Frequency-agile gyrotron for electron decoupling and pulsed dynamic nuclear polarization, J. Magn. Reson. 289 (2018) 45–54. doi:10.1016/j.jmr.2018.02.010.

[6] SmartTest HLT 550 HLT 560 HLT 570 Operating instructions, (2010) 1–124.

[7] S. V. Kagwade, C.R. Clayton, D. Chidambaram, G.P. Halada, Photochemical breakdown of acetone on copper, Electrochim. Acta. 46 (2001) 2337–2342. doi:10.1016/S0013-4686(01)00359-0.

[8] R. Flitney, Seals and Sealing Handbook, 6th ed., 2014.

[9] Instruction Manual- Sputter-Ion Pump Models V20, V30, V60, V110, V140, V220, V400,

V500, (1998).

Chapter 7: Frequency-agile gyrotron for improved microwave output mode

This chapter is expected to be published as part of a manuscript describing the gyrotron currently used for improved electron decoupling. Another gyrotron is currently under construction (section 7.3.1) and will be characterized before the journal article is completed.

7.1 Introduction

Dynamic nuclear polarization (DNP) is used to enhance sensitivity in nuclear magnetic resonance (NMR) experiments. An electron Rabi frequency sufficient to manipulate electron spins can be achieved by a high power microwave source (5-30 W) or a resonator with a low power source (200 mW) [1–4]. Magic angle spinning (MAS) instrumentation complicates the application of a resonator [5], so a high power microwave source such as a gyrotron is used instead [6]. A frequency-agile gyrotron with a microwave output of 5 W to the sample was used for electron decoupling in DNP [7–9]. A higher electron Rabi frequency allows for faster adiabatic sweeps that could be used to decouple electrons with shorter T_1 due to higher radical concentration or higher sample temperature [10,11].

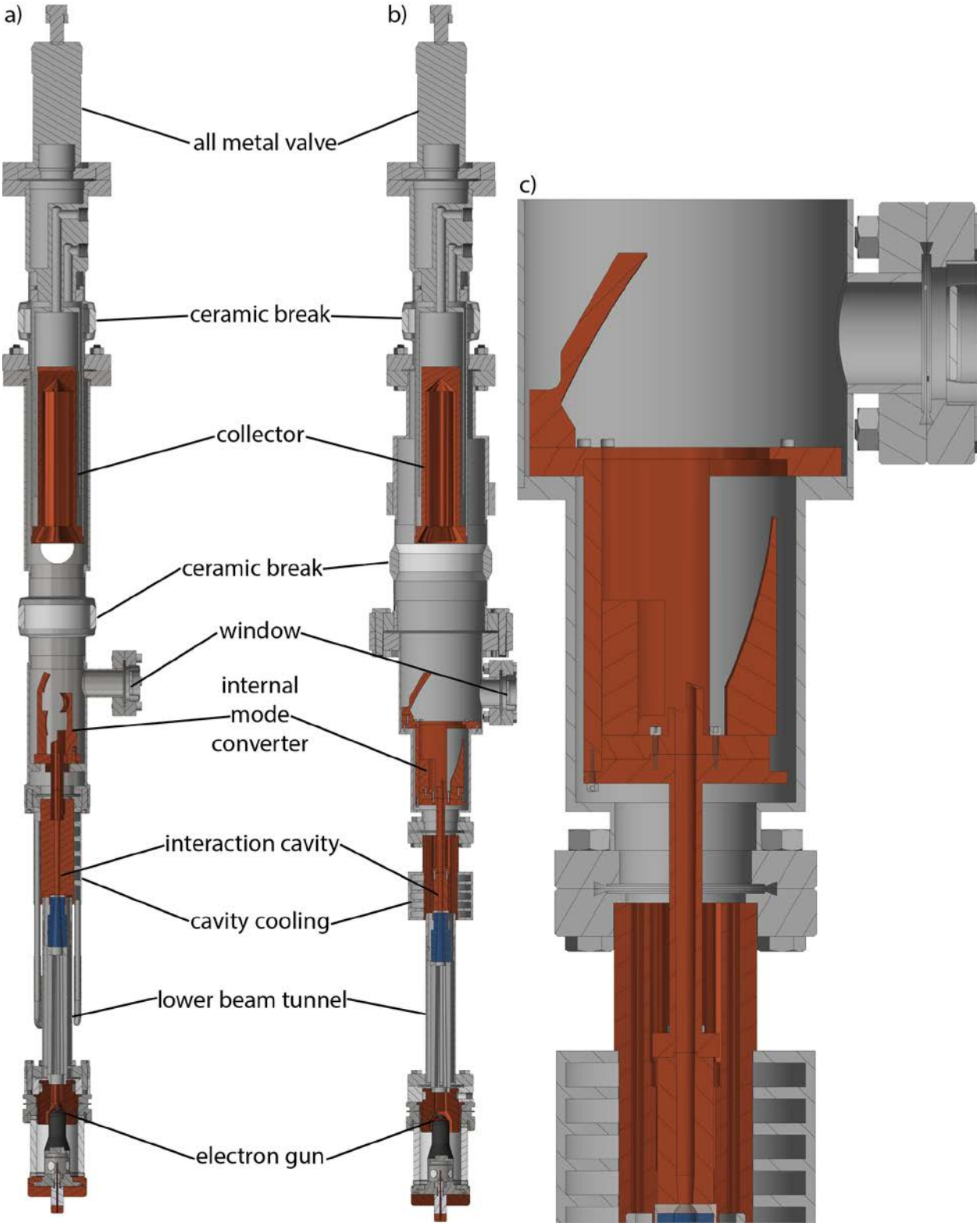

Figure 7.1 Side-by-side comparison of the previous gyrotron (a) and the current gyrotron (b). The collector, electron gun, and all metal valve remained the same between the two models. (c) Detail view of the window, internal mode converter, and cavity for the current gyrotron.

The theoretical power output of the previously published gyrotron at an efficiency of 10% is 500 W [12]. As discussed in [9], much of the microwave power is absorbed at the ceramic break instead of exiting the window into the waveguide. Additionally, the intensity profile emitted from the window does not couple efficiently into the HE_{11} mode. This decreases the efficiency of the microwave propagation in the waveguide. Both symptoms point to the microwaves propagating improperly off the internal mode converter. The mode converter could be misaligned or the mode entering the mode converter could be partially or totally other than the intended TE_{52} mode. We have constructed and processed a gyrotron with a replaceable cavity and internal mode converter to achieve a higher microwave power output and a higher electron Rabi frequency at the sample (**Figure 7.1**). This gyrotron is capable of frequency agility and chirped microwave pulses at a higher microwave power level for improved electron decoupling.

7.2 Improvements in gyrotron design

7.2.1 Interaction cavity

The current gyrotron features a replaceable interaction cavity. In the previous gyrotron design, the interaction cavity was permanently inserted into the cooling jacket with a press fit of copper against copper. The cooling jacket requires a long time to fabricate due to the complex nature of the water tunnels and the weld and braze joints required. By replacing only the cavity, time and cost for gyrotron optimization is reduced. Cavities at new frequency ranges can open up experiments with new electron radicals without changing the main NMR magnetic field. Instead of a press fit to the cooling jacket, the current cavity is attached by screws and alignment pins to the internal mode converter (**Figure 7.2**). The entire internal mode converter and cavity assembly can be lifted out through the top of the 316 stainless-steel internal mode converter mount when the 6” CF flange is opened.

The cavity inner surface was optimized in two ways: the cavity was positioned 23.7 cm from the electron gun so that no gun coil magnetic field is necessary for microwave emission, and the straight section of the cavity is shorter (2.5 cm) to reach a larger band of frequencies without moving the gyrotron magnetic field.

7.2.2 Internal mode converter

The mirrors of the internal mode converter are equally replaceable to permit optimizations, such as dimpled mirror surface to increase the Gaussian content of the output mode [13], or even a completely new design to convert a different mode of microwave from the cavity.

The internal mode converter was redesigned with three mirrors instead of four. Each mirror attenuates the microwave power [14] as it shapes the microwaves into a smaller, more Gaussian shape. By placing the mirrors farther away from each other, the number of mirrors could be decreased. However, this new design has a larger footprint and required expansion of the gyrotron body to match. Mirror surfaces were optimized by Bridge12 Technologies, Inc by calculations in an integral electromagnetics simulation program (**Figure 7.2c**). The mirrors and support structures were then designed in Autodesk Inventor to properly align the mirror surfaces with respect to each other, the microwave beam, and the gyrotron window (San Rafael, CA). 1/16” stainless steel dowel pins were added as a new feature to help keep the mirrors aligned to a tolerance of 0.002” after assembly. The mirror assembly was built on site after the mirrors were machined and polished by Ramco. The interaction cavity was machined by Midwest Precision Tool and Die, Inc. (Sioux Falls, SD).

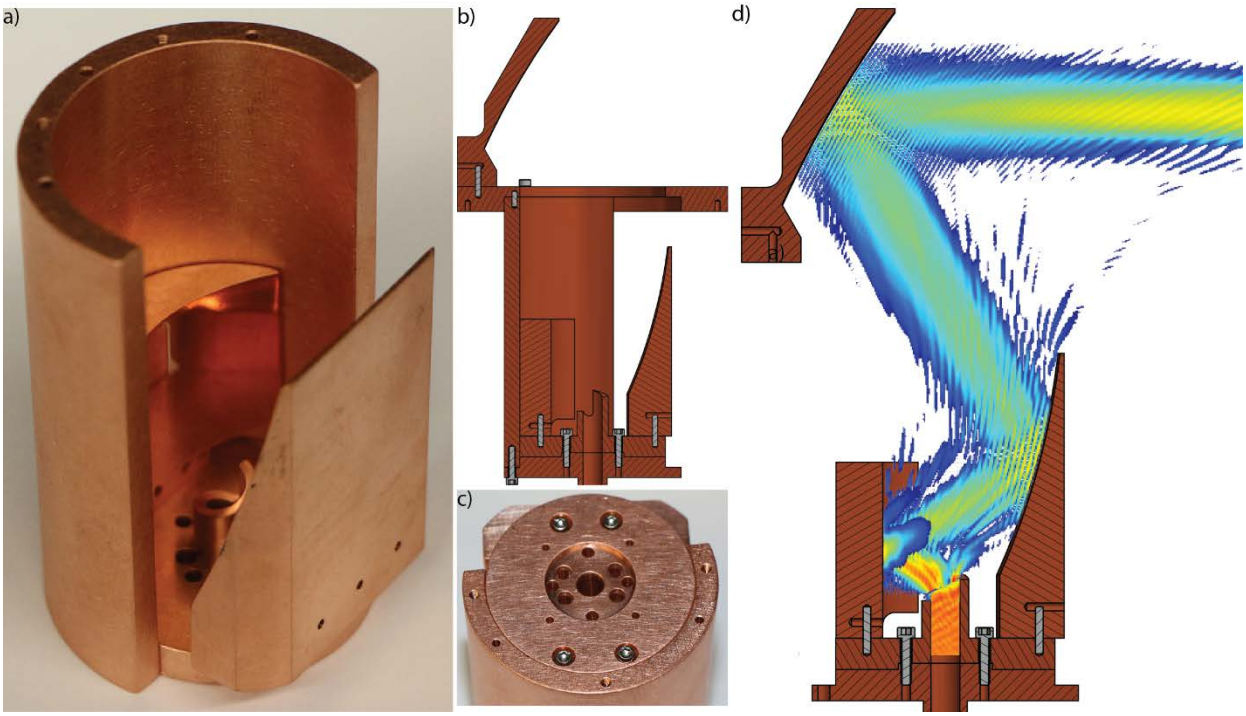

Figure 7.2 a) Photo of the lower two mirrors and Vlasov launcher. b) CAD section view of internal mode converter mirrors and Vlasov launcher. c) Photo of holes for alignment pins. d) Microwave intensity plots overlaid on CAD section view. Microwave intensity plots were calculated by Bridge12 Technologies, Inc. (Framingham, MA).

7.2.3 Alignment stage

The alignment stage for the old gyrotron was constructed of pieces from Thorlabs, Inc. and custom-made clamps. Sliding stages on the side opposite the micrometers posed two main problems. First, a great deal of force had to be used to turn the handle of the micrometer due to the friction and weight on the stages. Second, if the stage was over-extended, the stage would fall out of the dovetail track, often bending the plate which held the dovetail track in place. The problem was fixed temporarily by machining thicker custom plates from brass and restricting the motion of the gyrotron to a smaller range, but the problem persisted when the gyrotron clamps were disconnected.

To solve this, new rails and wheels were purchased and assembled to replace the sliding stages. 80/20 rails were used for the vertical sections, which allowed the horizontal stages on either side to be adjusted to an appropriate height for the new gyrotron (**Figure 7.3**) (80/20 Inc., Columbia

City, IN). The new stages roll on wheels with less friction, and have no chance of falling off the rails. Stages can be adjusted vertically to accommodate new clamp locations on the gyrotron body.

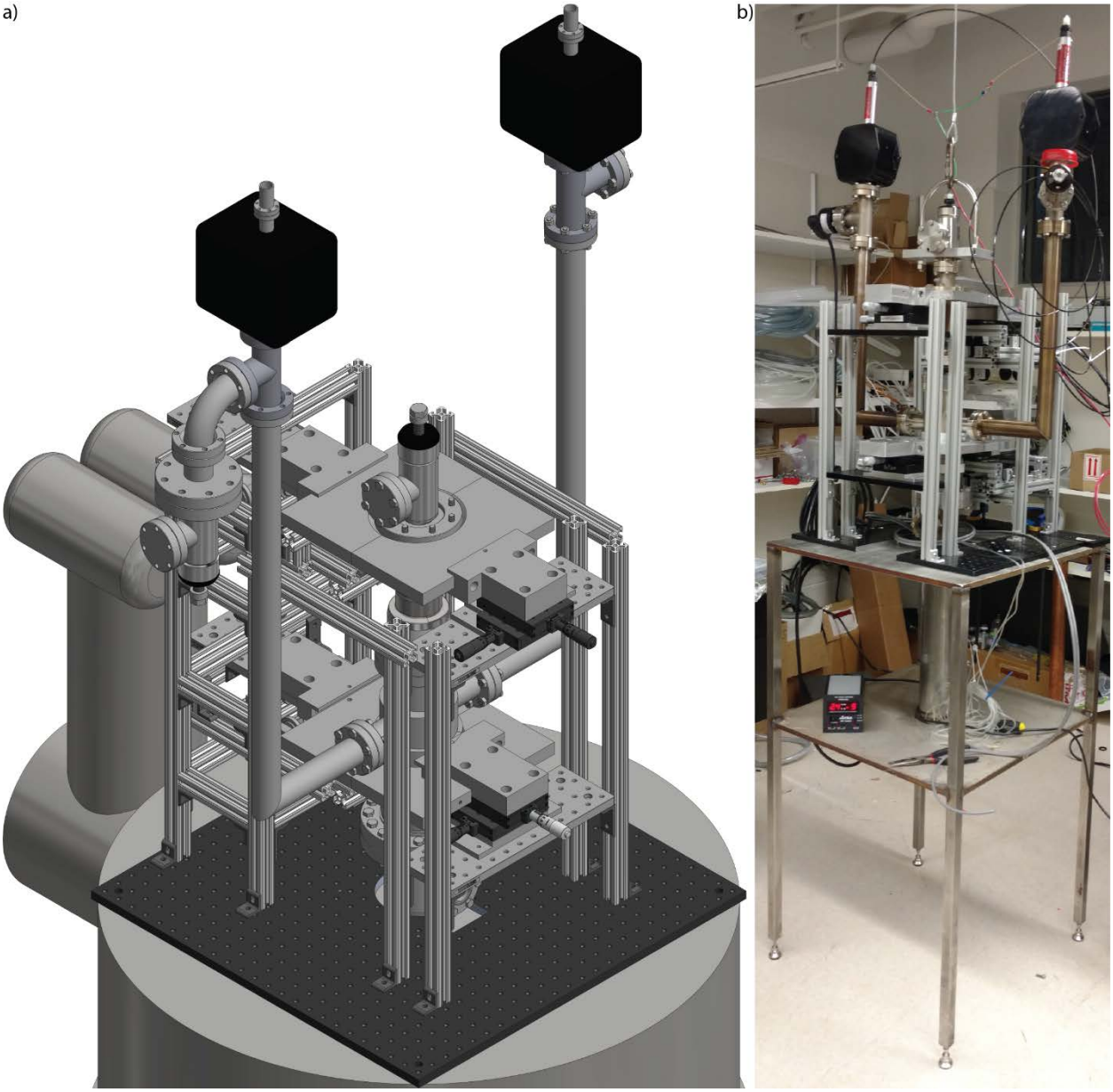

Figure 7.3 a) Gyrotron mounted in new alignment stage. View is reversed to show the support side of the alignment stage rather than the micrometer side. b) Gyrotron in new alignment stage, mounted on magnet facsimile table while testing the alignment stage. The hole size in the table was representative of the bore size of the magnet.

Springs were required to counter the weight of the gyrotron and allow the stages to operate. The new alignment stage shows signs of hysteresis during beam alignment but exhibits less friction

than the previous alignment stage. Springs must be carefully aligned so that the wheels do not twist in the tracks, causing the alignment stage to stick in place. The bar across the two towers keeps the towers from leaning in towards each other due to spring tension.

7.3 Results

7.3.1 Increased efficiency in waveguide transmission

According to measurements and experimental results, the power at the sample with the previous gyrotron was about 5 W. This resulted in an electron Rabi frequency of 0.49 MHz [10]. The current gyrotron produces 40 W instead of 36 W, but 13 W propagates to the end of the waveguide, meaning that the electron Rabi frequency is 1.27 MHz without any focusing lens or resonator. This is because the mode of the current gyrotron is more Gaussian-like (TE_{01}) and propagates more efficiently in the waveguide in an HE_{11} mode. The improved mode that increases the power propagation can be attributed to a better design or alignment of the internal mode converter.

7.3.2 Gyrotron tuning bandwidth

The output range for the currently implemented gyrotron is 750 MHz at a single magnetic field (**Figure 7.4**) compared to an output range of 670 MHz for the previous gyrotron. This increase in bandwidth can be attributed to the shorter 2.5 cm cavity replacing a 3.0 cm interaction cavity. Output power was measured with a diode calorimeter monitored by a Tektronix (DMM4050) multimeter.

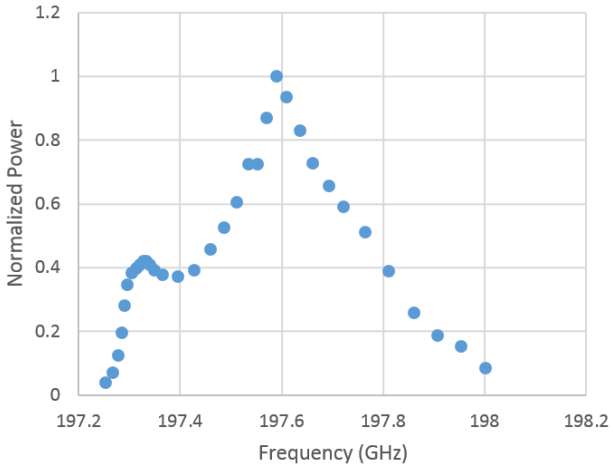

Figure 7.4 Gyrotron output power measured over tuning bandwidth with a diode calorimeter.

7.3.3 Heating of the ceramic break

The previous gyrotron and current gyrotron both heat the ceramic break during microwave emission. This is a symptom of microwave power generated within the interaction cavity and not properly reflected by the internal mode converter, but rather reflected internally until it is absorbed as heat by the ceramic break. This could be due to a problem in the internal mode converter or with the cavity. The internal mode converter was carefully simulated (**Figure 7.2**) during the redesign to confirm maximum power from the TE_{52} mode is directed out of the gyrotron. The cavity may also be generating modes other than TE_{52} which are not converted properly by the internal mode converter.

In the previous design, a second straight section near the center of the magnetic field could have acted as a parasitic cavity that caused modes other than the TE_{52q} mode at 197 GHz to be excited. The new cavity was machined with no extraneous straight sections, however the internal surface was machined with a severe chatter on the interior of the cavity. Other modes may still be formed by the cavity surface which was not machined to specification. The bakeout and processing of a new cavity in another gyrotron body is now underway and is expected to give a higher microwave output in the TE_{52q} mode, resulting in a higher power efficiency of the

gyrotron, which will be reflected in less heating of the ceramic break. The theoretical output power of the gyrotron with the new cavity is 300 W based on a 10% efficiency and a beam current of 3 kW.

7.4 Conclusion and future directions

The current implementation of the gyrotron has proved the feasibility of the replaceable interaction cavity. This will allow optimization of gyrotrons for different frequency bandwidths. The three-mirror internal mode converter is better aligned due to the dowel pins implemented in the current design. An identical gyrotron body with a new smooth-wall cavity is predicted to produce up to 300 W of microwaves for a 7.5 times higher electron Rabi frequency at the sample. This should improve implementation of electron decoupling and pulsed DNP experiments in rotating solids.

References

[1] L.R. Becerra, G.J. Gerfen, R.J. Temkin, D. Singel, R.G. Griffin, Dynamic nuclear polarization with a cyclotron resonance maser at 5 T, Phys. Rev. Lett. 71 (1993) 3561–3564. doi:10.1103/PhysRevLett.71.3561.

[2] T. Dubroca, A.N. Smith, K.J. Pike, S. Froud, R. Wylde, B. Trociewitz, et al., A quasi-optical and corrugated waveguide microwave transmission system for simultaneous dynamic nuclear polarization NMR on two separate 14.1 T spectrometers, J. Magn. Reson. 289 (2018) 35–44. doi:10.1016/j.jmr.2018.01.015.

[3] T.A. Siaw, A. Leavesley, A. Lund, I. Kaminker, S.-I. Han, A versatile and modular quasi optics-based 200 GHz dual dynamic nuclear polarization and electron paramagnetic resonance instrument, J. Magn. Reson. 264 (2016) 131–153.

doi:10.1016/j.jmr.2015.12.012.

[4] V. Weis, M. Bennati, M. Rosay, J.A. Bryant, R.G. Griffin, High-field DNP and ENDOR with a novel multiple-frequency resonance structure, J. Magn. Reson. 140 (1999) 293–299. doi:10.1006/jmre.1999.1841.

[5] F.J. Scott, E.L. Sesti, E.J. Choi, A.J. Laut, J.R. Sirigiri, A.B. Barnes, Magic Angle Spinning NMR with Metallized Rotors as Cylindrical Microwave Resonators, (n.d.). doi:10.1002/mrc.4744.

[6] A.B. Barnes, E.A. Nanni, S.K. Jawla, Q.Z. Ni, J. Herzfeld, R.G. Griffin, et al., A novel high power 3 GHz tunable 250 GHz gyrotron for Dynamic Nuclear Polarization, in: 2012 IEEE 13th Int. Vac. Electron. Conf. IVEC 2012, 2012: pp. 329–330. doi:10.1109/IVEC.2012.6262183.

[7] E.P. Saliba, E.L. Sesti, F.J. Scott, B.J. Albert, E.J. Choi, N. Alaniva, et al., Electron Decoupling with Dynamic Nuclear Polarization in Rotating Solids, J. Am. Chem. Soc. 139 (2017) 6310–6313. doi:10.1021/jacs.7b02714.

[8] E.L. Sesti, E.P. Saliba, N. Alaniva, A.B. Barnes, Electron Decoupling with Cross Polarization and Dynamic Nuclear Polarization Below 6 K, J. Magn. Reson. (n.d.).

[9] F.J. Scott, E.P. Saliba, B.J. Albert, N. Alaniva, E.L. Sesti, C. Gao, et al., Frequency-agile gyrotron for electron decoupling and pulsed dynamic nuclear polarization, J. Magn. Reson. 289 (2018) 45–54. doi:10.1016/j.jmr.2018.02.010.

[10] D.E.M. Hoff, B.J. Albert, E.P. Saliba, F.J. Scott, E.J. Choi, M. Mardini, et al., Frequency swept microwaves for hyperfine decoupling and time domain dynamic nuclear

polarization, Solid State Nucl. Magn. Reson. 72 (2015) 79–89. doi:10.1016/j.ssnmr.2015.10.001.

[11] Ē. Kupce, R. Freeman, Adiabatic pulses for wideband inversion and broadband decoupling, J. Magn. Reson. Ser. A. 115 (1995) 273–276.

[12] G.S. Nusinovich, Gyrotron Oscillators for Controlled Fusion Experiments, in: Introd. to Phys. Gyrotrons, The John Hopkins University Press, 2004: pp. 215–238.

[13] Y. Hirata, Y. Mitsunaka, K. Hayashi, Y. Itoh, K. Sakamoto, T. Imai, The design of a tapered dimple-type mode converter/launcher for high-power gyrotrons, IEEE Trans. Plasma Sci. 31 (2003) 142–145. doi:10.1109/TPS.2003.808864.

[14] E.A. Nanni, S.K. Jawla, M.A. Shapiro, P.P. Woskov, R.J. Temkin, Low-loss transmission lines for high-power terahertz radiation, J. Infrared, Millimeter, Terahertz Waves. 33 (2012) 695–714. doi:10.1007/s10762-012-9870-5.

Chapter 8: Conclusion

8.1 Gyrotrons for increased electron Rabi frequency

This dissertation contains many examples of instrumentation intended to give better control over electron spins for electron decoupling. The first frequency-agile gyrotron used for electron decoupling was designed and built at Washington University in Saint Louis. While the gyrotron produced sufficient power for an electron Rabi frequency of 0.49 MHz at the DNP-NMR sample, optimizations could improve the microwave output power of this device.

After building, baking out, and processing a new frequency-agile gyrotron, microwave output power was improved by 11%. However, power at the sample increased by 160% due to the improved coupling efficiency of the microwave mode into the waveguide. The exchangeable interaction cavity allows for further improvement of microwave power as the interaction cavity surface is optimized. The replaceable cavity lowers the production cost for gyrotrons in the future as only the interaction cavity and internal mode converter need to be replaced to change gyrotron characteristics [1,2]. A triode electron gun could also be used in place of the current electron gun to access microwave frequency agility without maintaining the gyrotron body at high voltage. The triode electron gun would connect a neutral section to the gyrotron body, separated by a ceramic break from the anode [3].

8.2 Cryostat and probes at low sample temperature

The cryostat and cryogenic system enable better electron spin control as electron relaxation times are increased at low temperatures. The cryostat described herein allows for further innovation in NMR probes. Magic angle spinning spheres, which have the potential to spin stably at higher spinning frequencies than their cylindrical rotor counterparts, are currently being investigated

[4]. Stators for spheres are easily implemented into probes fitted to the current cryostat to decrease the need to new cryogenic equipment.

8.3 Resonant structure for sample Q > 1

The rotor-mounted resonator described in Chapter 4 can be altered to take advantage of new rotor geometries such as MAS spheres. The cylindrical rotor outer surface was readily coated with vacuum deposited copper. The cylindrical inner surface of a spherical rotor will not be as simple to coat, but a different strategy could be feasible. Relatively inexpensive quartz tubes externally coated with copper could be inserted into the sphere. The tubes could be packed with DNP sample to determine the presence of a resonance structure, which increases the Q of the sample area to more than 1. Different quartz tube outer diameters could be used to optimize the resonance structure for 197-198 GHz. A resonant structure with a Q of 100 would increase the electron Rabi frequency at the sample by 10,000 times, resulting in improved electron decoupling through electron spin control.

References

[1] A.B. Barnes, E.A. Nanni, S.K. Jawla, Q.Z. Ni, J. Herzfeld, R.G. Griffin, et al., A novel high power 3 GHz tunable 250 GHz gyrotron for Dynamic Nuclear Polarization, in: 2012 IEEE 13th Int. Vac. Electron. Conf. IVEC 2012, 2012: pp. 329–330. doi:10.1109/IVEC.2012.6262183.

[2] D.R. Whaley, M.Q. Tran, T.M. Tran, J. Antonsen, T.M., Gyrotrons Using High-Order Operating Modes, IEEE Trans. Plasma Sci. 22 (1994) 850–860.

[3] K. Kajiwara, Y. Oda, A. Kasugai, K. Takahashi, K. Sakamoto, Development of dual-frequency gyrotron with triode magnetron injection gun, Appl. Phys. Express. 4 (2011)

11–14. doi:10.1143/APEX.4.126001.

[4] P. Chen, B.J. Albert, C. Gao, N. Alaniva, L.E. Price, F.J. Scott, et al., Magic Angle Spinning Spheres, Sci. Adv. Accepted (2018) 1–13.